

Colloids near phase transition lines under shear

Colloïden in de buurt van faseïijnen onder shear
(met een samenvatting in het Nederlands)

Proefschrift

Ter verkrijging van de graad van doctor aan de Universiteit Utrecht op het gezag van de Rector Magnificus, Prof. dr. H. Voorma, ingevolge het besluit van het College voor Promoties in het openbaar te verdedigen op vrijdag 23 februari 2001 des namiddags te 14.30 uur.

door

Tjerk Albert Jelle Lenstra
Geboren op 20 mei 1973 te Utrecht



Universiteit Utrecht

Promotoren:

Prof. dr. H.N.W.Lekkerkerker

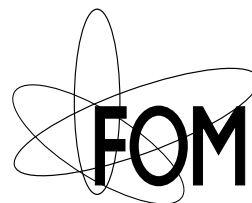
Verbonden aan:

Van't Hoff laboratorium voor Fysiche- en Colloïdchemie, Debye Instituut,
Universiteit van Utrecht

Prof. dr. J.K.G. Dhont

Verbonden aan:

Weiche Materie, Institut für Festkörperforschung, Forschungszentrum Jülich,
Deutschland



The work described in this thesis is part of the research program of the Stichting voor Fundamenteel Onderzoek der Materie (FOM) and was made possible by financial support from the Nederlandse Organisatie voor Wetenschappelijk Onderzoek (NWO).

ISBN 90-393-2621-5

Cover by / Omslag door Remco Lenstra

Photo on the back of the cover is the experimental birefringence/dichroism set up.
Foto op achterkant van de omslag is de experimentele dubbelbrekings/dichroïsme opstelling.

CONTENTS / INHOUDSOPGAVE

Chapter 1: <i>COLLOIDS IN SHEAR FLOW</i>	3
Chapter 2: <i>FLOW DICHROISM IN CRITICAL COLLOIDAL FLUIDS</i>	17
Chapter 3: <i>SHEAR-INDUCED DISPLACEMENT OF ISOTROPIC-NEMATIC SPINODALS</i>	45
Chapter 4: <i>SHEAR-BANDED STRUCTURE IN SUSPENSIONS OF RIGID RODS</i>	75
<i>SUMMARY</i>	87
<i>DE ESSENTIE NA 4 JAAR</i> (SAMENVATTING VOOR NIET-VAKBROEDERS EN ZUSTERS)	91
<i>NAWOORD</i>	101
<i>LIST OF PUBLICATIONS</i>	104
<i>CURRICULUM VITAE</i>	105

Chapter 1

COLLOIDS IN SHEAR FLOW

1.1 INTRODUCTION

Colloidal particles, which have linear dimensions of roughly 1 nm to 10 μm , behave in much the same way as atoms and molecules do. In experimental investigation, the advantage of colloidal system is that the length and time scales of interest are much larger. Dynamics and structure of colloids are therefore much more easily experimentally accessible as compared to atomic/molecular systems. The two major differences between colloidal and atomic/molecular systems are that the dynamics of colloids are affected by so-called hydrodynamic interactions, and that the form of the pair-interaction potential for colloids can be varied between long ranged repulsive to short ranged attractive. These kind of interaction potentials which do not exist for atomic/molecular systems give rise to dynamics and phase behaviour that are specific for colloids. The hard-core part of the pair-interaction potential between the colloidal particles can be varied by the shape of the particle, namely by chemically synthesising spheres, platelet-like and rod-like colloidal particles. The additional interaction characteristics can be tuned by surface modification and variation of the solvent.

Due to the fact that the linear dimensions of the colloids are so large, the dynamics will be relatively slow; foreexample, rod-like and plate-like colloids are so large that the rotational diffusion will be slow compared to atoms/molecules. Due to these relatively slow dynamics, colloidal systems show interesting behaviour in rheological experiments, for example, shear-thinning (and some times shear-thickening) behaviour on increasing the shear rate. The time scale on which microstructure diffusely evolves is now so large, that for experimentally accessible shear rates the microstructure cannot respond instantaneously to the applied shear field. For the anisotropic shaped particle, rods and platelets, this will result in the fact that small shear rates are sufficient to align the colloidal particles. In case of atomic/molecular systems, away from a critical point, the microstructural dynamics are so fast, that unrealistically high shear rates would be necessary to see the same kind of shear-thinning behaviour.

The experimental work described in this thesis involves time resolved birefringence and dichroism measurements under shear. In the subsequent chapter, the effect of shear flow on critical microstructure structure of a mixture of spherical colloids and polymer, close to it's gas-liquid critical point, is described. The polymers induce an

effective attraction between the colloidal particles, which can be sufficiently strong to induce a gas-liquid phase transition. Near the gas-liquid critical point, the microstructural dynamics are slow as compared to systems away from a critical point (a phenomenon that is referred to as “critical slowing down”) and the spatial extent of microstructure is large in comparison to the size of the colloidal particles. The effect of shear flow near the critical point is therefore enhanced as compared to, for example, colloids with a hard-core interaction potential. Due to the long ranged nature of effective interactions between the colloidal particles close to the critical point, scaling relations for, for example, shear induced dichroism can be derived. These relations are universal in the sense that they are independent of the details of the pair-interaction potential, that is, they are independent of the particular system under investigation. The corresponding scaling functions can be found within the mean field region from the solution of the Smoluchowski equation under shear flow conditions. In fact, dichroism measurements are used to test theoretical predictions on the microstructure under shear flow. There is no theory yet for the region very close to the critical point, beyond mean field. A completely different behaviour of the shear induced dichroism in the mean field as compared to the beyond mean field region is found.

In Chapter 3 a system of rod-like colloids is investigated, where the effect of shear flow can essentially be attributed to the shear-alignment, and the effect of shear flow on correlations can be neglected. This is the complete opposite of effect of shear flow on critical microstructure of spherical colloids, where the shear induced distortion of correlations is the sole reason for all shear induced phenomena. The shear dependence of isotropic-nematic spinodals of suspensions of fd-virus particles is measured by means of time resolved birefringence measurements. In the final Chapter 4 we examine a flow instability that was observed in suspensions of stiff, rod like boehmite particles. In a couette geometry, banded structures along the vorticity directions are found. The internal microstructural order within the bands is probed by means of birefringence effects. It turns out that the stationary banded state can not be identified with a shear-banded state, nor with a state that is normally observed in incompressible, Newtonian fluids which exhibit the Taylor instability. It could be that the instability is nevertheless a Taylor instability, but that the final, stationary banded state differs from that of simple fluids, possibly because of shear-thinning effects and a possible spatially varying density of the rods.

This introduction discusses, in an intuitive way, what dichroism and birefringence is and how these are induced by applying a shear flow to colloidal fluids. In addition, the home built experimental set ups and optical couette cell are discussed.

1.2 DICHOISM AND BIREFRINGENCE IN SHEARED COLLOIDS.

When light passes through a material the intensity of the transmitted light I will be smaller than the intensity I_0 of the incident light beam. The relation between these two intensities is described by Lambert-Beer's law,

$$\frac{I}{I_0} = \exp(-\tau l) \quad (1.1)$$

Here, τ is the turbidity and l the path length that the light traversed through the sample. The loss of intensity is due to absorption and/or scattering of the light. For the colloidal systems under investigation in this thesis there is no absorption. A finite value of the turbidity is solely due to scattering of light by the colloidal particles. In most materials the turbidity τ is independent of the polarisation state of the light. For some materials, however, light is attenuated differently with different polarizations states, that is, *the turbidity is polarization state dependent*. Such a material is termed dichroic, and the phenomenon is referred to as *dichroism*. A daily example of dichroism that results from absorption rather than scattering are Polaroid sun glasses. The intensity of the light is attenuated by absorption of aligned polymers. Light polarised parallel to the polymer alignment direction is absorbed most strongly. This is illustrated in Figure 1.1. For colloids under shear flow, the total amount of scattered light depends on the polarisation direction due to the anisotropic nature of the microstructure under shear flow.

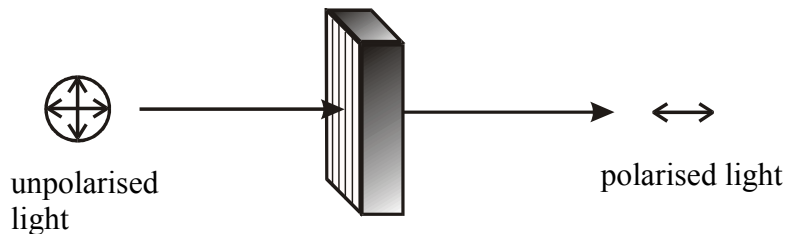


Figure 1.1: Representation of a Polaroid sheet. Light with a polarisation direction parallel to the aligned polymers is absorbed more strongly as compared to light with a polarisation direction perpendicular to the polymers. The circle and ellipsoid on the left and right hand-side of the figure, respectively, are projections of the electric field component onto the plane of the paper.

A material is called birefringence, when the refractive index is polarisation state dependent. The velocity of light is now depending on the polarisation state of the light, and hence the optical path length will be different for differently polarized light. This results in a phase difference between light with different polarisation states after having passed the birefringence material. This generally changes linearly polarised light into to elliptically polarized light, as is illustrated in Figure 1.2. To understand this in some more detail, the polarisation direction of the light can be decomposed

into a component parallel to the direction where the refractive index is large and a component parallel to the direction where the refractive index is small. After having traversed the sample, there is a relative phase shift of the two field components. The resulting electric field component, which is the sum of the two fields, is now generally elliptically polarised, that is, the polarisation direction of the electric field rotates with the frequency of the original electric field and the field component strength depends on the polarisation direction.

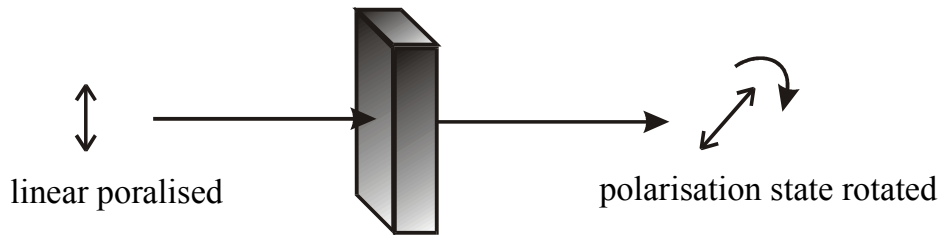


Figure 1.2: Linear polarised light is generally transmitted as elliptically polarised light through a birefringent material. The ellipse on the right hand-side is a projection of the electric field component onto the plane of the paper.

Birefringence can occur in colloidal suspensions of rod like particles which are optically anisotropic in the sense that their refractive index depends on the polarisation direction of the light relative to their own orientation. When the rods have a preferred orientation, for example due to an externally applied shear flow, the suspension behaves as a birefringent material. In fact, since the microstructure is anisotropic, the suspension will also exhibit dichroism.

1.3 DICHROISM AND BIREFRINGENCE MEASUREMENTS

1.3.1 DESCRIPTION OF THE EXPERIMENTAL SET UP'S

The set up that is used in the present thesis to measure shear induced dichroism and birefringence is home built, and based on a design proposed by Fuller [1]. A schematic representation of the optical train is given in Figure 1.3. In the last subsection the optical train will be discussed in some more detail.

The light of a He-Ne-laser first passes through the beam splitter BS'. This beam splitter is used in order to monitor the incident light beam intensity with detector D3. The beam of light then passes the polarizer P1. After this first optical element, the beam is directed through a pinhole and subsequently through the half wave retardation platelet R1. This retardation plate is mounted on a rotor (dentist drill with a hollow axle), which enables to rotate the platelet with an angular velocity ω_d of about 4 kHz.

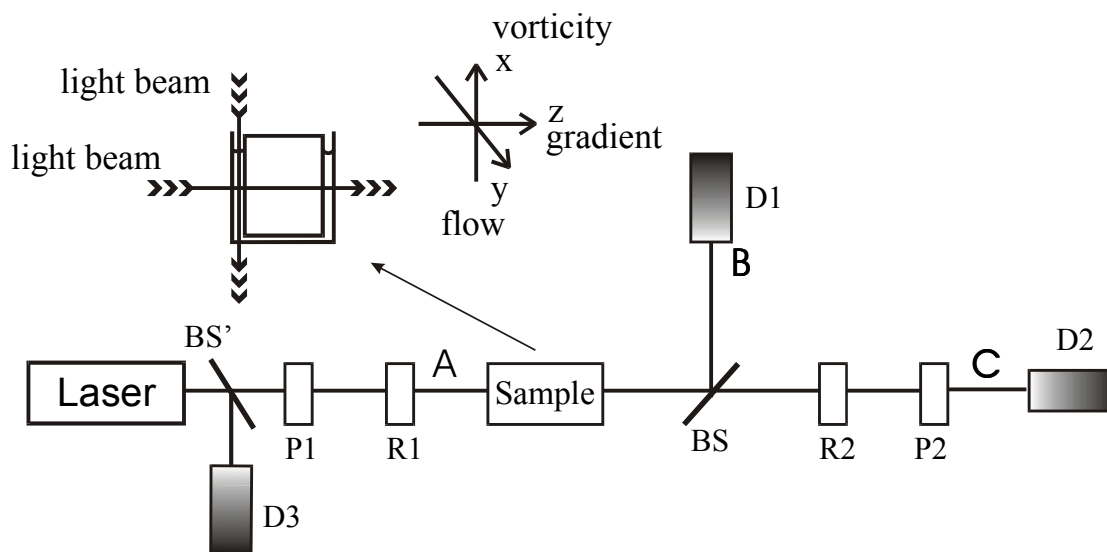


Figure 1.3: Schematic of the experimental set-up for dichroism and birefringence measurements.

The light then passes the shear cell, which will be described in some more detail below (see Figure 1.5). The transmitted beam is then directed towards two detectors (D1 and D2) by means of the non-polarizing beam splitter BS. Half of the transmitted intensity is directed towards detector D1, the other half of the intensity impinges onto detector D2 after having passed the quarter wave platelet R2 and the polarizer P2. The polarisation direction of P2 is the same as for P1, while the axis of R2 are at 45° . Both signals of the detectors D1 and D2 are then analysed by two dual phase Lockin-Amplifiers. These amplifiers filter out the 4ω component of the detected signals. As will be shown below, combination of these components from both detectors allow for the determination of both dichroism and birefringence simultaneously.

When one is only interested in dichroism, a somewhat simpler set up can be used, which is sketched in Figure 1.4. This is essentially the above described set up where the detector D2 has been removed. This set up can also be used to measure the turbidity for a given polarisation state of the light, using Lambert-Beer's law in eq.(1.1). To this end, the ratios of the intensities of detectors D1 and D3 are measured with the sample and just solvent, respectively, in the absence of the rotor R1.

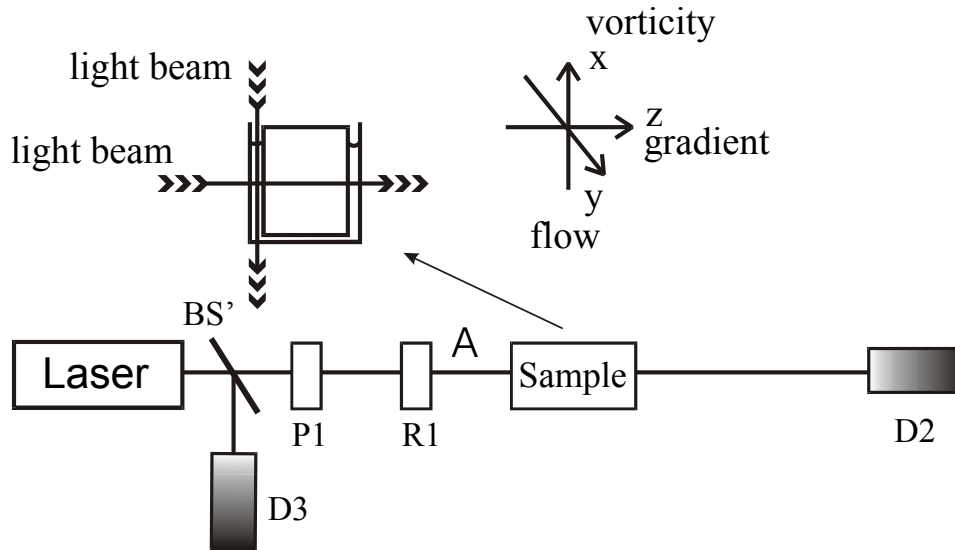


Figure 1.4: Schematic of the set up that can be used for a dichroism measurement.

1.3.2 THE SHEAR CELL

The shear cell is a home built, optical couette cell. A sketch of this cell is presented in Figure 1.5. The optical part of the cell is constructed from BK7 optical glass. The cell is constructed in such a way that one has the possibility to perform experiments where the laser beam propagates either along the gradient direction or the vorticity direction. Although in this thesis, experiments are described only for the case where the laser beam propagates along the gradient direction, a special feature is included. To avoid refraction at the meniscus in case the laser beam is directed along the vorticity direction, a glass ring is installed at the top of the optical part of the cell. The inner cylinder is rotated by means of a belt around the belt-support S. Within the hollow inner cylinder, which is filled with toluene, a pinhole P can be used when this cell is used for light scattering experiments: scattered light from the first gap is now blocked, and only light that is scattered from the second gap is detected. In case of dichroism and birefringence measurements this pinhole is absent. The lower, optical part of the shear cell is placed in a thermostating and optically matching toluene bath.

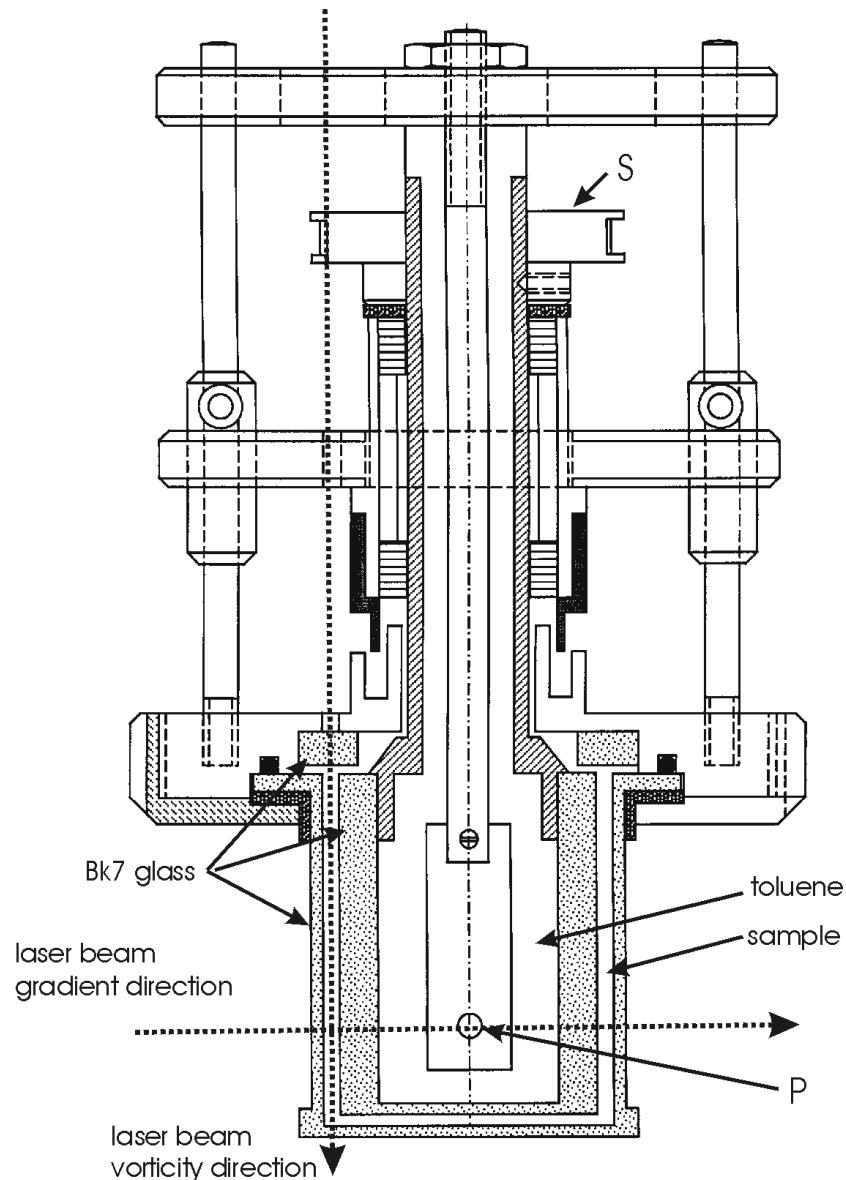


Figure 1.5: A sketch of the home built shear cell.

1.3.3 ANALYSIS OF THE OPTICAL TRAINS IN FIGURE 1.3 AND FIGURE 1.4

Choosing the propagation direction of the incident light beam in the z-direction, the polarization state of the light can be described by a two-vector,

$$\mathbf{E} = \begin{pmatrix} E_x \\ E_y \end{pmatrix}$$

where E_x and E_y are the x- and y-components of the electric field strength. The xy-coordinate system sketched in Figure 1.3 and Figure 1.4. The action of a linear optical element can now be represented by a two-dimensional matrix. Such matrices are usually referred to as Jones-matrices. A few Jones matrices are collected in the

table below, together with their short-hand notation. It is convenient to introduce complex number as entries in these matrices to specify the phase of both electric field components [see for more details, [2]]. For example, $iE_x = \exp(i\pi/2)E_x$ is phase shifted over an angle $\pi/2$ (that is, a quarter wavelength) relative to E_x .

Physical meaning	Matrix	Short notation
Polariser aligned in the x-direction	$\begin{pmatrix} 1 & 0 \\ 0 & 0 \end{pmatrix}$	$\mathbf{P}(x)$
Retardation elements: $\lambda/2$ plate and $\lambda/4$ plate	$\begin{pmatrix} -1 & 0 \\ 0 & 1 \end{pmatrix}$ and $\begin{pmatrix} i & 0 \\ 0 & 1 \end{pmatrix}$	$\Lambda(\frac{1}{2})$ and $\Lambda(\frac{1}{4})$
Non-polarising 1-1 beam splitter	$\begin{pmatrix} \frac{1}{\sqrt{2}} & 0 \\ 0 & \frac{1}{\sqrt{2}} \end{pmatrix}$	\mathbf{B}
Rotation over an angle σ	$\begin{pmatrix} \cos \sigma & \sin \sigma \\ -\sin \sigma & \cos \sigma \end{pmatrix}$	$\mathbf{R}(\sigma)$

Table 1.1: Table with Jones matrices and there short hand notations

These Jones matrices will be used in the following discussion to calculate the electric field strength at the detectors in the experimental set-ups. This interpretation will make it possible to analyse the detected intensities at the photodiodes in terms of the apparent dichroism and birefringence of the sheared sample.

The first beamsplitter (BS') and detector D3 is of no significance for the polarisation state of the light. First consider the electric field strength at point A (see Figure 1.3 and Figure 1.4). The light, from the He/Ne-laser passes a polariser and a rotation halfwave platelet (R1). In Jones matrix notation, the formal expression for the electric field strength \mathbf{E}_A at point A is equal to,

$$\mathbf{E}_A = \mathbf{R}(-\omega t) \Lambda(\frac{1}{2}) \mathbf{R}(\omega t) \mathbf{P}(x) \mathbf{E}_0 \quad (1.2)$$

where \mathbf{E}_0 is the incident field strength. The first matrix $\mathbf{P}(x)$ from the right is the Jones matrix for the first polariser (P1), which principle axis is along the x-direction. The rotation matrix $\mathbf{R}(\omega t)$ rotates the coordinate system over the angle ωt between the original coordinate system and the principle axes of the retardation platelet. Within this coordinate system the action of the retardation platelet is given by the matrix $\Lambda(\frac{1}{2})$ in Table 1.1. The matrix $\mathbf{R}(-\omega t)$ then transforms back to the original coordinate system.

Evaluation of equation (1.2) results in,

$$\mathbf{E}_A = E_{x_0} \begin{pmatrix} \cos(2\omega_d t) \\ \sin(2\omega_d t) \end{pmatrix} \quad (1.3)$$

The electric field point \mathbf{A} is thus linear polarized light of which to polarization direction rotates with an angular velocity of 2ω .

The field \mathbf{E}_A now passes the birefringent and dichroic sample. Birefringence gives rise a relative phase shift φ between E_x and E_y , while dichroism introduces a polarisation dependent attenuation of the electric field strength. We will assume here that birefringence and dichroism in a sheared colloidal fluid are *coaxial*, that is, their principle axes are identically oriented. The Jones matrix with respect to a coordinate system of which the axes coincide with the principles optical axes that describes the combined birefringence and dichroism of the sheared sample reads,

$$\mathbf{M} = \begin{pmatrix} \exp(-\frac{1}{2}\tau_x) \exp(i\varphi_x) & 0 \\ 0 & \exp(-\frac{1}{2}\tau_y) \exp(i\varphi_y) \end{pmatrix} \quad (1.4)$$

where τ_x and τ_y are the turbidities corresponding to the two principle axes. Before this Jones matrix acts on the electric field strength, we have to transform the field first to a coordinate system with it's base vectors along the principle axes of the sample. This amounts to a rotation over the angle α between the original coordinate system and the direction of the principle axes. Transforming back to the original coordinate system thus leads to the following expression for the Jones matrix for the sample,

$$\mathbf{R}(-\alpha) \mathbf{M} \mathbf{R}(\alpha) \quad (1.5)$$

After the sample has been probed, the transmitted light beam is split in two: half of the intensity is lead to the photodiode cell D1, the other half to detector D2. The field at detector D1 is the field at point B in Figure 1.3, which is equal to,

$$\mathbf{E}_B = \mathbf{B} \mathbf{R}(-\alpha) \mathbf{M} \mathbf{R}(\alpha) \mathbf{E}_A \quad (1.6)$$

The first matrix on the left hand side represents the beamsplitter (BS). Evaluating equation (1.6) results in,

$$\mathbf{E}_B = \frac{E_{x_0}}{\sqrt{2}} \begin{pmatrix} e^{-\frac{1}{2}\tau_x} e^{i\varphi_x} [\cos \alpha \cos(2\omega t - \alpha)] - e^{-\frac{1}{2}\tau_y} e^{i\varphi_y} [\sin \alpha \sin(2\omega t - \alpha)] \\ e^{-\frac{1}{2}\tau_x} e^{i\varphi_x} [\sin \alpha \cos(2\omega t - \alpha)] + e^{-\frac{1}{2}\tau_y} e^{i\varphi_y} [\cos \alpha \sin(2\omega t - \alpha)] \end{pmatrix} \quad (1.7)$$

The beam intensity at detector D2 is thus equal to,

$$i_B = \frac{I_0}{2} (e^{-\tau_x} \cos^2(2\omega t - \alpha) + e^{-\tau_y} \sin^2(2\omega t - \alpha)) \quad (1.8)$$

which can also be written as,

$$i_B = \frac{I_0}{2} e^{-\frac{1}{2}(\tau_x + \tau_y)} \cosh \delta'' (1 - \tanh \delta'' \cos 2\alpha \cos 4\omega t - \tanh \delta'' \sin 2\alpha \sin 4\omega t) \quad (1.9)$$

where we defined,

$$\delta'' = \frac{1}{2}(\tau_x - \tau_y)$$

Note that the factor $\frac{1}{2}$ is due to the (non-polarizing) beamsplitter BS in the set up sketched in Figure 1.3. Since this beamsplitter is absent in the set up sketched in Figure 1.4, the light intensity measured by the detector D1 in this latter set up is given by eq.(1.9), without the prefactor $\frac{1}{2}$. When one is interested in dichroism only, the set up in Figure 1.4 suffices. When one is interested in birefringence, however, the intensity at detector D2 in the set up sketched in Figure 1.3 must be measured in addition.

Since the principle axis of the quarter lambda platelet R2 make an angle of $\pi/4$ with the original coordinate system, while the polariser P2 is oriented along the x-axis, we find that the field strength at point C is equal to,

$$\mathbf{E}_C = \mathbf{P}(x) \mathbf{R}\left(-\frac{\pi}{4}\right) \mathbf{\Lambda}\left(\frac{1}{4}\right) \mathbf{R}\left(\frac{\pi}{4}\right) \mathbf{E}_B \quad (1.11)$$

Evaluation of equation (1.11) leads to,

$$\mathbf{E}_C = \frac{E_{x_0}}{2\sqrt{2}} \begin{pmatrix} e^{-\frac{1}{2}i\tau_x d} e^{i\varphi_x} \cos(2\omega t - \alpha) (\cos \alpha (i+1) + \sin \alpha (i-1)) \\ + e^{-\frac{1}{2}i\tau_y d} e^{i\varphi_y} \sin(2\omega t - \alpha) (\cos \alpha (i-1) - \sin \alpha (i+1)) \\ 0 \end{pmatrix} \quad (1.12)$$

The intensity at point C, which is the intensity detected by D2, is thus equal to,

$$i_C = \frac{I_0}{4} (e^{-\tau_x} \cos^2(2\omega t - \alpha) + e^{-\tau_y} \sin^2(2\omega t - \alpha)) \\ + \frac{I_0}{8} i \left(-e^{-\frac{1}{2}(\tau_x + \tau_y)} e^{i\Delta\varphi} \sin(4\omega t - 2\alpha) + e^{-\frac{1}{2}(\tau_x + \tau_y)} e^{-i\Delta\varphi} \sin(4\omega t - 2\alpha) \right) \quad (1.13)$$

or,

$$i_C = \frac{I_0}{4} e^{\frac{1}{2}(\tau_x + \tau_y)} \cosh \delta'' \left[1 - \left(\tanh \delta'' \cos 2\alpha + \frac{\sin \Delta\varphi}{\cosh \delta''} \sin 2\alpha \right) \cos 4\omega t \right. \\ \left. - \left(\tanh \delta'' \sin 2\alpha - \frac{\sin \Delta\varphi}{\cosh \delta''} \cos 2\alpha \right) \sin 4\omega t \right] \quad (1.14)$$

Where,

$$\Delta\varphi = \varphi_x - \varphi_y$$

is the difference in phase shift of the x- and y-component of the electric field strength, φ_x and φ_y , respectively.

Equations (1.9) and (1.14) show that combination of the 4ω frequency components of the time dependent detector signals (and the dc-response of both detectors) renders the required information concerning birefringence and dichroism, including the orientation of the principle axes of the sample. These frequency components can be filtered from the detector signals by means of lock-in amplifiers.

1.4 RELAXATION OF THE FLOW PATTERN AFTER CESSATION OF SHEAR FLOW

In some of our experiments, the dynamics of relaxation of dichroism and birefringence is measured, after cessation of the applied shear flow. It is therefore important to know how fast the fluid flow itself relaxes. This relaxation time defines the time window below which no measurements on the dynamics of microstructural order can be done.

In order to estimate the relaxation time of the flow pattern, we need to solve the Navier-Stokes equation. Consider a linear flow pattern between two flat plates, as sketched in Figure 1.6. For a laminar flow in the x-direction, with its gradient direction in the y-direction, the Navier-Stokes equation reads,

$$\rho \frac{\partial u(y,t)}{\partial t} = \eta \frac{\partial^2 u(y,t)}{\partial y^2} \quad (1.15)$$

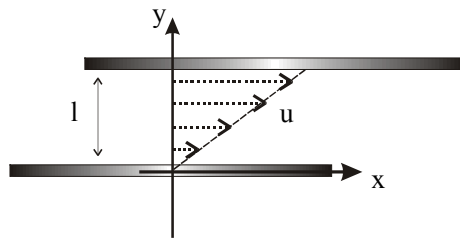


Figure 1.6: Flow pattern between two flat plates

where u is the fluid flow velocity, ρ is the suspension mass density and η is the suspension shear viscosity. The initial flow velocity varies linearly with the distance y from the lower plate,

$$u(y, t = 0) = \dot{\gamma} y \quad (1.16)$$

Where $\dot{\gamma}$ is the shear-rate. For stick boundary conditions we have (for $t > 0$),

$$\begin{aligned} u(y = 0, t) &= 0 \\ u(y = l, t) &= \dot{\gamma} l \end{aligned} \quad (1.17)$$

Where l is the gapwidth, that is, the distance between the two plates. The solution of the above problem can be written as a sin-series,

$$u(y,t) = \frac{2\dot{\gamma}l}{\pi} \sum_{n=1}^{\infty} \frac{(-1)^{n+1}}{n} \sin\left\{n\pi \frac{y}{l}\right\} \exp\left\{-\frac{\eta}{\rho} \frac{n^2\pi^2}{l^2} t\right\} \quad (1.18)$$

The y - and t -dependence of the velocity field is plotted in Figure 1.7. As can be seen, the flow pattern virtually dropped to 0 for times of the order,

$$\tau \approx \frac{\rho}{4\eta} \frac{l^2}{\pi^2} \quad (1.19)$$

For typical numbers this time is found to equal to $\tau = 0.1$ s. This is the lower time resolution limit for dynamical experiments.

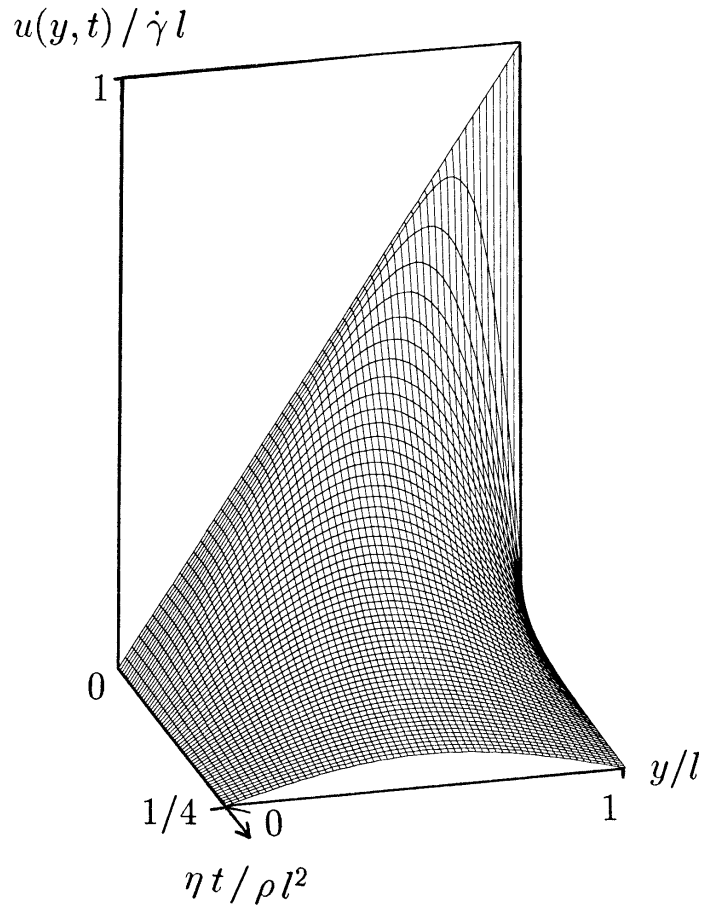


Figure 1.7: y - and t -dependence of the velocity field

1.5 REFERENCES :

1. G.G. Fuller and K.J. Mikkelsen, *Optical rheometry using a rotary polarization modulator*. Journal of Rheology, **33**, 761 (1989).
2. G.G. Fuller, *Optical Rheometry of complex fluids*. first edition, editor K.E. Gubbins. 1995, Cornell University: Oxford University press. 268.

Chapter 2

FLOW DICHROISM IN CRITICAL COLLOIDAL FLUIDS

Due to long range correlations and slow dynamics of concentration fluctuations in the vicinity of the gas-liquid critical point, shear flow is very effective in distorting the microstructure of near-critical fluids. The anisotropic nature of the shear-field renders the microstructure highly anisotropic, leading to dichroism. Experiments on the dichroic behaviour can thus be used to test theoretical predictions on microstructural order under shear flow conditions. We performed both static and dynamic dichroism and turbidity measurements on a colloid/polymer mixture, consisting of silica spheres (radius 51 nm) and PDMS polymer (molar weight 204 kg/mol). Sufficiently far away from the critical point, in the mean-field region, the experimental data are in good agreement with theory. Very close to the critical point, beyond mean field, for which no theory exists yet, an unexpected decrease of dichroism on approach of the critical point is observed. Moreover, we do not observe critical slowing down of shear-induced dichroism, right up to the critical point, in contrast to the turbidity.

2.1 INTRODUCTION

Critical phenomena have been studied for a long time, and the critical behaviour of various quantities is well understood. The main interest has been to understand the difference between the values of critical exponents in the mean-field region and very close to the critical point. Very little is known about the effects of external fields on critical behaviour and the critical behaviour of properties that are induced by external fields. In particular, non-conservative external fields, which cannot be described in terms of a Hamiltonian or a free energy, do not allow for the well-known thermodynamic approaches that led to the current knowledge of critical phenomena. Shear flow is an example of such a non-conservative external field. The critical behaviour of systems in such non-conservative external fields must be studied on the basis of kinetic equations. The most fundamental kinetic equation is the equation of motion for the probability density function of phase-space variables. In principle, equations of motion for macroscopic variables can be derived from this fundamental kinetic equation, which then allows for the prediction of their critical behaviour. Alternatively, the measurement of the critical behaviour of a macroscopic quantity can be used to test a theoretical prediction for the probability density function under shear flow conditions.

On approach of the gas-liquid critical point, interactions become very long ranged. This leads, for example, to the divergence of the turbidity. In addition, the gradient diffusion coefficient tends to zero so that the dynamics of the system severely slows down, often referred to as critical slowing down. Due to the long ranged spatial correlations and their very slow dynamics, the microstructural order near the gas-liquid critical point is very sensitive to shear flow. For very small shear rates the turbidity can go down enormously, changing the sample from being white to almost transparent. This change in turbidity is directly related to the change of the microstructure due to the applied shear field. Moreover, due to critical slowing down, one observes very slow relaxation of the turbidity after cessation of the shear flow.

Due to the anisotropic nature of the microstructure under shear flow, besides a change of the turbidity, dichroism is induced by the shear flow, that is, the turbidity will depend on the polarization state of the incident light. Measurement of shear induced dichroism, resulting from scattering by the anisotropic microstructure, is a sensitive test for the theoretically predicted microstructure under shear flow. This chapter

presents experimental data on shear induced dichroism as a function of shear rate and the distance from the critical point. As far as we know, this is the first systematic investigation of shear induced dichroism near the gas-liquid critical point. In ref.[1] a single measurement of dichroism in a near critical binary fluid is briefly discussed.

The present study is aimed at the understanding of the critical behaviour of dichroism in systems under shear flow, on the basis of the solution of the fundamental equation of motion referred to above. The relevant probability density function is the pair-distribution function, the Fourier transform of which is the structure factor. There are a number of theoretical approaches to obtain an expression for the pair-distribution function for systems under shear flow [2-6]. In this paper we concentrate on an expression for the structure factor that is believed to be valid for colloidal systems consisting of spherical particles close to their gas-liquid critical point. This theoretical prediction is a mean-field result [7-9]. No theory exists yet that is valid beyond mean-field.

Experimentally we find that the shear induced dichroism increases on approach of the critical point, in accordance with mean-field predictions, but unexpectedly decreases again on very close approach of the critical point. Moreover we find no critical slowing down of the relaxation dynamics of dichroism after cessation of shear flow, right up to the critical point. This is in sharp contrast with the turbidity, which diverges on approach of the critical point, and whose relaxation is severely slowed down.

The colloidal system used is a mixture of spherical colloidal particles and polymers, dissolved in cyclohexane. The added polymer induces attractions, commonly referred to as “depletion attractions” [10-12], which attractions give rise to a gas-liquid critical point [13].

This chapter is organised as follows. Section 2.2 provides the theoretical background that is necessary to understand the data interpretation. In section 2.3 the colloidal system is discussed together with the experimental set up that was used to measure dichroism. In section 2.4 the experimental results and comparison with theoretical predictions are presented. Section 2.5 contains some concluding remarks.

2.2 THEORETICAL BACKGROUND

This section contains the necessary theoretical background for the data interpretation that is used in the experimental section. First of all the relation between the

correlation length and the turbidity of a quiescent, unsheared system is discussed. This relation will be used in experiments to determine the distance from the critical point in terms of the correlation length by means of turbidity measurements. Secondly, the shear distorted stationary structure factor under shear flow is discussed, and the shear induced dichroism will be expressed as a wavevector integral over this structure factor. This leads to a scaling relation that will be tested experimentally in section 2.4. Thirdly, the relaxation dynamics of the turbidity and shear induced dichroism, after cessation of the shear flow, is addressed.

The flow that we will consider here is chosen in the y -direction, with its gradient in the z -direction. That is, the flow velocity is equal to $\mathbf{u} = \mathbf{\Gamma} \cdot \mathbf{r}$, where $\mathbf{\Gamma}$ is the velocity gradient tensor,

$$\mathbf{\Gamma} = \dot{\gamma} \begin{pmatrix} 0 & 0 & 0 \\ 0 & 0 & 1 \\ 0 & 0 & 0 \end{pmatrix} \quad (2.1)$$

with $\dot{\gamma}$ the shear rate. The direction of the incident laser beam is along the z -direction, and the polarization state of the light is specified by the angle α of the electric field with the x -axis. This geometry is sketched in Figure 2.1.

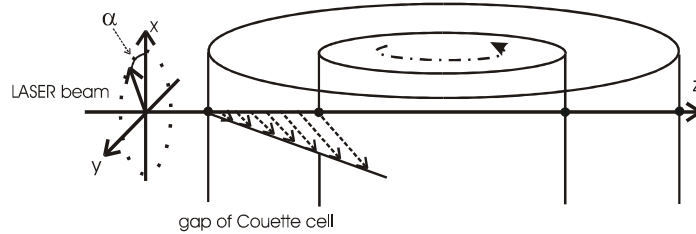


Figure 2.1: Geometry used in the theoretical discussion and experimental set-up.

2.2.1 RELATION BETWEEN THE SCATTERED INTENSITY AND THE TURBIDITY

The turbidity measures the loss of intensity as a light beam passes the sample. It is related to the thickness l of the sample, the incident intensity I_0 and the intensity I_s after passing the sample by Lambert-Beer's law,

$$I_s = I_0 \exp\{-\tau l\} \quad (2.2)$$

Since the intensity loss is solely due to scattering of light by the colloidal particles, there is a relation between the turbidity τ and the integrated scattered intensity, which in turn is proportional to $P(k)S(\mathbf{k})$ with $P(k)$ the formfactor and $S(\mathbf{k})$ the structure factor. This relation reads (see ref. [7] for the derivation of this equation),

$$\tau = \frac{C_\tau}{k_0^2} \int_0^{2\pi} d\varphi \int_0^{2k_0} dk k P(k) S(\mathbf{k}) \times \left[(-\cos \alpha \sin \varphi + \sin \alpha \cos \varphi)^2 + (\cos \alpha \cos \varphi + \sin \alpha \sin \varphi)^2 \left\{ 1 - \left(\frac{k}{k_0} \right)^2 + \frac{1}{4} \left(\frac{k}{k_0} \right)^4 \right\} \right] \quad (2.3)$$

where the optical constant C_τ is equal to,

$$C_\tau = \frac{k_0^4}{(4\pi)^2} \bar{\rho} V_p^2 \left| \frac{\bar{\epsilon}_p - \epsilon_f}{\epsilon_f} \right|^2$$

with $k_0 = 2\pi/\lambda_{\text{wav}}$ (λ_{wav} is the wavelength of the light in the dispersion), $\bar{\rho}$ the colloidal particle number density, V_p the volume of a colloidal particle, $\bar{\epsilon}_p$ the volume averaged dielectric constant of the colloidal particles, and ϵ_f the dielectric constant of the fluid. The wavevector \mathbf{k} is equal to $-k_0 (\sin \theta \cos \varphi, \sin \theta \sin \varphi, \cos \theta - 1)$. The magnitude $k = |\mathbf{k}|$ of the wavevector is equal to $2k_0 \sin \frac{\theta}{2}$, in which θ is the angle between \mathbf{k} and the z-axis. In the integration in eq.(2.3) with respect to the spherical coordinates φ and θ , the θ -integration is transformed to k -integration.

In case the structure factor is isotropic, that is, when $S(\mathbf{k})$ is a function of the magnitude $k = |\mathbf{k}|$ only, the φ -integration in eq.(2.3) can be done analytically rendering the turbidity independent of α . For such isotropic structures there is no polarization dependence of the turbidity. Shear flow renders the structure factor anisotropic, leading to an α -dependent turbidity. Shear flow thus induces dichroism through its effect on the microstructure of the suspension of spherical colloidal particles. For non-spherical colloidal particles there is an additional contribution to dichroism that stems from the orientation dependence of the formfactor. In the present work, where spherical colloids are used, such alignment-dichroism is absent.

2.2.2 RELATION BETWEEN THE TURBIDITY AND CORRELATION LENGTH

The relevance of the relation between the turbidity τ and the correlation length ξ for the work described in the present chapter is, that when a dichroism measurement has been done, the correlation length is obtained through a turbidity measurement on the quiescent, non-sheared suspension. Once the relation between the turbidity and the correlation length is established, such a turbidity measurement suffices to characterise the distance from the critical point in terms of the correlation length, which is also an important input when comparing with theory.

The structure factor for a non-sheared, equilibrium suspension near the critical point is the Ornstein-Zernike structure factor,

$$S^{eq}(k) = \frac{1}{\beta\Sigma} \frac{\xi^2}{1 + (k\xi)^2} \quad (2.4)$$

where $\beta = 1/k_B T$ (k_B is the Boltzmann constant and T is the temperature), and Σ is a constant related to the Cahn-Hilliard square-gradient coefficient. Furthermore, ξ is the correlation length, which measures the largest distance over which particles are correlated. Eq.(2.4) is a valid expression for the structure factor for small wavevectors, $k < 2\pi/R_V$, where R_V is the range of the pair-interaction potential. For such small wavevectors the formfactor in eq.(2.3) for the turbidity is almost equal to 1. Correction terms can be obtained by Taylor expansion of the formfactor of optically homogeneous colloidal spheres,

$$P(k) = \left[3 \frac{\sin(ka) - ka \cos(ka)}{(ka)^3} \right]^2 = 1 - \frac{1}{5}(ka)^2 + \frac{3}{175}(ka)^4 + O((ka)^6) \quad (2.5)$$

Substitution of eqs.(2.4),(2.5) into eq.(2.3) for the turbidity gives,

$$\begin{aligned} \tau^{eq}(\sigma) \propto \sigma \left[\frac{2\sigma^2 + 2\sigma + 1}{\sigma^3} \ln(1 + 2\sigma) - 2 \frac{(1 + \sigma)}{\sigma^2} \right. \\ \left. + \frac{2}{5} a^2 k_0^2 \left\{ \frac{2\sigma^2 + 2\sigma + 1}{\sigma^4} \ln(1 + 2\sigma) - \frac{\frac{8}{3}\sigma^2 + 2\sigma + 2}{\sigma^3} \right\} + O((ak_0)^4) \right] \end{aligned} \quad (2.6)$$

where $\sigma = 2(k_0\xi)^2$. This equation has been derived by Puglielli and Ford [14].

The Ornstein-Zernike structure factor (eq.(2.4)) is the contribution to the structure factor due to critical, long range correlations only, and does not contain the non-critical contributions to the scattered intensity. For the small wavevectors of interest here, this non-critical background is virtually a constant, not only independent of the wavevector but also independent of the concentration within the vicinity of the critical point. This leads to a non-critical additive, constant contribution to the turbidity in eq.(2.6).

Alternatively, the correlation length can be measured from small angle light scattering experiments using eq.(2.4) for the structure factor. Since the scattered intensity is directly proportional to the structure factor at sufficiently small angles, this equation shows that a plot of $1/S(k)$ versus k^2 is a straight line with a slope equal to $\beta\Sigma$ and an intercept equal to $\beta\Sigma\xi^{-2}$. The ratio of the intercept and slope thus equals the squared reciprocal correlation length. As mentioned above, the Ornstein-Zernike

structure factor accounts only for the critical contribution to the structure factor. In experimental practice we shall have to subtract a constant, wavevector independent background intensity.

2.2.3 CRITICAL MICROSTRUCTURE UNDER SHEAR FLOW

The shear induced turbidity and dichroism can be obtained from eq.(2.3) once the structure factor under shear flow is known. Concentration and shear rate dependent turbidity and dichroism measurements actually serve as a tool to test theoretical predictions for the structure factor under shear flow. Notable theoretical predictions for the shear rate dependence of the structure factor can be found in refs.[2-6]. Here we discuss a theory that is specialised to colloidal systems close to their gas-liquid critical point [7-9].

Starting point is the Smoluchowski equation, which is the fundamental kinetic equation referred to in the introduction. This is the equation of motion for the probability density function of the position coordinates of the colloidal particles. From this kinetic equation one obtains the following equation of motion for the structure factor under stationary shear flow (for the geometry sketched in Figure 2.1),

$$\left[\frac{\partial}{\partial t} - \dot{\gamma} k_2 \frac{\partial}{\partial k_3} \right] S(\mathbf{k}; t | \dot{\gamma}) = -2D^{eff}(k)k^2 [S(\mathbf{k}; t | \dot{\gamma}) - S^{eq}(k)] \quad (2.7)$$

Note that in directions where $k_2 = 0$, this equation predicts that there is no effect of the shear flow on the microstructure. Here D^{eff} is an effective diffusion coefficient which is equal to,

$$D^{eff}(k) = D_0 \beta \left(\frac{d\Pi}{d\bar{\rho}} + k^2 \Sigma \right) \quad (2.8)$$

with D_0 the Stokes-Einstein diffusion coefficient of a non-interacting, free colloidal particle, Π is the osmotic pressure (of which the derivative with respect to the number density $\bar{\rho}$ is taken), and Σ is a constant that is related to the Cahn-Hilliard square gradient coefficient (the same constant occurs in eq.(2.4) for the Ornstein-Zernike structure factor). The stationary solution $S(\mathbf{k} | \dot{\gamma})$ of this equation of motion is conveniently expressed in terms of the relative structure factor deformation,

$$\Psi(\mathbf{k} | \lambda) = \frac{S(\mathbf{k} | \dot{\gamma}) - S^{eq}(k)}{S^{eq}(k) - 1} \quad (2.9)$$

As will become clear later in this subsection, this quantity is well-behaved for all wavevectors right up to the critical point. From eq.(2.7) one finds,

$$\Psi(\mathbf{k} | \lambda) = \frac{1}{\lambda K_2} \int_{K_3}^{+\infty} dX (K^2 - K_3^2 + X^2)(K_3^2 - X^2) \exp\left(-\frac{F(\mathbf{K} | X)}{\lambda K_2}\right) \quad (2.10)$$

where the dimensionless wavevector $\mathbf{K} = \mathbf{k}\xi$ is introduced and,

$$F(\mathbf{K} | X) = (X - K_3)(K^2 - K_3^2)(1 + K^2 - K_3^2) + \frac{1}{3}(X^3 - K_3^3)(1 + 2K^2 - 2K_3^2) + \frac{1}{5}(X^5 - K_3^5) \quad (2.11)$$

Here, K_j is the j^{th} component of the dimensionless wavevector. The upper integration limit in eq.(2.10) is $+\infty$ when $\lambda K_2 > 0$ and $-\infty$ when $\lambda K_2 < 0$. Furthermore λ is a dressed Peclet number,

$$\lambda = \frac{\dot{\gamma} \xi^2}{2D^{\text{eff}}(k=0)} = \frac{1}{\beta \Sigma} \frac{\dot{\gamma} \xi^4}{2D_0} \quad (2.12)$$

In the second equation in eq.(2.12) we used that $\xi = \sqrt{\Sigma/[d\Pi/d\bar{\rho}]}$. Note that close to the critical point $d\Pi/d\bar{\rho}$ is small, so that D^{eff} is small in comparison to the free diffusion coefficient D_0 for small wavevectors. This reflects critical slowing down of long wavelength concentration fluctuations.

The dressed Peclet number λ in eq.(2.12) measures the effect of shear flow on the long ranged, critical microstructural order. When $\lambda < 1$ the critical microstructural order is only slightly affected, while for $\lambda > 1$ the effect of shear flow is significant. What is neglected in the derivation of eq.(2.10), is distortion of microstructural order extending over distances equal or less than the range R_V of the pair-interaction potential. The extent to which such short ranged microstructural order is affected by shear flow is measured by the so-called bare Peclet number,

$$Pe^0 = \frac{\dot{\gamma} R_V^2}{2D_0} \quad (2.13)$$

Eq.(2.10) is valid whenever $Pe^0 \ll 1$. Since $\xi < R_V$ and $D^{\text{eff}} < D_0$, the dressed Peclet number can be large, also for small bare Peclet numbers. This is due to the fact that large structures are more easily affected by shear flow than small structures, and that long wavelength critical fluctuations are much slower than density fluctuations with small wavelengths ($\sim R_V$). One can thus distinguish three shear rate regimes,

$$\begin{aligned} \lambda < 1; \quad Pe^0 \ll 1 & \quad \text{weak shear flow} \\ \lambda > 1; \quad Pe^0 \ll 1 & \quad \text{strong shear flow} \\ \lambda > 1; \quad Pe^0 \lll 1 & \quad \text{very strong shear flow} \end{aligned}$$

Eq.(2.10) for the structure factor distortion is valid in the weak and strong shear regime, but not in the very strong shear regime.

The result eq.(2.10) is valid only in the mean-field region around the critical point. This is due to a linearization of equations of motion with respect to the total-correlation function $h(r)$ for large distances r between two colloidal particles. In fact, terms $\sim h^2$ are neglected against the term $(\beta d\Pi/d\bar{\rho})h$ for large distances r . This is only a valid procedure when $\beta d\Pi/d\bar{\rho}$ is not extremely small, that is, when the distance to the critical point is not too small. The above predictions are therefore only valid in the mean-field region.

In the derivation of eq.(2.10) hydrodynamic interactions between colloidal particles have been neglected. Furthermore, a closure relation has been used in order to express the three-particle correlation function in terms the pair-correlation function. This approximate closure relation is reminiscent of the classic super-position closure relation.

It can be shown rigorously, that the displacement of the critical point for colloidal systems is proportional to $(Pe^0)^{1/\gamma}$, where $\gamma = 1.23$ is the critical exponent of the compressibility of the quiescent system [15]. The displacement of the critical point for spherical colloids is related to the distortion of the pair-correlation function for short distances, smaller than the range of the pair-interaction potential, and is therefore a function of the bare Peclet number Pe^0 . For the experiments described here, $Pe^0 \leq 0.08$, so that the displacement of the critical point is not important for the present work.

Numerical results for the relative structure factor distortion and the structure factor itself are plotted in Figure 2.2. In some directions there is enhancement of structure whereas in other directions destruction of structure is observed, as can be seen from the plots of Ψ . This can be understood by decomposing a simple shear flow in its elongational and rotational contributions. The elongational contribution tends to enhance structure along the $y = -z$ direction, and diminishes structure in the direction where $y = z$. These directions correspond to the directions $k_2 = -k_3$ and $k_2 = k_3$, respectively. Note that Ψ is found to be finite right up to the critical point, which is the reason for introducing this quantity.

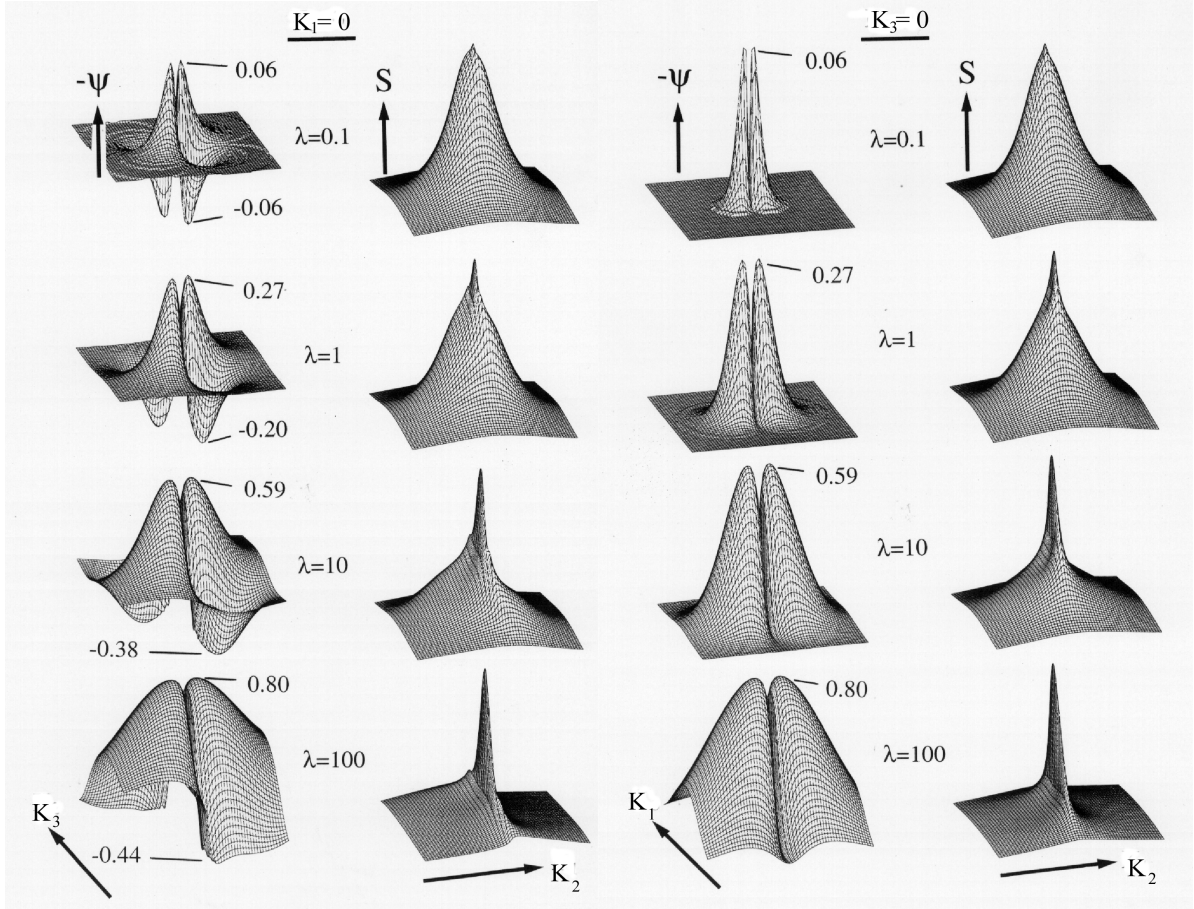


Figure 2.2: Plots of (minus) the relative structure factor distortion $\Psi(\mathbf{k} | \lambda)$ and the structure factor $S(\mathbf{k} | \dot{\gamma})$, at $K_1 = 0$ and $K_3 = 0$, for various values of λ as indicated in the figure. K_1, K_2 and K_3 values range from -3 to $+3$. The minimum and maximum values of Ψ are indicated in the figure.

2.2.4 SHEAR INDUCED DICHOISM

The change of the turbidity on applying a shear flow follows from eqs.(2.3),(2.4),(2.9) and (2.10). Transforming to the dimensionless $K = k\xi$ variable, and disregarding the small $(K/K_0)^4$ -terms in eq.(2.3), the turbidity, relative to the turbidity for $\alpha = \pi/2$, is found to be equal to,

$$\begin{aligned} \Delta\tau(\dot{\gamma} | \alpha) &\equiv \tau(\dot{\gamma} | \alpha) - \tau(\dot{\gamma} | \alpha = \frac{\pi}{2}) \\ &= -\frac{C_\tau}{(k_0 R_V)^4} \frac{1}{(\beta \Sigma / R_V^2)^{3/2}} \sqrt{Pe^0(\dot{\gamma})} \left[\cos^2(\alpha) D_{cc}(\lambda) + 2 \sin(\alpha) \cos(\alpha) D_{sc}(\lambda) \right] \end{aligned} \quad (2.14)$$

where the scaling functions D_{sc} and D_{cc} are given by,

$$D_{cc}(\lambda) = \frac{1}{\sqrt{\lambda}} \int_0^{2\pi} d\varphi \int_0^{\infty} dK \frac{K^3}{1+K^2} \Psi^*(K, \varphi | \lambda) (\cos^2 \varphi - \sin^2 \varphi) \quad (2.15)$$

and,

$$D_{sc}(\lambda) = \frac{1}{\sqrt{\lambda}} \int_0^{2\pi} d\varphi \int_0^{\infty} dK \frac{K^3}{1+K^2} \Psi^*(K, \varphi | \lambda) \sin(\varphi) \cos(\varphi) \quad (2.16)$$

The upper integration limit $2k_0$ in eq.(2.3) is replaced here by ∞ . This can be done for systems under shear flow, where the structure factor distortion peaks at small values of K , and tends to 0 for large wavevectors much faster than $1/K^2$ (except in directions where $K_2 \approx 0$) as can be seen from the plots of $S(\mathbf{k} | \dot{\gamma})$ in Figure 2.2. In fact, numerical evaluation of the integrals in eqs.(2.15) and (2.16) shows that the integrals converge to within a fraction of 1 % for an upper integration limit of typically $K \approx 5$. For the same reason, Ψ is replaced here by Ψ^* , which is equal to Ψ with the angle θ of \mathbf{k} with the z-axis taken into account to leading order, that is,

$$\Psi^*(K, \varphi | \lambda) = \Psi(\mathbf{K} = K(\cos \varphi, \sin \varphi, 0) | \lambda) \quad (2.17)$$

Numerical evaluation of the scaling functions reveals that for the present geometry (see Figure 2.1) $D_{sc} = 0$, to within numerical errors. Numerical results for the scaling functions are plotted in Figure 2.3. Here, the curves labelled with a ‘1’ refer to the geometry where the direction of the beam is along the vorticity direction, while ‘2’ refers to the geometry sketched in Figure 2.1. The reason for division by $\sqrt{\lambda}$ in eq.(2.15) and eq.(2.16) is that the scaling functions tend to a constant for large dressed Peclet numbers λ .

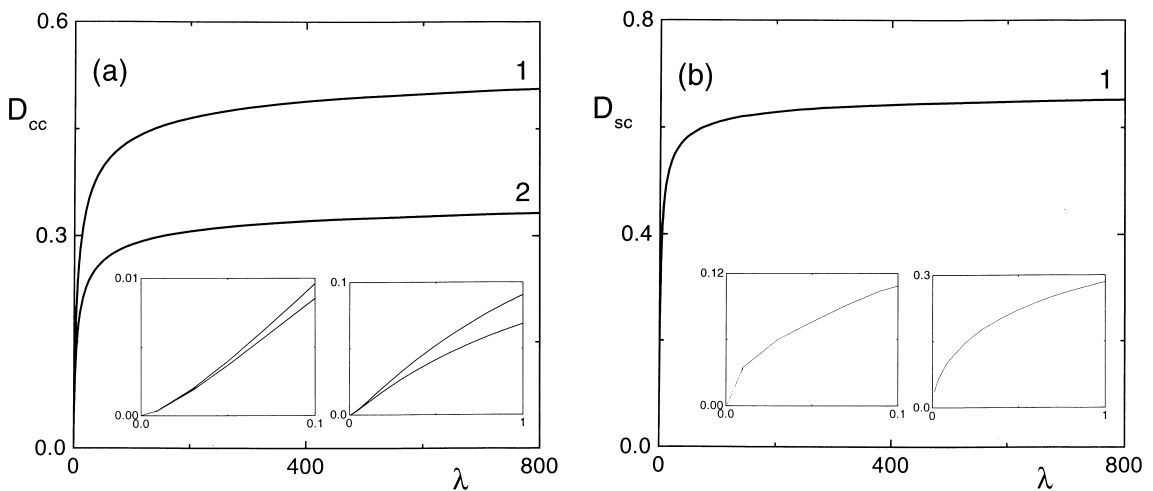


Figure 2.3: Numerical results for the scaling functions D_{cc} (a) and D_{sc} (b). The inserts show the behaviour for small values of λ , which confirms the analytically predicted behaviour as discussed in the main text, below eq.(2.18).

In the weak shear limit, where $\lambda < 1$, for the geometry ‘2’ of interest here, D_{cc} can be found by substitution of a regular expansion of the structure factor with respect to λ . To this end the expansion,

$$S(\mathbf{K} | \dot{\gamma}) = S^{eq}(K) + \lambda S^{(1)}(\mathbf{K}) + \lambda^2 S^{(2)}(\mathbf{K}) + \dots \quad (2.18)$$

is substituted into the stationary form of eq.(2.7). Equating terms of equal powers in λ reveals that, for the geometry sketched in Figure 2.1, $S^{(1)} \sim \sin \varphi$ and $S^{(2)} \sim \cos^2 \varphi$. The φ -integration in eq.(2.15) for D_{cc} renders a linear term in λ equal to 0, so that, $D_{cc} \sim \lambda^{3/2}$. Dichroism thus varies like $\dot{\gamma}^2$ for small dressed Peclet numbers. The shear induced dichroism in the present geometry is thus inherently non-linear. The small shear rate behaviour of D_{cc} is plotted in the insert of Figure 2.3 a. The function D_{sc} , relevant for the geometry ‘1’, varies like $\lambda^{1/2}$ for small λ . In the ‘1’ geometry, there is thus a non-zero linear-response. Note the very small range of λ ’s in Figure 2.3 where the leading λ -dependence is dominant.

The regular expansion eq.(2.18) is invalid in a region in wavevector space around $\mathbf{k} = \mathbf{0}$ of width $\sim \sqrt{\lambda}$, even for small values of λ . The reason is that eq.(2.7) is singularly perturbed by the shear flow contribution. In this so-called (mathematical) boundary layer at $\mathbf{k} = \mathbf{0}$ there is never linear shear flow response of the structure factor. The regular expansion eq.(2.18) does make sense, however, when used in integrals like in eqs.(2.15) and (2.16) for the scaling functions, since the width of the boundary layer vanishes for small shear rates, and therefore contributes only little to the value of the integral. In addition, the integrand in eqs.(2.15), (2.16) vanishes for zero wavevectors, so that the error that is made by using the regular expansion is further diminished.

The maximum variation of the turbidity on variation of α , multiplied by $\lambda_{wav}/2\pi$ defines the dichroism $\Delta n''$. From eq.(2.14) we thus finally find the following expression for the shear induced dichroism for the geometry ‘2’ near the gas-liquid critical point,

$$\Delta n'' = \frac{C_\tau}{(k_0 R_V)^4} \frac{1}{(\beta \Sigma / R_V)^{3/2}} \frac{\sqrt{Pe^0(\dot{\gamma})}}{k_0} D_{cc}(\lambda) \quad (2.19)$$

This result predicts scaling in the sense that dichroism depends on the shear rate and the distance from the critical point only through the dressed Peclet number λ , except

for the trivial prefactor $\sqrt{Pe^0(\dot{\gamma})}$. This scaling implies that experimental data for $\Delta n''/\sqrt{\dot{\gamma}}$ taken at various shear rates and distances from the critical point should collapse onto a single master curve when plotted versus $\dot{\gamma}\xi^4$, the form of which master curve is given by the scaling function in Figure 2.3 a (geometry ‘2’).

2.2.5 TIME DEPENDENT TURBIDITY AND DICHROISM

Consider an experiment where a stationary shear flow is suddenly switched off, at time $t = 0$, say. The solution of eq.(2.7) for this situation is a single exponential function of time, where the structure factor $S(\mathbf{k} | \dot{\gamma})$ in eq.(2.9) is now the structure factor in the stationary state, before cessation of the flow,

$$S(\mathbf{K}; t | \dot{\gamma}) = (S^{eq}(K) - 1) \Psi(\mathbf{K} | \lambda) \exp\left(-K^2 [1 + K^2] \frac{\dot{\gamma} t}{\lambda}\right) \quad (2.20)$$

The dimensionless variables as defined in subsection 2.2.3 are introduced here. The time dependent behaviour of the turbidity is immediately found by substitution of eq.(2.20) into eq.(2.3), neglecting terms of order $(K/K_0)^2$,

$$\begin{aligned} \tau(\dot{\gamma} | t) - \tau^{eq} &= -\frac{C_\tau}{(k_0 R_v)^4} \frac{1}{(\beta \Sigma / R_v^2)^{3/2}} \times \\ &\int_0^{2\pi} d\varphi \int_0^\infty dK \frac{K}{1 + K^2} \Psi^*(K, \varphi | \lambda) \exp\left[-K^2 (1 + K^2) \frac{\dot{\gamma} t}{\lambda}\right] \end{aligned} \quad (2.21)$$

Similarly as in subsection 2.2.4, the polarization dependence of the turbidity is given by,

$$\begin{aligned} \Delta\tau(\dot{\gamma} | \alpha | t) &\equiv \tau(\dot{\gamma} | \alpha | t) - \tau(\dot{\gamma} | \alpha = \frac{\pi}{2} | t) \\ &= -\frac{C_\tau}{(k_0 R_v)^4} \frac{1}{(\beta \Sigma / R_v^2)^{3/2}} \sqrt{Pe^0(\dot{\gamma})} \times \\ &[\cos^2(\alpha) D_{cc}(\lambda | \dot{\gamma} t) + 2 \sin(\alpha) \cos(\alpha) D_{sc}(\lambda | \dot{\gamma} t)] \end{aligned} \quad (2.22)$$

where,

$$\begin{aligned} D_{cc}(\lambda | \dot{\gamma} t) &= \frac{1}{\sqrt{\lambda}} \int_0^{2\pi} d\varphi \int_0^\infty dK \frac{K^3}{1 + K^2} (\cos^2 \varphi - \sin^2 \varphi) \times \\ &\Psi^*(K, \varphi | \lambda) \exp\left(-K^2 [1 + K^2] \frac{\dot{\gamma} t}{\lambda}\right) \end{aligned} \quad (2.23)$$

and,

$$D_{sc}(\lambda | \dot{\gamma}t) = \frac{1}{\sqrt{\lambda}} \int_0^{2\pi} d\varphi \int_0^{\infty} dK \frac{K^3}{1+K^2} \sin(\varphi) \cos(\varphi) \times \Psi^*(K, \varphi | \lambda) \exp\left(-K^2 [1+K^2] \frac{\dot{\gamma}t}{\lambda}\right) \quad (2.24)$$

Numerical evaluation of eqs.(2.23) and (2.24) leads to a pronounced difference in relaxation times for the turbidity and dichroism after cessation of the shear flow. Dichroism relaxes fast in comparison to the turbidity. Formally, this is due to the factor K^3 in the integrand in eqs.(2.23) and (2.24) for the dichroism, as compared to the factor K in eq.(2.21) for the turbidity. The dynamics of dichroism is connected to larger wavevectors as compared to the turbidity. The dynamics of concentration fluctuations pertaining to these larger wavevectors is fast as compared to small wavevectors.

2.3 EXPERIMENTAL

2.3.1 COLLOIDAL SYSTEM

The system used in this study consists of colloidal silica particles grafted with stearyl alcohol. The solvent is cyclohexane. Polydimethylsiloxane (PDMS) is added to induce depletion attractions between the colloidal particles which give rise to a gas-liquid critical point. The silica particles were synthesized by the method of Stöber [16]. The spheres have an average diameter of 102 nm, as determined by dynamic light scattering. The polydispersity, determined by Transmission Electron Microscopy, was found to be around 16 %. The specific mass ρ of the silica particles, that relates the volume fraction Φ to the mass concentration c as $\Phi = c/\rho$, was determined by Ubbelohde measurements, using Einstein's formula $\eta_r = 1 + 2.5\Phi$, which relates the shear viscosity η_r to the volume fraction Φ of spheres. The specific mass ρ was found to be 1.863 g/ml. The polymer PDMS that we used has a molar weight of 204 kg/mol. When dissolved in cyclohexane, the spherical coils have a radius of gyration of around 26 nm (at 25°C).

To determine the phase diagram, a number of samples with various, fixed PDMS to silica concentration ratios were prepared. By adding or evaporating solvent we moved along so-called dilution lines in the phase diagram, as depicted in Figure 2.4. The binodal was found by visual inspection of the samples for the formation of an interface and the time it takes before an interface could be seen. Close to the critical

point, phase separation could take a few hours due to the fact that the density difference between the gas and liquid phases becomes very small. The experimentally determined phase diagram is shown in Figure 2.4. The critical point was found by locating the point on the binodal where, after phase separation, the volumes of the two phases are equal. Close to the critical point phase separation occurred after about 2 hours. All measurements are performed on a sample on the dilution line that intersects the critical point. The distance from the critical point is varied by gently evaporating or adding solvent.

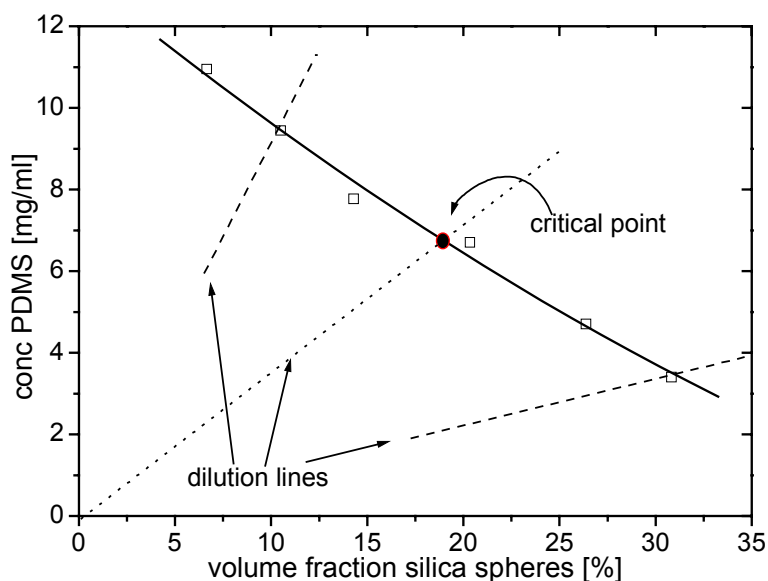


Figure 2.4: Experimental phase diagram (polymer to colloid diameter ratio 0.51). The binodal points \square are obtained by visual observation.

2.3.2 EXPERIMENTAL SET UPS

The important parameter that characterises the distance from the critical point, which is also an important input when comparing with theory, is the correlation length. When performing a dichroism experiment one could measure the concentration of the sample, and from that derive the correlation length, after the relation between the correlation length and concentration has been established independently. The relevant differences in concentration, however, are so small that the determination of the concentration would be far too inaccurate. Before and after each dichroism experiment we therefore performed a turbidity measurement on the quiescent, unsheared sample, and determined the correlation length from the turbidity. To this

end we first have to establish the relation between the turbidity and the correlation length. The experimental set up for this purpose is sketched in Figure 2.5.

The laser beam first passes two polaroid's in order to be able to adjust the intensity of the beam. A non-polarising beam splitter is used to determine the intensity of the incident light with detector 1. The sample is immersed in a thermostating optical matching bath, to prevent scattering from optical imperfections of the cuvette. The scattered light intensity is measured by means of a photodiode array camera which is positioned in the focal plane of the optical bath. The scattering angle range is 2-6 degrees. The intensity of the beam that passed the sample is reflected by a mirror to detector 2. A circular pinhole with a diameter of 0.3 mm has been used to prevent detection of scattered light by detector 2. The ratio of the intensities of the detectors 1 and 2 is then recorded for an experiment with the colloidal sample and only solvent, respectively. These two intensity ratios determine the turbidity of the colloidal sample through Lambert-Beer's law eq.(2.2). The pathlength of the cuvettes is typically 0.2 cm.

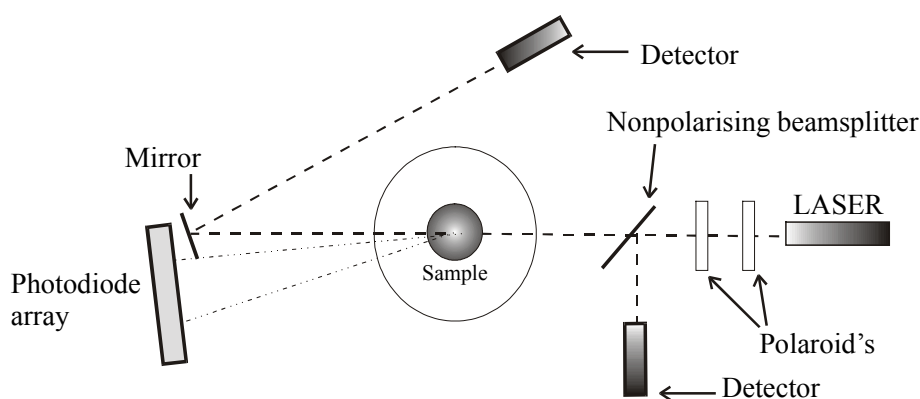


Figure 2.5: Experimental set-up for the determination of the relation between the turbidity and the correlation length.

The dichroism set up is based on the design by Fuller [17, 18]. The set up was adjusted to be able to also measure the turbidity of the system, for reasons discussed above. In our set up, the rotating $1/2$ waveplatelet is mounted on a dentist drill, which accomplishes a rotational speed of about 4 kHz. The shear cell is a home made optical couette cell with a gapwidth of 2.47 mm, which is placed a thermostating, optically matching bath. See Chapter 1 for a more detailed description of the dichroism set up and the shear cell.

Before an actual dichroism experiment was started, the colloid-polymer mixture was left to equilibrate for at least 30 min. in the thermostated, optical bath. The turbidity is

measured before and after each dichroism experiment in order to verify that evaporation of solvent during the experiment is insignificant. It turned out that evaporation is insignificant over periods of several hours.

2.4 EXPERIMENTAL RESULTS AND DISCUSSION

2.4.1 CORRELATION LENGTH DEPENDENCE OF THE TURBIDITY

Figure 2.6 shows the reciprocal intensity versus the wavevector k squared, for a sample with the critical colloid to polymer ratio, for various distances from the critical point (see the dilution line in Figure 2.4). The solid lines in this figure are curves fitted to eq.(2.4), where the non-critical background contribution to the intensity is used as an additional fitting parameter. Relatively far from the critical point the curves are virtually straight lines, but closer to the critical point, curves deviate from a straight line. The reason for this is the large variation of the *relative* contribution of the non-critical background intensity: for small wavevectors, where the critical scattered intensity is very large, the relative contribution of the background intensity is much smaller than for the larger wavevectors. Further away from the critical point, the *relative* background contribution becomes almost wavevector independent and renders Orstein-Zernike plots linear. Except for the largest correlation lengths shown in Figure 2.6, the curves have the same slope. The slope is proportional to $\beta\Sigma$ so that this parameter is seen to be well-behaved near the critical point, as expected.

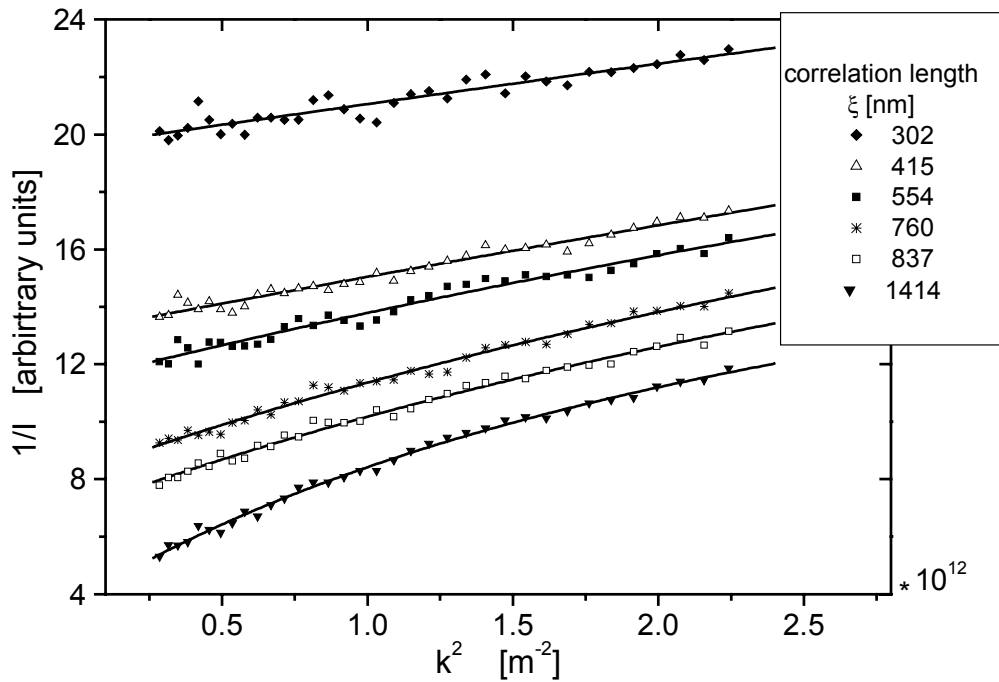


Figure 2.6: Reciprocal scattered intensity versus k^2

We found that on approach of the critical point the time needed to render the scattered intensity time independent increases. This is a manifestation of critical slowing down of the dynamics of concentration fluctuations. For very large correlation lengths (more than about 2500 nm) we observed a decrease of the measured correlation length over longer periods of time. This is illustrated in Figure 2.7. Right after homogenization of the sample, a fit to the Ornstein-Zernike structure factor, including the non-critical background contribution, yields a correlation length of 424 nm. A measurement after some hours yields a correlation length of 5011 nm. This value then decreases over a period of 8 hours to 1375 nm. The reason for this decrease in correlation length is probably that density inhomogeneities are so long-lived, as a result of severe critical slowing down, that sedimentation occurs. The system then develops large scale concentration gradients. The concentration of the part of the system from which scattered intensities are measured differs from the overall concentration, giving rise to a smaller measured correlation length. Measurements are therefore only reliable in case the correlation length is smaller than about 2500 nm.

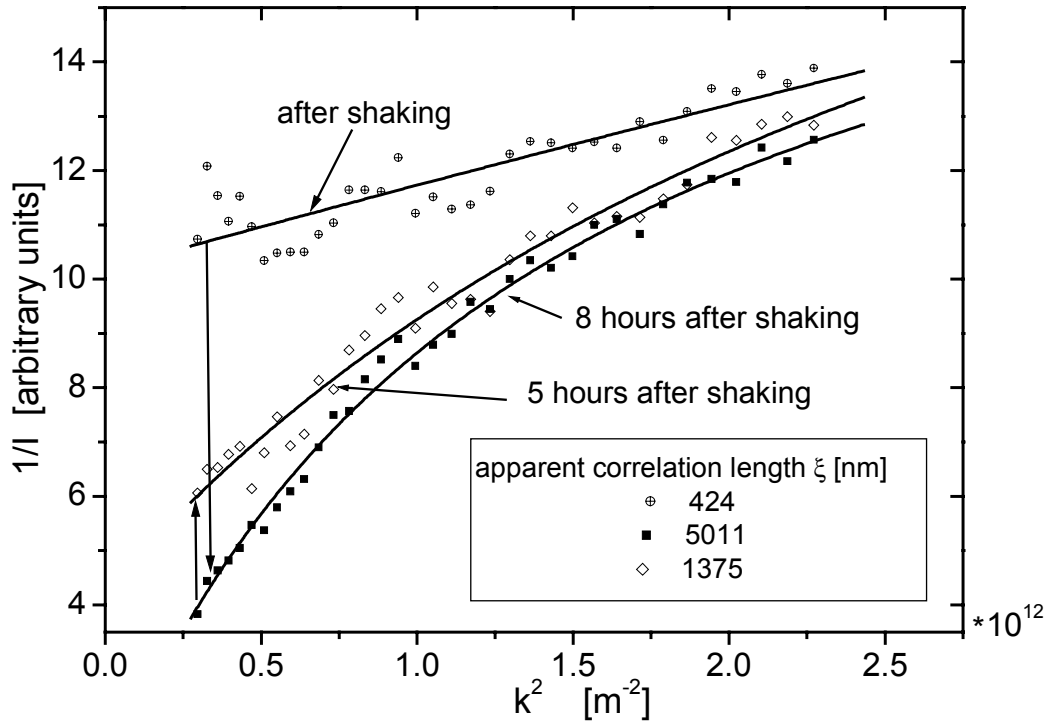


Figure 2.7: Time dependence of the reciprocal scattered intensity as a function of k^2

Figure 2.8 shows the correlation length versus the turbidity. The smallest correlation length of 250 nm is about twice as large as the range of the pair-interaction potential, which is equal to the sum of the diameters of the colloidal particles and the polymer diameter of gyration (~ 150 nm). The solid curve in Figure 2.8 is a fit to eq.(2.6). The solid curve will be used to determine the correlation length from turbidity measurements.

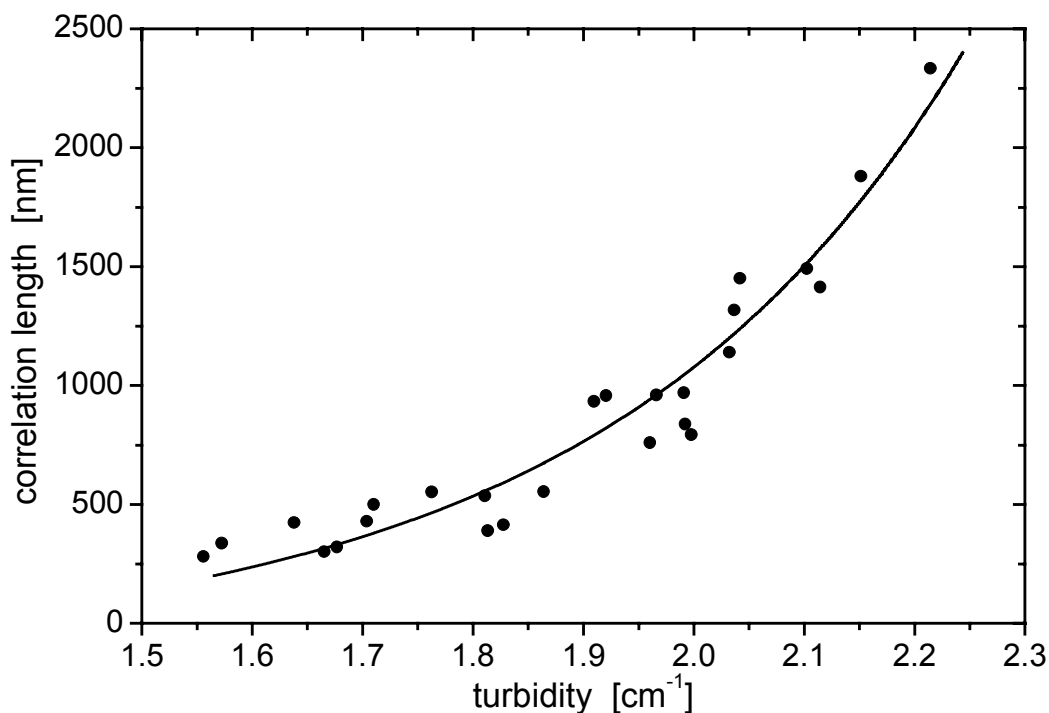


Figure 2.8: Relation between the correlation length and the turbidity

2.4.2 DICHROISM UNDER STATIONARY SHEAR FLOW

Measurements were done on a sample with the critical concentration ratio of colloid to polymer. The distance to the critical point is varied by evaporation or addition of solvent. The actual distance to the critical point in terms of the correlation length ξ is obtained from transmission measurements and Figure 2.8. A transmission measurement was done before and after the dichroism measurements were performed, in order to ensure that no significant evaporation occurred during the dichroism measurement.

Dichroism measurement results in the shear rate range of 0.1 to 34.7 s⁻¹ are plotted in Figure 2.9 for various correlation lengths. The lowest curve (dashed line) is the dichroism for a sample with silica particles only, without polymer (PDMS). This curve relates to non-critical contributions to the dichroism. As can be seen, these non-critical contributions are negligibly small as compared to critical contributions.

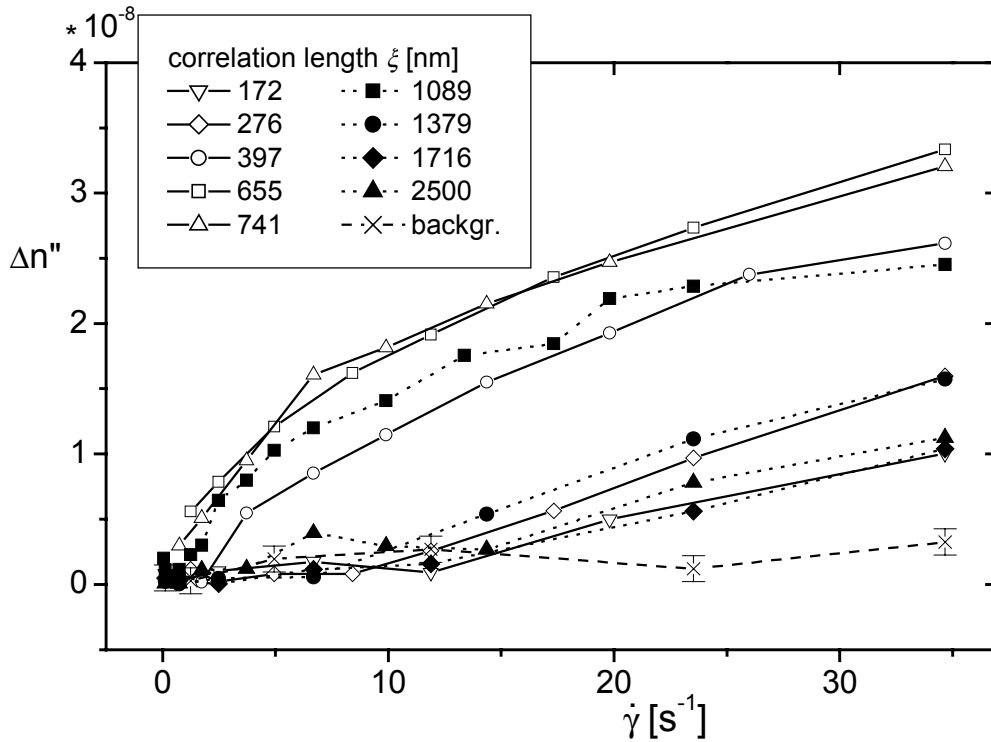


Figure 2.9: Dichroism as a function of the shear rate for various correlation lengths, as indicated in the figure. The lowest curve is the dichroism of the sample without polymer.

As can be seen from this figure, dichroism increases with increasing correlation length up to a certain correlation length after which dichroism decreases. This is made more explicit in Figure 2.10, where the dichroism at the maximum applied shear rate (34.7 s^{-1}) is plotted against the correlation length. The mean field theory described in section 2.2.4 predicts a monotonous increase of the dichroism with the correlation length. We therefore conclude that the cross-over from mean field to non-mean field behaviour occurs at a correlation length of about 750 nm.

When comparing to the theory described in section 2.2.4 we therefore have to restrict to correlation lengths less than 750 nm. Note that since in Figure 2.10 the shear rate is a constant, the location of the critical point is fixed. The decrease of dichroism can therefore not be attributed to a shear induced shift of the critical point (see also the discussion at the end of in section 2.2.3).

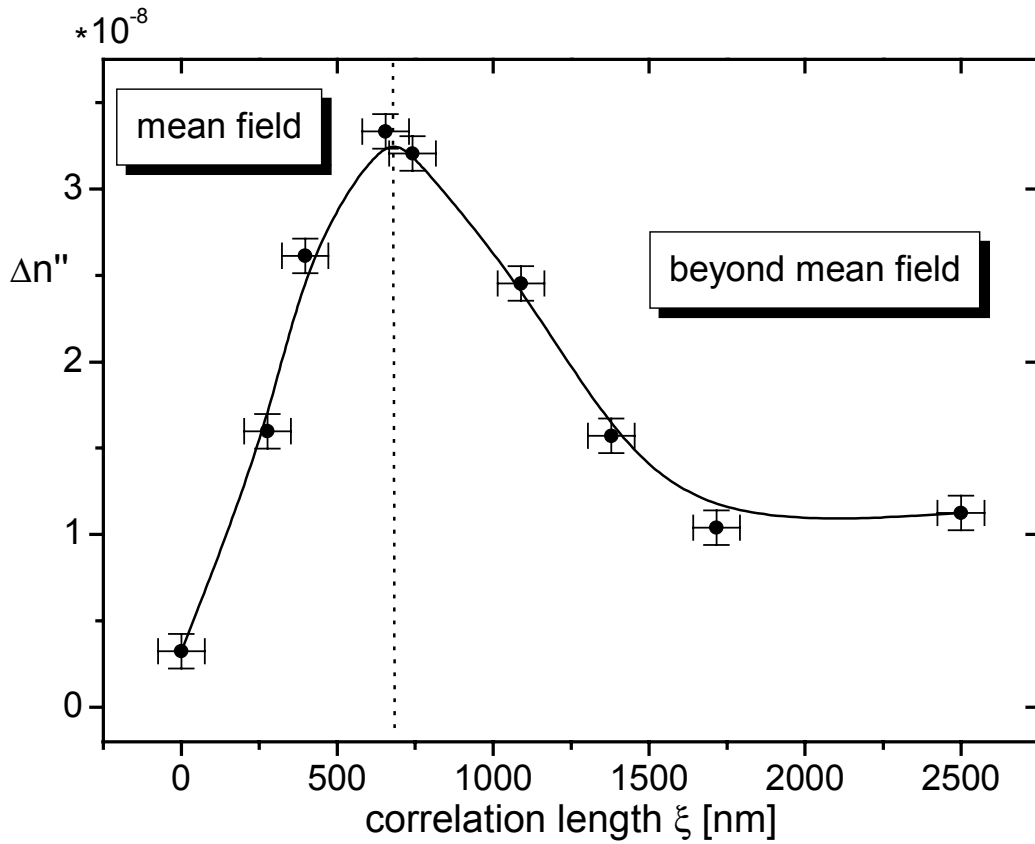


Figure 2.10: Dichroism at $\dot{\gamma} = 34.7 \text{ s}^{-1}$ versus correlation length. The vertical dotted line indicates where the cross-over from mean field to non-mean field behaviour occurs.

2.4.2.a DICHROISM IN THE MEAN FIELD REGION

The shear rate dependence of dichroism within the mean field region is plotted in the insert in Figure 2.11. Within the mean field region, dichroism is monotonously increasing with increasing shear rate. The experiments for small correlation lengths ($< 300 \text{ nm}$) suggest that the slope of the dichroism against the shear rate is 0 for small shear rates. This is in accordance with the theoretical result, $\Delta n'' \sim \dot{\gamma}^2$ for small shear rates.

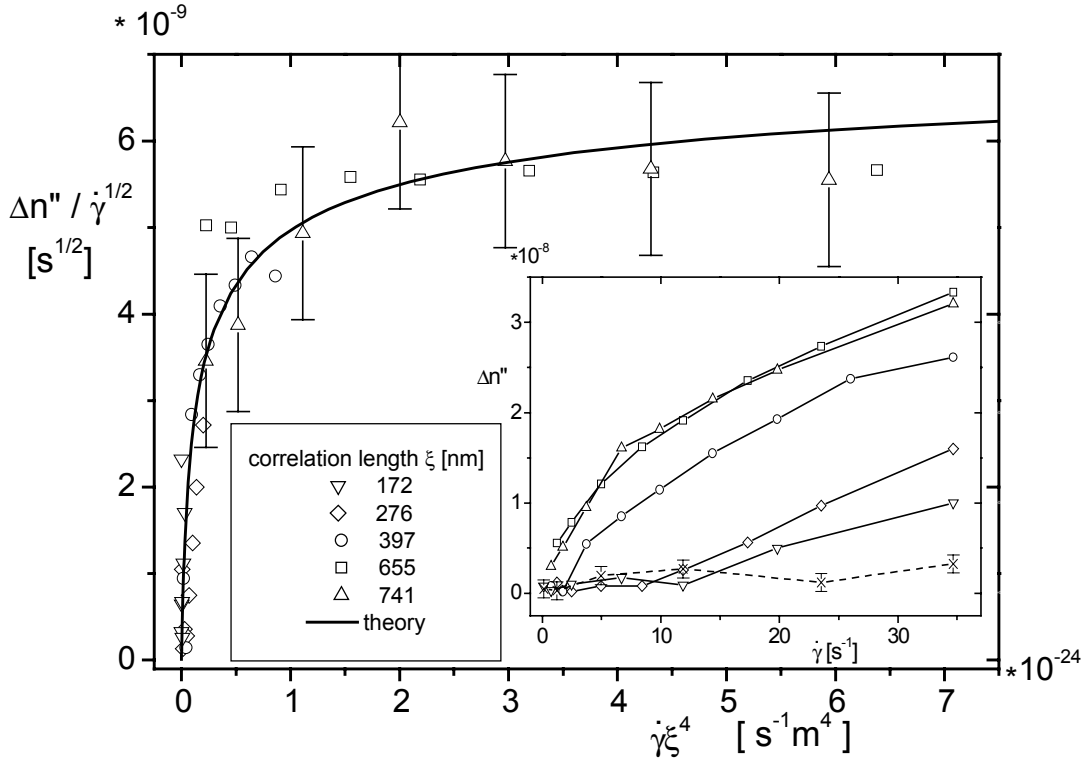


Figure 2.11: Scaling of the experimental data. The solid line corresponds to the theoretical result (eqs. (2.15) and (2.19)). Insert shows dichroism measurements in the mean field region. The dashed line is the dichroism for a sample without polymer.

The theoretical result eq.(2.19) implies that $\Delta n'' / \sqrt{\dot{\gamma}}$ is a function of the shear rate and the correlation length only through the combination $\dot{\gamma} \xi^4$. Hence, in a plot of $\Delta n'' / \sqrt{\dot{\gamma}}$ against $\dot{\gamma} \xi^4$ all experimental curves should collapse onto each other. To within experimental errors, this is indeed seen to be the case in Figure 2.11. In addition, the functional form of the dichroism scaling function eq.(2.15), as depicted in Figure 2.3, can be compared to the experimental master curve in Figure 2.11 as follows. The dressed Peclet number λ is directly proportional to $\dot{\gamma} \xi^4$. The proportionality constant between λ and $\dot{\gamma} \xi^4$ can be found by rescaling the horizontal axis in Figure 2.11, so as to obtain the best agreement between the theoretical scaling function and the experimental master curve. The vertical axis must be rescaled simultaneously. As can be seen from Figure 2.11, the theoretical scaling function agrees with the experimental master curve to within experimental errors. The rescaling factor for the horizontal axis is equal to $(2\beta\Sigma D_0)^{-1}$, according to eq.(2.12),

while the rescaling factor for the vertical axis is equal to $C_\tau \sqrt{R_V^2/2D_0} / (k_0 R_V)^4 k_0 (\beta\Sigma/R_V)^{3/2}$, according to eq.(2.13) and eq.(2.19). The scaling factors are found to be equal to $3.3 \times 10^{25} \text{ sm}^{-4}$ and $2.0 \times 10^{-8} \text{ s}^{1/2}$, respectively. From these numbers it follows that, $\beta\Sigma/R_V^2 \approx 0.14$ and $(n_p - n_f) \approx 0.025$, where n_p and n_f are the refractive index of the colloidal particles and the solvent, respectively. The former value is in accordance with a crude theoretical estimate ($\beta\Sigma/R_V^2 \sim 0.1$) [8, 19], but differs by a factor of about 10 with results obtained from earlier turbidity measurements on a similar colloidal system [20]. The refractive index difference with cyclohexane of 0.025 is in good agreement with the value of 0.02 that is common for silica spheres prepared by the method of Stöber.

2.4.2.b DICHOISM BEYOND MEAN FIELD

Dichroism as a function of the shear rate for correlation lengths larger than 750 nm, corresponding to distances to the critical point which are beyond mean field, are plotted in Figure 2.9 (filled symbols). Contrary to its mean field behaviour, shear induced dichroism decreases on approach of the critical point. In the mean field region there is a bright streak in the scattering pattern, corresponding to the unaffected microstructure in directions perpendicular to the flow direction (see remark just below eq.(2.7) and Figure 2.2). What is observed beyond mean field is that the intensity of this bright streak is diminished when shear flow is applied, more so on closer approach of the critical point [21]. This breakdown of microstructure in directions perpendicular to the flow direction renders the structurefactor more isotropic, leading to smaller dichroism. This effect of shear flow on the microstructure is lost when the equation of motion for the total-correlation function is linearized (as discussed in section 2.2.3). Beyond the mean field region one should consider non-linear equations of motion. As far as we are aware, such non-linear equations have not been analysed yet.

2.4.3 RELAXATION OF DICHOISM AND TURBIDITY

Relaxation behaviour was studied for correlation lengths of 600 nm (mean field) and 1517 nm (beyond mean field). Each measurement was started at time $t = 0$ and then shear was applied at $t = 7.5$ s, and turned off at $t = 15$ s. Relaxation curves for dichroism and turbidity are given in Figure 2.12. Figure 2.12 a shows relaxation curves for a correlation length of 600 nm, within the mean field region. As can be seen, the shear induced dichroism relaxes within seconds, while the transmitted intensity (and hence the turbidity) relaxes over a much larger time interval. As can be

seen from Figure 2.12 b, where relaxation curves for a correlation length of 1517 nm. are plotted, beyond the mean field region, relaxation of dichroism remains fast.

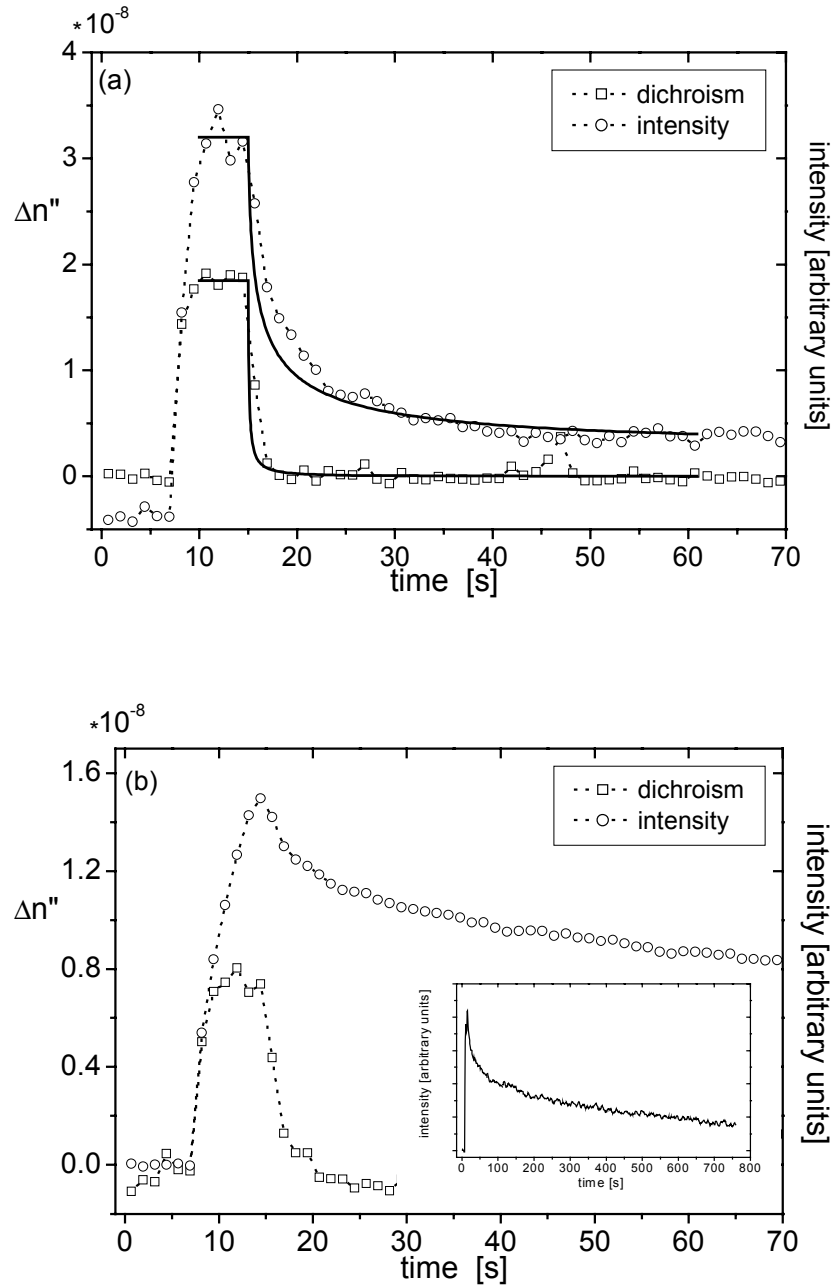


Figure 2.12: : a) Relaxation curves for dichroism and the transmitted intensity for a correlation length of 600 nm. The solid curves are theoretical mean field predictions based on eqs.(2.21) and (2.22). Shear flow is imposed at 7.5 s and is turned off at 15 s. Plot b) shows the relaxation of dichroism and transmitted intensity for the beyond mean field region ($\xi = 1517$ nm). The insert in b) shows the extremely long relaxation time for $\xi = 1280$ nm.

Relaxation times of the turbidity, however, become larger on approach of the critical point. The insert in Figure 2.12 b illustrates the extremely long relaxation time of the turbidity on very close approach of the critical point ($\xi = 1280$ nm). Hence dichroism does not show critical slowing down, contrary to the turbidity. Note that the sample in the beyond mean field region did not reach the stationary state at the time the shear rate is switched off.

These observed differences in relaxation behaviour of dichroism and turbidity are in agreement with the mean field theoretical predictions, as discussed in subsection 2.2.5 (see Figure 2.12 a). The integrands in eqs.(2.23) and (2.24) for dichroism are more sensitive to structure at larger wavevectors (because of the factor K^3) as compared to the integrand in eq.(2.21) for the turbidity (a factor K). Since the dynamics of density waves with larger wavevectors is faster than for smaller wavevectors, this results in a faster relaxation of dichroism as compared to turbidity. The slower relaxation of the turbidity for larger correlation lengths is due to the smaller value of the effective diffusion coefficient (see eq.(2.8)) for small wavevectors. The solid lines in Figure 2.12 a are theoretical relaxation curves, based on the equations in section 2.2.5. The dichroism relaxation curve is calculated from the constants derived from the scaling analysis of the stationary dichroism measurements in section 2.4.2.a, except that the constant $(2\beta\Sigma D_0)^{-1}$ is chosen as $2.3 \times 10^{-8} s^{1/2}$ instead of $2.0 \times 10^{-8} s^{1/2}$, in order to obtain agreement for the initial value of $\Delta n''$ (for a single dichroism measurement this lies within experimental errors). The theoretical intensity relaxation curve is obtained from the constants obtained in section 2.4.2.a, where the initial value of the intensity was an adjustable parameter (since we did not measure the incident intensity in this experiment) and the small experimental offset, due to optical imperfections of the shear-cell, was added to the calculated intensity. The important thing to note here is that the theoretical; curves reproduce, within experimental error, the very different experimentally observed relaxation times for dichroism and turbidity.

2.5 SUMMARY AND CONCLUSIONS

Shear induced dichroism near the gas-liquid critical point behaves completely different in the mean field region and beyond mean field : for a given shear rate, dichroism first increases on approach of the critical point in the mean field region, but then decreases in the beyond mean field region. The decreasing dichroism on approach of the critical point for the beyond mean field region is probably due to the breakdown of the structure factor in directions perpendicular to the flow direction.

This phenomenon is due to non-linear terms in the equation of motion for the structure factor. These non-linear terms can be neglected in the mean field region. So far, non-linear equations of motion of the structure factor have not been analysed. In the mean field region, where equations of motion for the total-correlation function can be linearised, theory predicts scaling of data for $\Delta n''/\sqrt{\dot{\gamma}}$ when plotted against $\dot{\gamma}\xi^4$. This is confirmed by the experiments (see Figure 2.11). Values for $\beta\Sigma/R_V^2$ and $n_p - n_f$ as found by comparing the experimentally obtained master curve and the theoretically predicted scaling function are in accordance with a theoretical estimate for $\beta\Sigma/R_V^2$ [8, 19] and independent experimental results for $n_p - n_f$ (see section 2.4.2.a). Shear rate dependent turbidity measurements close to the critical point on a similar colloidal system [20] rendered an unexpectedly high value of 3.6 for $\beta\Sigma/R_V^2$. The reason for this is not clear.

Relaxation experiments after cessation of the shear flow show that dichroism does not exhibit experimentally relevant critical slowing down: relaxation times are found of the order of a second, right up to the critical point. This is in contrast to the turbidity, the relaxation time of which is found to diverge on approach of the critical point. This different dynamical behaviour of dichroism and turbidity is in accordance with mean field theory. Formally, dichroism is more sensitive to the dynamics of density waves with larger wavevectors (due to the factor K^3 in the integrand in eqs.(2.23) and (2.24)) as compared to the turbidity (a factor K in the integrand in eq.(2.21)). Since the dynamics of density waves are faster for larger wavevectors, this explains the relatively fast relaxation of dichroism. It is surprising however, that even very close to the critical point, the dichroism relaxation dynamics remains fast.

2.6 REFERENCES :

1. D. Beysens and R. Gastaud, Phys. Rev. A, **30**, 1145 (1984).
2. D. Ronis, Phys. Rev. A, **29**, 1453 (1984).
3. A. Onuki, J. Phys.: Cond. Matter, **9**, 6119 (1997).
4. A. Onuki, K. Nakatani and K. Kawasaki, Ann. Phys, **131**, 217 (1981).
5. J.F. Scharwl and S. Hess, Phys. Rev. A, **33**, 4277 (1986).
6. N.J. Wagner and W.B. Russel, Physica A, **155**, 475 (1989).
7. Dhont, J.K.G., *An Introduction to Dynamics of Colloids*. studies in interface science, ed. D. Mobius and R. Miller. Vol. II. 1996: Elsvier. 642.
8. J.K.G. Dhont and H. Verduin, J. Chem. Phys., **101**, 6193 (1994).
9. J.K.G. Dhont and H. Verduin, Physica A, **235**, 87 (1997).
10. S. Asakura and F. Oosawa, J. Chem. Phys., **22**, 1255 (1954).
11. S. Asakura and F. Oosawa, J. Pol. Sc., **XXXIII**, 183 (1958).
12. A. Vrije, Pure Apl. Chem., **48**, 471 (1976).
13. H.N.W. Lekkerkerker, W.C.K., P.N. Pusey, A. Stroobants and P.B. Warren, Europhys. Lett., **20**, 559 (1992).
14. V.G. Puglielli and N.C. Ford, Jr., Phys. Rev. Lett., **25**, 143 (1970).
15. J.K.G. Dhont, Phys. Rev. Lett., **76**, 4469 (1996).
16. W. Stöber, A. Fink and E. Bohn, J. Colloid Int. Sci., **26**, 62 (1968).
17. Fuller, G.G., *Optical Rheometry of complex fluids*. first ed, ed. K.E. Gubbins. 1995, Cornell University: Oxford University press. 268.
18. G.G. Fuller and K.J. Mikkelsen, J. Rheol., **33**, 761 (1989).
19. M. Fixman, Advances in Chemical Physics, **6**, 175 (1964).
20. Verduin, H. and J.K.G. Dhont, Phys. Rev. E, **52**, 1811 (1995).
21. Dhont, J.K.G. and I. Bodnar, Phys. Rev. E, **58**, 4783 (1998).

Chapter 3

SHEAR-INDUCED DISPLACEMENT OF ISOTROPIC-NEMATIC SPINODALS

The shear dependent location of the isotropic-nematic spinodals in suspensions of bacteriophage fd is studied by means of time resolved birefringence experiments. The hysteresis in the birefringence on increasing and subsequently decreasing the shear-rate allows the determination of the location of points in the shear-rate versus concentration phase diagram between the isotropic-to-nematic and the nematic-to-isotropic spinodals. Experimental hysteresis curves are interpreted on the basis of an equation of motion for the orientational order parameter tensor, as derived from the N-particle Smoluchowski equation. The spinodals are found to shift to lower concentrations on increasing the shear-rate. Above a critical shear-rate, where shear forces dominate over thermodynamic forces, no spinodal instability could be detected.

3.1 INTRODUCTION

Early experimental observations of isotropic-nematic phase coexistence in systems of rod-like colloidal particles were made by Zocher [1] and Bernal [2]. In later experimental studies [3-8], other colloidal systems were found to exhibit isotropic-nematic phase coexistence as well, and in some studies [9-13] the kinetics of isotropic-to-nematic phase separation has been addressed. An exact theoretical result for the isotropic-nematic phase boundaries for very long and thin, rigid rods with excluded volume interactions has been obtained some 50 years ago by Onsager [14]. More recent theoretical developments on the isotropic-nematic phase transition can be found in refs. [15-18]. Orientational order parameter dynamics in systems of rod-like colloids with excluded volume interactions have been considered theoretically by Doi and Edwards [19] and Maeda [20]. Their approach is extended by Shimada et al. [21] and very recently by Winters et al. [22], to include inhomogeneities, in order to describe phase separation kinetics during the initial stage of spinodal demixing. Still open issues in this area are concerned with the role of attractive interactions and phase separation kinetics, especially beyond the initial stage (see v.d. Schoot [17], and Winters [22]).

Phase coexistence and phase separation kinetics in systems of lyotropic rigid rods under shear flow are less well understood. The only work on rod-like systems in this respect we are aware of is due to Olmsted [23-25]. This work is partly based on thermodynamic considerations, where driving forces are assumed to be generated by gradients in free energy. Olmsted et al. assume local equilibrium and one of the phase coexistence conditions is equality of chemical potential in both phases. Although strictly speaking a free energy and chemical potential can not be defined for a system in a non-conservative external field like the simple shear flow, this work predicts interesting features. Olmsted addresses the shear induced shift of spinodals and binodals, the existence of a log-rolling phase, where the director of the aligned rods is parallel to the vorticity direction, and the occurrence of a hydrodynamic instability commonly referred to as the shear-banding instability. As far as we know, there are no experimental results on the shear induced shift of phase coexistence boundaries or spinodals. *In the present paper we present experimental results on the shear induced shift of the isotropic-nematic spinodals for suspensions of bacteriophage fd-virus.* The experimental technique that we used is time resolved birefringence measurement,

where the hysteresis in birefringence on increasing and subsequently decreasing the shear-rate is measured.

This chapter is organised as follows. In section 3.2.2 we shall present the theoretical background that is necessary to interpret experiments. In particular, we shall define the notion of spinodals in systems under shear flow, derive an equation of motion for the orientational order parameter tensor, starting from the N-particle Smoluchowski equation for rigid rods, and use this equation of motion to calculate hysteresis curves. In the experimental section 3.3, we shall first describe the colloidal system and the birefringence equipment, and then proceed with presenting the experimental results and discussion. Section 3.4 contains a summary and conclusions.

3.2 THEORY

3.2.1 THE SUSPENSION FLOW FIELD

The flow considered here is chosen in x-direction, with its gradient in the y-direction. That is, the flow velocity is equal to $\mathbf{U} = \mathbf{\Gamma} \cdot \mathbf{r}$, where $\mathbf{\Gamma}$ is the velocity gradient tensor,

$$\mathbf{\Gamma} = \dot{\gamma} \begin{pmatrix} 0 & 1 & 0 \\ 0 & 0 & 0 \\ 0 & 0 & 0 \end{pmatrix} \quad (3.1)$$

with $\dot{\gamma}$ the shear-rate. The direction of the incident laser beam is along the gradient direction, as depicted in Figure 3.1, while the polarization state of the light is characterized by the angle α of the electric field with the z-axis.

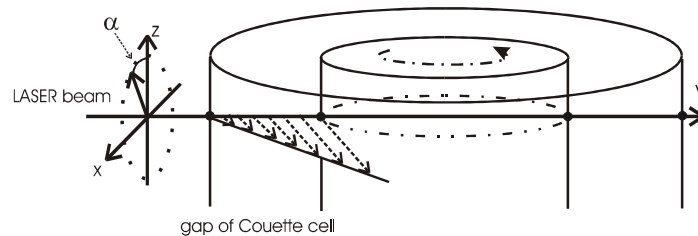


Figure 3.1: Definition of the flow geometry.

3.2.2 DEFINITION OF SPINODALS IN SYSTEMS UNDER SHEAR FLOW

A spinodal is defined as the set of control variables (like temperature, concentration and shear-rate) where the system in the homogeneous state becomes absolutely

unstable. That is, the spinodal separates the (meta-) stable region from the unstable region in the phase diagram, where demixing is initiated by order parameter fluctuations of arbitrary small amplitude. On the (meta-) stable side of the spinodal, phase separation is induced only by fluctuations with an amplitude that exceeds some minimum, finite amplitude. Without shear flow, the spinodal can be obtained from thermodynamic considerations: by definition the spinodal is the set of variables where the free energy barrier for phase separation becomes equal to zero. Such a thermodynamic approach is no longer feasible for systems in a non-conservative external field, like a simple shear flow. The spinodal must now be obtained from equations of motion for the relevant order parameter. By definition, the location of the spinodal can now be obtained by a linear stability analysis of the equation of motion. The set of control variables where the equation of motion becomes absolutely unstable defines the spinodal. This kinetic definition of the spinodal should reduce to the usual thermodynamic definition in the absence of shear flow. In case of the gas-liquid transition for attractive spherical colloids, the relevant order parameter is the density. The equation of motion for the density, as derived from the Smoluchowski equation for spheres, is indeed shown in ref. [26] to reproduce the gas-liquid spinodal as obtained from thermodynamic considerations, when shear-rate contributions to the equation of motion are neglected. For the rod-like systems under consideration here, the equation of motion for the orientational order parameter becomes unstable beyond some concentration. This equation of motion will be derived in the next subsection.

Experimentally, the location of a spinodal can in principle not be detected to within arbitrary accuracy. Close to the theoretical spinodal, on the (meta-) stable side, the amplitude of order parameter fluctuations necessary to initiate demixing is small, but non-zero. When the change in free energy on creating an order parameter variation of such small amplitude is less than about $k_b T$, demixing will occur without any time delay, as if one quenched into the unstable region of the phase diagram. There is thus a gradual change of nucleation dominated demixing to spinodal demixing. This prevents a sharp experimental determination of the location of the spinodal.

3.2.3 AN EQUATION OF MOTION FOR THE ORIENTATIONAL ORDER PARAMETER TENSOR

The reason for deriving an equation of motion for the orientational order parameter is twofold. First of all, a linear stability analysis of such an equation renders the shear-rate dependent location of the spinodals. Second, this equation of motion will be used

in subsection 3.2.6 to analyse the experimental procedure used here to detect the location of the spinodals.

The equation of motion that we will derive here from the N-particle Smoluchowski equation for rigid rods, is very similar to that obtained from the Doi-Edwards equation [19]. The assumptions involved in the derivation of the equation of motion for the orientational order parameter tensor are most clearly revealed by starting from the N-particle Smoluchowski equation. We shall therefore discuss the derivation of this equation of motion, starting from the N-particle Smoluchowski equation, in some detail below.

The central quantity is the orientational order parameter tensor, which is defined as,

$$\mathbf{S} \equiv \langle \hat{\mathbf{u}}\hat{\mathbf{u}} \rangle \quad (3.2)$$

where $\hat{\mathbf{u}}$ is the unit vector along the long axis of a uni-axial rod, the ‘‘orientation’’ of the rod, and the brackets denote ensemble averaging. The eigenvector of this tensor with the largest eigenvalue is commonly referred to as ‘‘the director’’, and points into the preferred orientation of the rods. Equations of motion for \mathbf{S} have been considered before by Hess [27], and Doi and Edwards [19]. Hess’s derivation is based on thermodynamic arguments, while Doi and Edwards start from their equation of motion for the probability density function (pdf) of the orientations of a rod. Here we will start from the N-particle Smoluchowski equation for the pdf P of the positions $(\mathbf{r}_1, \mathbf{r}_2, \dots, \mathbf{r}_N)$ and orientations $(\hat{\mathbf{u}}_1, \hat{\mathbf{u}}_2, \dots, \hat{\mathbf{u}}_N)$ of all N rods in the system under consideration. In analysing this equation of motion we will recover the equation of motion used by Doi and Edwards, which is known to reproduce the Euler-Lagrange equation that complies with Onsager’s free energy functional without shear flow [28]. The Smoluchowski equation is a continuity equation for translational and rotational motion and reads,

$$\frac{\partial P}{\partial t} = -\sum_{j=1}^N \left[\nabla_j \cdot (\mathbf{v}_j P) + \hat{\mathcal{R}}_j \cdot (\boldsymbol{\Omega}_j P) \right] \quad (3.3)$$

with \mathbf{v}_j the transitional velocity of rod j and $\boldsymbol{\Omega}_j$ it’s angular velocity, ∇_j is the gradient operator with respect to r_j , and $\hat{\mathcal{R}}_j$ is the rotation operator which is defined as,

$$\hat{\mathcal{R}}_j(\dots) = \hat{\mathbf{u}}_j \times \nabla_{\mathbf{u}_j}(\dots)$$

with $\nabla_{\mathbf{u}_j}$ the gradient operator with respect to the orientation $\hat{\mathbf{u}}_j$ of rod j .

On the Brownian time scale, where there is a force and torque balance, the translational and rotational velocities of the rods can be expressed as functions of positions and orientations. To this end, a rod is represented as a string of spherical beads, and Faxen's theorem is applied to each of the beads. Analysing the resulting relation between the bead velocities and the hydrodynamic forces on the beads for very long, thin rods (similar to ref. [29]), the following expression for the translational velocity is obtained,

$$\mathbf{v}_j = -D_t \mathbf{D}(\hat{\mathbf{u}}_j) \cdot [\beta \nabla_j \Psi + \nabla_j \ln P] + \mathbf{U}(\mathbf{r}_j) \quad (3.4)$$

with $\beta = 1/k_B T$ and,

$$D_t = \frac{k_B T \ln(L/D)}{4\pi\eta_0 L}$$

which is proportional to the orientationally averaged translational diffusion coefficient for a free, non-interacting rod, with L the length and D the diameter of the rod, and η_0 the viscosity of the solvent. Furthermore,

$$\mathbf{D}(\hat{\mathbf{u}}) \equiv \hat{\mathbf{I}} + \hat{\mathbf{u}}\hat{\mathbf{u}}$$

while Ψ in eq.(3.4) is the total potential energy and \mathbf{U} is the suspension flow velocity. The rotational velocity is found similarly and equals,

$$\boldsymbol{\Omega}_j = -D_r [\beta \hat{\mathcal{R}}_j \Psi + \hat{\mathcal{R}}_j \ln P] + \hat{\mathbf{u}}_j \times [\hat{\mathbf{u}}_j \cdot \nabla_j \mathbf{U}(\mathbf{r}_j)] \quad (3.5)$$

with,

$$D_r = \frac{3k_B T \ln(L/D)}{\pi\eta_0 L^3}$$

the rotational diffusion coefficient for a free, non-interacting rod.

In both eqs.(3.4) and (3.5) the total potential energy accounts for direct interactions between the rods. The total potential energy is now assumed to be pair-wise additive, that is,

$$\Psi(\mathbf{r}_1, \dots, \mathbf{r}_N, \hat{\mathbf{u}}_1, \dots, \hat{\mathbf{u}}_N) = \sum_{i < j} V(\mathbf{r}_i - \mathbf{r}_j, \hat{\mathbf{u}}_i, \hat{\mathbf{u}}_j)$$

where V is the interaction potential for two isolated rods: the ‘‘pair-interaction potential’’. In case of excluded volume interactions this is an exact relation. Integration of the Smulochowski equation eq.(3.3) with respect to $\mathbf{r}_1, \mathbf{r}_2, \dots, \mathbf{r}_N$ and $\hat{\mathbf{u}}_2, \dots, \hat{\mathbf{u}}_N$, after the substitution of eqs.(3.4) and (3.5), results in the equation of motion for the reduced pdf $P(\hat{\mathbf{u}}, t)$ for the orientation $\hat{\mathbf{u}}$ of a rod. This equation of motion depends on the two-particle pdf $P(\mathbf{r}, \mathbf{r}', \hat{\mathbf{u}}, \hat{\mathbf{u}}')$. In order to obtain a closed

equation of motion, let us first introduce the pair-correlation function g . For a homogeneous system the pair-correlation function is defined as,

$$\begin{aligned} P(\mathbf{r}, \mathbf{r}', \hat{\mathbf{u}}, \hat{\mathbf{u}}', t) &\equiv \int d\mathbf{r}_3 \dots \int d\mathbf{r}_N \oint d\hat{\mathbf{u}}_3 \dots \oint d\hat{\mathbf{u}}_N P(\mathbf{r}, \mathbf{r}', \mathbf{r}_3, \dots, \mathbf{r}_N, \hat{\mathbf{u}}, \hat{\mathbf{u}}', \hat{\mathbf{u}}_3, \dots, \hat{\mathbf{u}}_N, t) \\ &\equiv \frac{1}{V^2} P(\hat{\mathbf{u}}, t) P(\hat{\mathbf{u}}', t) g(\mathbf{r}, \mathbf{r}', \hat{\mathbf{u}}, \hat{\mathbf{u}}', t) \end{aligned} \quad (3.6)$$

We shall approximate the pair-correlation function as,

$$g(\mathbf{r}, \mathbf{r}', \hat{\mathbf{u}}, \hat{\mathbf{u}}', t) = \exp(-\beta V(\mathbf{r} - \mathbf{r}', \hat{\mathbf{u}}, \hat{\mathbf{u}}')) \quad (3.7)$$

This expression is correct for homogeneous systems in equilibrium, for long, thin rods with repulsive pair-interactions. Effects of shear flow on g are neglected in eq.(3.7). The effect of shear flow on the one-particle pdf $P(\hat{\mathbf{u}}, t)$ is probably much more important.

Substitution of eqs.(3.4) and (3.5) into eq.(3.3), and then performing the integration as described earlier, one finds,

$$\begin{aligned} \frac{\partial}{\partial t} P(\hat{\mathbf{u}}, t) &= D_r \hat{\mathcal{R}} \cdot (\hat{\mathcal{R}} P(\hat{\mathbf{u}}, t) - \beta P(\hat{\mathbf{u}}, t) \bar{\mathbf{T}}(\hat{\mathbf{u}}, t)) \\ &\quad - \hat{\mathcal{R}} \cdot P(\hat{\mathbf{u}}, t) \hat{\mathbf{u}} \times (\hat{\mathbf{u}} \cdot \nabla \mathbf{U}(\mathbf{r}, t)) \end{aligned} \quad (3.8)$$

where $\bar{\mathbf{T}}(\hat{\mathbf{u}}, t)$ the average torque on a rod, which is equal to,

$$\bar{\mathbf{T}}(\hat{\mathbf{u}}, t) = -\bar{\rho} \int d\mathbf{r}' \oint d\hat{\mathbf{u}}' P(\hat{\mathbf{u}}', t) g(\mathbf{r} - \mathbf{r}', \hat{\mathbf{u}}, \hat{\mathbf{u}}', t) \hat{\mathcal{R}} V(\mathbf{r} - \mathbf{r}', \hat{\mathbf{u}}, \hat{\mathbf{u}}') \quad (3.9)$$

with $\bar{\rho} = N/V$ the number density. To within the approximation eq.(3.7) for the pair-correlation function, we have, for excluded volume interactions,

$$g(\mathbf{r} - \mathbf{r}', \hat{\mathbf{u}}, \hat{\mathbf{u}}') \hat{\mathcal{R}} V(\mathbf{r} - \mathbf{r}', \hat{\mathbf{u}}, \hat{\mathbf{u}}') = \beta^{-1} \chi(\mathbf{r} - \mathbf{r}', \hat{\mathbf{u}}, \hat{\mathbf{u}}') \quad (3.10)$$

where χ is the characteristic function for core-overlap, that is, $\chi = 1$ when the cores of the rods overlap and is 0 otherwise. Since for very long, thin rods,

$$\int d\mathbf{r}' \chi(\mathbf{r} - \mathbf{r}', \hat{\mathbf{u}}, \hat{\mathbf{u}}') = 2DL^2 |\hat{\mathbf{u}} \times \hat{\mathbf{u}}'| \quad (3.11)$$

the average torque is found to be equal to,

$$\bar{\mathbf{T}}(\hat{\mathbf{u}}, t) = -2\beta^{-1} DL^2 \bar{\rho} \hat{\mathcal{R}} \oint d\hat{\mathbf{u}}' P(\hat{\mathbf{u}}', t) |\hat{\mathbf{u}} \times \hat{\mathbf{u}}'| \quad (3.12)$$

We shall expand the right hand-side of this equation to fourth order in bilinear products of the orientations $\hat{\mathbf{u}}$ and $\hat{\mathbf{u}}'$. This Ginzburg-Landau type of expansion results in a fourth order expansion of the free energy with respect to \mathbf{S} , in the case where no shear flow is applied. Such an expansion captures the essential physics. Hence, we shall approximate, $|\hat{\mathbf{u}} \times \hat{\mathbf{u}}'| \approx 1 - \frac{1}{2}(\hat{\mathbf{u}} \cdot \hat{\mathbf{u}}')^2$, which is reminiscent to the well

known Maier-Saupe approximation for the pair-interaction potential for two hard rods [30-32]. Evaluation of the average torque now results in,

$$\bar{\mathbf{T}}(\hat{\mathbf{u}}, t) = 2\beta^{-1}DL^2\bar{\rho} \hat{\mathbf{u}} \times [\mathbf{S}(t) \cdot \hat{\mathbf{u}}] \quad (3.13)$$

Multiplying both sides of eq.(3.8) by $\hat{\mathbf{u}}\hat{\mathbf{u}}$, using eqs.(3.13) and (3.9), and then integrating with respect to $\hat{\mathbf{u}}$, yields an equation of motion for the order parameter tensor \mathbf{S} . This result is only valid for the homogeneous system, where the shear-rate, the density and orientational order are independent of position,

$$\begin{aligned} \frac{\partial}{\partial t} \mathbf{S} = & -2D_r \left[3\mathbf{S} - \hat{\mathbf{I}} - 2DL^2\bar{\rho}(\mathbf{S} \cdot \mathbf{S} - \mathbf{S}^{(4)} : \mathbf{S}) \right] \\ & + \dot{\gamma} \left[\hat{\mathbf{\Gamma}} \cdot \mathbf{S} + \mathbf{S} \cdot \hat{\mathbf{\Gamma}}^T - 2\mathbf{S}^{(4)} : \hat{\mathbf{\Gamma}} \right] \end{aligned} \quad (3.14)$$

where,

$$\mathbf{S}^{(4)} = \langle \hat{\mathbf{u}}\hat{\mathbf{u}}\hat{\mathbf{u}}\hat{\mathbf{u}} \rangle$$

is a fourth order tensor. To be able to evaluate eq.(3.14), $\mathbf{S}^{(4)}$ must be expressed in terms of \mathbf{S} . Following Hinch [33], such a closure relation can be constructed by noting that the degree of alignment of the rods is a monotonically increasing function of the shear-rate. An interpolation between the known forms of $\mathbf{S}^{(4)}$ for the isotropic and the perfectly aligned states is therefore expected to be reasonably accurate. Assuming a second order polynomial in \mathbf{S} for $\mathbf{S}^{(4)}$, a calculation of the coefficients from the known forms for the isotropic and fully aligned states, and imposing trivial contraction properties, yields, for arbitrary tensors \mathbf{M} ,

$$\langle \hat{\mathbf{u}}\hat{\mathbf{u}}\hat{\mathbf{u}}\hat{\mathbf{u}} \rangle : \mathbf{M} = \frac{1}{5} \left[\mathbf{S} \cdot \mathbf{M}_s + \mathbf{M}_s \cdot \mathbf{S} - \mathbf{S} \cdot \mathbf{S} \cdot \mathbf{M}_s - \mathbf{M}_s \cdot \mathbf{S} \cdot \mathbf{S} + 2\mathbf{S} \cdot \mathbf{M}_s \cdot \mathbf{S} + 3\mathbf{SS} : \mathbf{M}_s \right] \quad (3.15)$$

with,

$$\mathbf{M}_s = \frac{1}{2} \left[\mathbf{M} + \mathbf{M}^T \right]$$

the symmetric part of \mathbf{M} . Using this closure relation in eq.(3.14), we finally find,

$$\begin{aligned} \frac{\partial}{\partial t} \mathbf{S} = & -\dot{\gamma} \left(\frac{2}{5} \left[\mathbf{S} \cdot \mathbf{M}_s + \mathbf{M}_s \cdot \mathbf{S} - \mathbf{S} \cdot \mathbf{S} \cdot \mathbf{M}_s - \mathbf{M}_s \cdot \mathbf{S} \cdot \mathbf{S} + 2\mathbf{S} \cdot \mathbf{M}_s \cdot \mathbf{S} + 3\mathbf{SS} : \mathbf{M}_s \right] \right. \\ & \left. - \hat{\mathbf{\Gamma}} \cdot \mathbf{S} - \mathbf{S} \cdot \hat{\mathbf{\Gamma}}^T \right) - D_r \left[6\mathbf{S} - 2\hat{\mathbf{I}} - \frac{12}{5}DL^2\bar{\rho}(\mathbf{S} \cdot \mathbf{S} - \mathbf{SS} : \mathbf{S}) \right] \end{aligned} \quad (3.16)$$

This is the equation of motion that is at the basis of our interpretation of experimental data and the calculation of the phase diagram as far as the spinodals are concerned.

As can be seen from the above derivation, the Doi-Edwards equation is obtained when assuming that the pair-correlation function has the form as given in eq.(7), that is, when higher order correlations are neglected. For very long, thin rods this is

probably a good approximation. Furthermore the translational and rotational diffusion coefficients relate to diffusion of a single, non-interacting rod, and are therefore independent of concentration. The concentration dependence of diffusion coefficients can in principle be calculated from the Smoluchowski equation, similar to calculations for spherical colloids [see for example ref. [29]].

3.2.4 THE SHEAR-RATE DEPENDENT SPINODALS

Let us first define the effective rotational diffusion coefficient D_r^{eff} as follows. Let \mathbf{S}_0 denote a stationary solution of the equation of motion eq.(3.16). Now write $\mathbf{S}(t) = \mathbf{S}_0 + \delta\mathbf{S}(t)$, and linearize the equation of motion eq.(3.16) with respect to $\delta\mathbf{S}(t)$. The linearized equation of motion will be of the form,

$$\frac{\partial \delta\mathbf{S}(t)}{\partial t} = -cD_r^{eff} \delta\mathbf{S}(t) \quad (3.17)$$

with c a numerical constant that is chosen such that for infinite dilution, in the absence of shear flow, the effective diffusion coefficient D_r^{eff} becomes equal to the single particle diffusion coefficient. The effective rotational diffusion coefficient depends on concentration and on \mathbf{S}_0 . When D_r^{eff} is positive, the stationary solution \mathbf{S}_0 is stable, when D_r^{eff} is negative it is unstable. By definition (see subsection 3.2.2) the density and the state \mathbf{S}_0 are on the spinodal when D_r^{eff} is zero. The rotational dynamics are thus extremely slow close to the spinodal (this is analogous to critical slowing of translational diffusion in case of a gas-liquid transition). The spinodal concentration where the isotropic state without shear flow becomes absolutely unstable can be found by linearization around $\mathbf{S}_0 = \frac{1}{3} \hat{\mathbf{I}}$. Hence we write,

$$\mathbf{S}(t) = \frac{1}{3} \hat{\mathbf{I}} + \delta\mathbf{S}(t) \quad (3.18)$$

and linearize eq.(3.16) with respect to $\delta\mathbf{S}(t)$. The solution of the resulting linear equation of motion is,

$$\delta\mathbf{S}(t) = \delta\mathbf{S}(t=0) \exp\{-6D_r^{eff}t\} \quad (3.19)$$

where the effective rotational diffusion coefficient is given by,

$$D_r^{eff} = D_r \left(1 - \frac{2}{15} DL^2 \bar{\rho}\right) \quad (3.20)$$

For concentrations where $\frac{2}{15} DL^2 \bar{\rho} > 1$, the effective rotational diffusion coefficient is negative, so that eq.(3.19) predicts an exponential increase of $\delta\mathbf{S}(t)$ with time. The spinodal concentration for the isotropic-to-nematic transition, in terms of the volume fraction ϕ of rods, is thus found to be equal to $\frac{L}{D} \phi = 5.89$. This number should be

compared to its exact value, 4, for very long, thin rods as found by Onsager [14]. The discrepancy between our result and the exact value is primarily due to the Ginzburg-Landau type of expansion, and to a lesser extent, to the closure relation.

In the case where shear flow is applied it is convenient to introduce the dimensionless rotational Peclet number,

$$Pe_r^0 = \dot{\gamma} / D_r \quad (3.21)$$

and the dimensionless time,

$$\tau = D_r t \quad (3.22)$$

The rotational Peclet number measures the effect of the shear flow on orientational microstructure in the case where the effective diffusion coefficient is not very different from the bare diffusion coefficient D_r . The stationary state under shear flow around which one should linearize the equation of motion eq.(3.16) is not known analytically, but must be found numerically. Bifurcation diagrams, where the largest eigenvalue λ of the order parameter tensor \mathbf{S} for stable states is plotted versus $\frac{L}{D}\phi$, are collected in Figure 3.2 for various shear-rates.

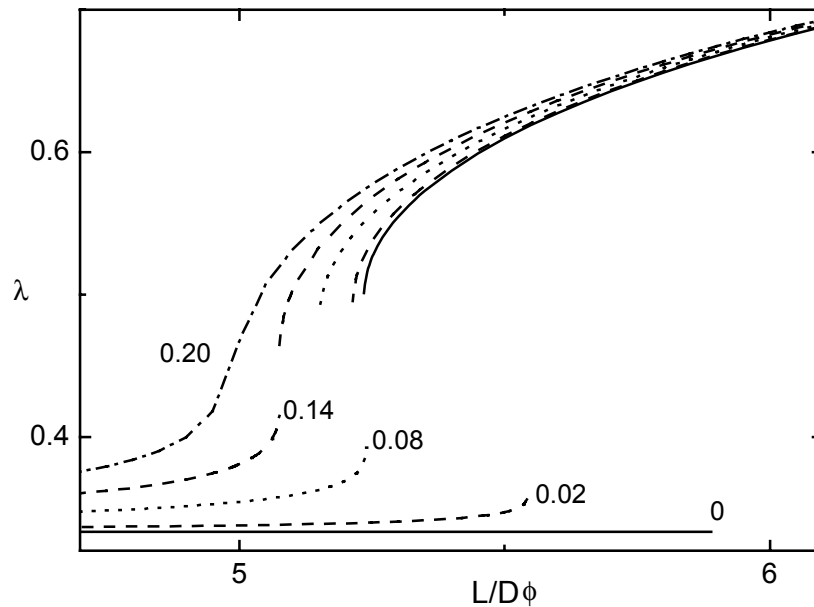


Figure 3.2: The largest eigenvalue of \mathbf{S} versus concentration. The lines represent stable solutions of the equation of motion (eq.(3.16)), for various bare Peclet numbers as indicated in the figure.

Diagrams of this sort are extensively discussed in refs. [34, 35]. The curves in the diagram are attractors for the equation of motion eq.(3.16) for a given Peclet number Pe_r^0 . The spinodal points are the points where the curves terminate: here the attractor becomes a repeller. As can be seen, for small enough shear-rates there is a concentration range where there are two stable solutions of eq.(3.16): a so-called paranematic state (the isotropic state which is slightly shear-aligned) and a nematic state. These concentrations are within the two-phase region. Above a certain critical shear-rate, corresponding to a Peclet number equal to $Pe_{r,c}^0 \approx 0.15$, the paranematic and the nematic branches merge into one single curve. For these large shear-rates, thermodynamic forces are too small in comparison to shear forces to be able to induce a discontinuous phase transition. The non-equilibrium phase diagram, as far as the spinodals are concerned, is given in Figure 3.3.

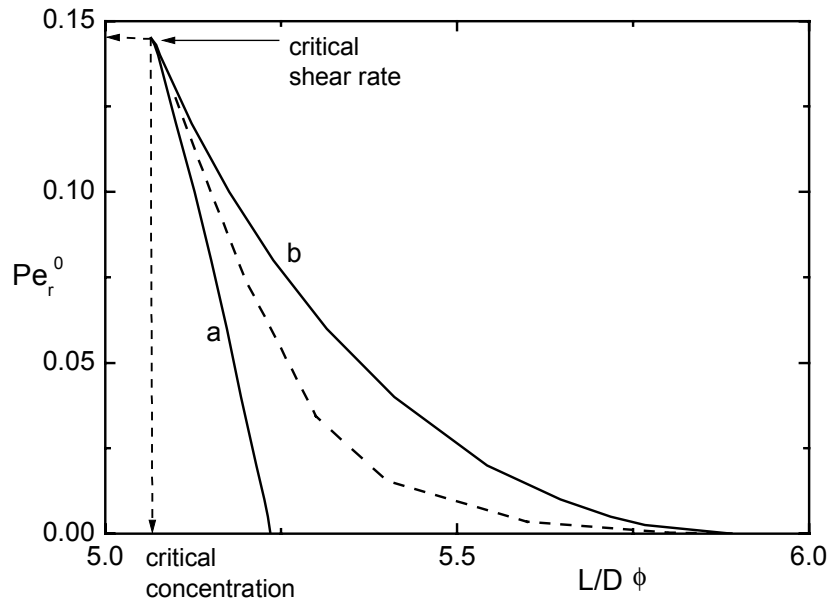


Figure 3.3: Non-equilibrium spinodals. The lower solid line (a) is the spinodal where the nematic phase becomes unstable on lowering the concentration (the nematic-to-paranematic spinodal), while the upper solid line (b) is the spinodal where the paranematic phase becomes unstable on increasing the concentration (the paranematic-to-nematic spinodal). The dotted line is the predicted experimental curve as obtained from birefringence hysteresis experiments, calculated from the equation of motion eq.(3.16) (see subsection 3.2.6).

3.2.5 THE RELATION BETWEEN BIREFRINGENCE AND THE ORIENTATIONAL ORDER PARAMETER TENSOR

Before describing the experimental method to obtain the shear-rate dependent spinodals, we shall have to establish the relation between birefringence and the orientational order parameter tensor. Let ε_{\parallel} and ε_{\perp} denote the dielectric constants for polarisation directions of the light parallel and perpendicular to the rod's long axis, respectively. These values are assumed to be constant within the core of the rod. The difference between ε_{\parallel} and ε_{\perp} comprises both intrinsic anisotropy of the rod material as well as 'form contributions' due to intra-particle multiple scattering.

By decomposing an incident electric field into a component parallel to the unit vector $\hat{\mathbf{u}}$ that specifies the orientation of the long axis of a rod and a component perpendicular to it, the dielectric constant $\boldsymbol{\varepsilon}_{rod}$ of the rod is found to be equal to,

$$\begin{aligned}\boldsymbol{\varepsilon}_{rod} &= \varepsilon_{\parallel} \hat{\mathbf{u}} \hat{\mathbf{u}} + \varepsilon_{\perp} \left[\hat{\mathbf{I}} - \hat{\mathbf{u}} \hat{\mathbf{u}} \right] \\ &= \bar{\varepsilon} \hat{\mathbf{I}} + \Delta\varepsilon \left[\hat{\mathbf{u}} \hat{\mathbf{u}} - \frac{1}{3} \hat{\mathbf{I}} \right]\end{aligned}\quad (3.23)$$

with,

$$\bar{\varepsilon} = \frac{1}{3}(\varepsilon_{\parallel} + 2\varepsilon_{\perp}) \quad , \quad \Delta\varepsilon = \varepsilon_{\parallel} - \varepsilon_{\perp}$$

The dielectric constant is now a tensorial quantity. The dielectric constant of the suspension is a linear combination of the dielectric constants of the solvent and the rod material. This is a very good approximation, certainly at the very low volume fractions of interest for the long and thin rods under consideration. The apparent dielectric constant of the suspension $\boldsymbol{\varepsilon}$, relative to that of the solvent, is thus equal to (with ε_f the dielectric constant of the solvent and φ the volume fraction of rods),

$$\begin{aligned}\boldsymbol{\varepsilon} &= \varphi \boldsymbol{\varepsilon}_{rod} + (1 - \varphi) \varepsilon_f \hat{\mathbf{I}} \\ &= \left[\varphi \bar{\varepsilon} + (1 - \varphi) \varepsilon_f \right] \hat{\mathbf{I}} + \varphi \Delta\varepsilon \left[\hat{\mathbf{u}} \hat{\mathbf{u}} - \frac{1}{3} \hat{\mathbf{I}} \right] \\ &\equiv \varepsilon_{iso} \hat{\mathbf{I}} + \varphi \Delta\varepsilon \hat{\mathbf{u}} \hat{\mathbf{u}},\end{aligned}\quad (3.24)$$

with ε_{iso} the isotropic part of the dielectric tensor, which is equal to,

$$\begin{aligned}\varepsilon_{iso} &= \varphi \bar{\varepsilon} + (1 - \varphi) \varepsilon_f - \frac{1}{3} \varphi \Delta\varepsilon \\ &= \varphi \varepsilon_{\perp} + (1 - \varphi) \varepsilon_f\end{aligned}$$

We assumed, in eq.(3.24), that all rods are identical in optical properties. The apparent dielectric constant $\varepsilon(\hat{\mathbf{n}})$ for a given polarisation direction $\hat{\mathbf{n}}$ of the light is equal to $\hat{\mathbf{n}} \cdot \boldsymbol{\varepsilon} \cdot \hat{\mathbf{n}}$. The corresponding macroscopic refractive index is equal to

$n_m(\hat{\mathbf{n}}) \sim \langle \sqrt{\mathcal{E}(\hat{\mathbf{n}})} \rangle$, where the brackets $\langle \dots \rangle$ denote ensemble averaging with respect to orientation. To leading order in $\Delta\mathcal{E} / \mathcal{E}_{iso}$ we thus find,

$$n_m(\hat{\mathbf{n}}) = n_{iso} \left[1 + \frac{1}{2} \varphi \frac{\Delta\mathcal{E}}{\mathcal{E}_{iso}} \hat{\mathbf{n}} \cdot \mathbf{S} \cdot \hat{\mathbf{n}} \right] \quad (3.25)$$

where $n_{iso} \sim \sqrt{\mathcal{E}_{iso}}$ is the refractive index corresponding to the dielectric constant \mathcal{E}_{iso} . The assumption here is that the magnetic susceptibility of the fluid and the rods are both equal to that of vacuum.

The birefringence $\Delta n'$ is defined as the maximum difference in the refractive index $n_m(\hat{\mathbf{n}})$ on varying $\hat{\mathbf{n}}$ within the plane perpendicular to the propagation direction of the light beam. In our experiments, the light beam propagates along the gradient direction (the y-direction, see Figure 3.1). Since for the geometry used here we have $\hat{\mathbf{n}} = (\mu, 0, \sqrt{1-\mu^2})$, with $0 \leq \mu \leq 1$, it is found that $\hat{\mathbf{n}} \cdot \mathbf{S} \cdot \hat{\mathbf{n}} = \mu^2 (S_{11} - S_{33}) + S_{33}$ (note that $S_{13} = 0$, due to symmetry with respect to the xy-plane). Hence the maximum and minimum values of the refractive index are taken by $\mu = 0$ and $\mu = 1$, that is, for $\hat{\mathbf{n}}$ along the x- and z-direction, respectively. We thus find that,

$$\Delta n' \sim c |S_{33} - S_{11}| \quad (3.26)$$

with S_{ij} the ij^{th} component \mathbf{S} and c the concentration. This is a special case of the formula given by Fuller [[36], page 113], with $S_{13} = 0$.

3.2.6 THE EXPERIMENTAL PROCEDURE

The intuitive idea behind the procedure used to obtain the shear-rate dependent spinodals is the following. Consider a homogeneous system of rod-like particles with a concentration below the nematic-to-isotropic spinodal concentration $\frac{L}{D}\phi = 5.24$, and above the critical concentration (see Figure 3.3).

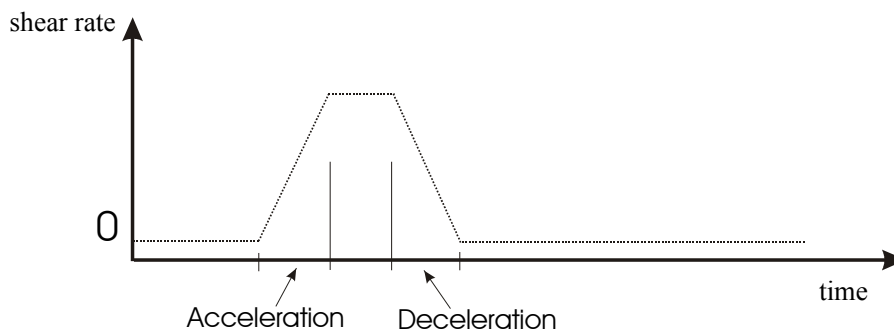


Figure 3.4: A shear-rate sweep. The shear-rate is increased linearly in time, after which the shear-rate is kept constant for 10 seconds and then decreased linearly in time to 0 within the same time span.

Suppose the system is subjected to a “shear-rate sweep” as depicted in Figure I.4 : the shear-rate is increased with time up to some value, which is then maintained for some time, after which the shear-rate is decreased to zero. On increasing the shear-rate, the concentration where the paranematic phase becomes unstable decreases, as can be seen from the bifurcation diagram Figure 3.2. At a certain shear-rate ($\dot{\gamma}_1$, say), the paranematic-to-nematic spinodal concentration will be lower than the actual concentration. The system will then, initially very slowly, evolve towards the stable nematic state. On decreasing the shear-rate after some time, the nematic state will become unstable again at a certain shear-rate ($\dot{\gamma}_2$, say). The system will then return to the paranematic state. Since $\dot{\gamma}_1 > \dot{\gamma}_2$, as can be seen from the bifurcation diagrams in Figure 3.2, there will be a hysteresis in the measured birefringence during such a shear-rate sweep. The shear-rate where the maximum hysteresis in birefringence occurs will be in between the two shear-rates $\dot{\gamma}_1$ and $\dot{\gamma}_2$ where the paranematic and nematic phase become unstable, respectively. On variation of the concentration, this procedure provides a line in the non-equilibrium phase diagram that is in between the two spinodals. Since rotational dynamics close to the spinodals are very slow, the form of the hysteresis curve will probably depend on the shear sweep rate, that is, the rate of change of the shear-rate. The effect of the very slow dynamics near the

spinodal points can be eliminated by extrapolating hysteresis curves to a sweep rate equal to zero. For concentrations above the nematic-to-isotropic spinodal concentration $\frac{L}{D}\phi = 5.24$, the system will tend towards the stable nematic state above a certain shear-rate, and will not return to the isotropic branch again on subsequent decrease of the shear-rate. There may be an exception when the system is not allowed to actually attain the stable nematic state before decreasing the shear-rate again, that is, when the state of the system remains in the basin of attraction of the paranematic branch during the entire experiment. These intuitive ideas will be quantified below on the basis of the equation of motion eq.(3.16).

There are two assumptions made in the above reasoning. First of all it is assumed that phase separation under shear does not occur during a shear-rate sweep. For the fd-system this was tested and no phase separation under shear flow was observed over a period of 2 days, while the birefringence experiments take about 5 minutes. Secondly, it is assumed that the orientational order parameter is independent of position, that is, the possible existence of domains with different directors is ignored. In the absence of shear flow such domains will certainly exist, while in the presence of strong shear flow this is probably a reasonable assumption.

The shear-rate sweep that we employed in our experiments is as follows. The shear-rate is increased linearly in time during a certain time interval up to a certain final shear-rate. This time interval and the final shear-rate determine the shear sweep rate. The final shear-rate is maintained for 10 seconds, after which the shear-rate is decreased again to 0 within the same time span (see Figure 3.4).

To relate the shear-rate with the bare Peclet number (see eq.(3.21)) and time with the dimensionless time (see eq.(3.22)), we used the bare rotational diffusion coefficient of 20.9 s^{-1} as reported in ref. [37]. Hysteresis curves can be obtained from eq.(3.16), where the shear-rate is now a prescribed function of time. Figure 3.5 shows plots of the hysteresis in birefringence, as obtained from eq(3.16), as a function of the actual bare Peclet number Pe_r^0 during a shear-rate sweep.

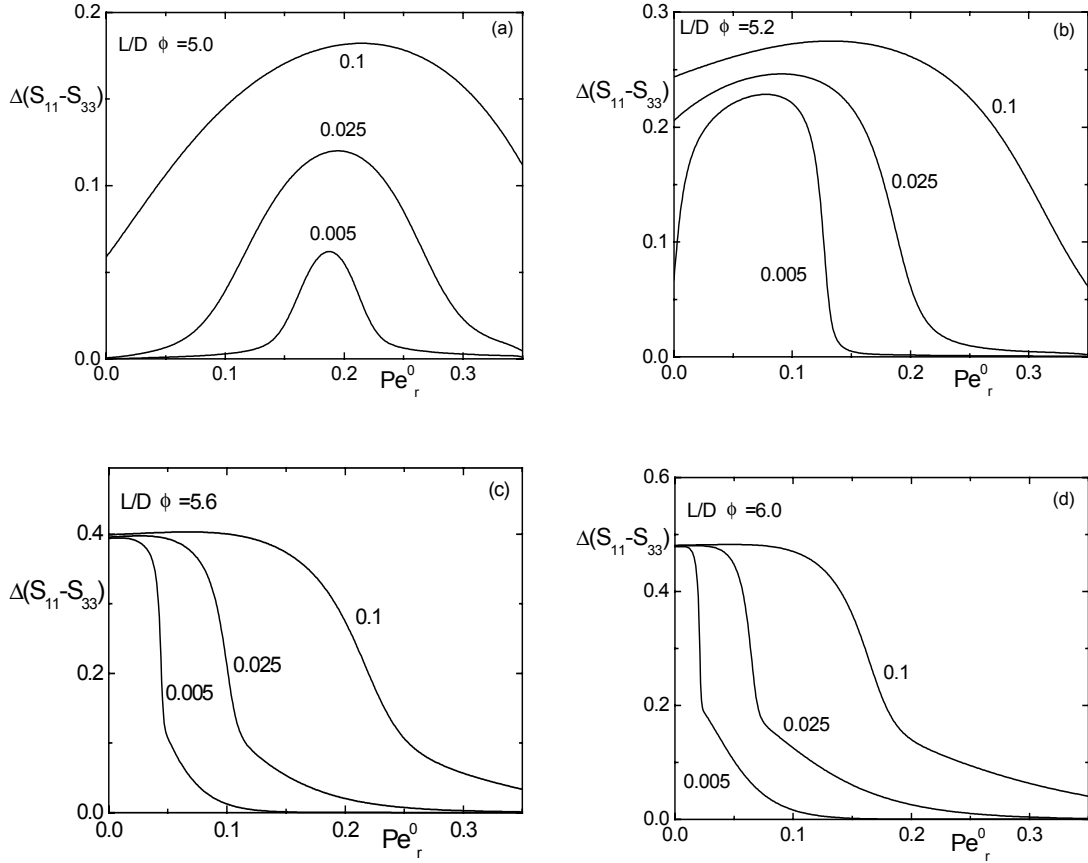


Figure 3.5: Birefringence hysteresis curves (as calculated from eq.(3.16)) for concentrations in the four different concentration regimes as defined in the main text. Plotted is the birefringence hysteresis $\Delta(S_{11} - S_{33})$ (see eq.(3.26)) versus the actual shear-rate during a shear-rate sweep, for different shear sweep rates. The shear sweep rates are indicated in the figures, and are defined here as $1/\tau_{end}$, with τ_{end} the dimensionless time interval during which the maximum shear-rate is achieved in the acceleration period of the sweep (see Figure 3.4).

Four different concentration regimes may be distinguished: concentrations below the critical concentration ($\frac{L}{D}\phi < 5.07$), concentrations in between the critical

concentration and the nematic-to-isotropic spinodal ($5.07 < \frac{L}{D}\phi < 5.24$), in between the nematic-to-isotropic spinodal and the isotropic-to-nematic spinodal ($5.24 < \frac{L}{D}\phi < 5.89$), and larger concentrations ($\frac{L}{D}\phi > 5.89$). We shall refer to these concentration regimes as the regimes I, II, III and IV, respectively. Figure 3.5 a-d relate to these concentration regimes. As explained above, a clear maximum in the hysteresis curve is expected in regime II, and is indeed found in Figure 3.5 b, since during a sweep, first the paranematic state becomes unstable on increasing the shear-rate and then the nematic state becomes unstable on decreasing the shear-rate. The maximum becomes much less pronounced in regime III (see Figure 3.5 c), since then the system attains the nematic state on increasing the shear-rate and remains in that state when the shear-rate is decreased, in accordance with our intuitive reasoning above.

Below the critical concentration, in regime I, the magnitude of the hysteresis goes to zero as the sweep rate is diminished, as can be seen in Figure 3.5 a. For a finite sweep rate there is a finite hysteresis because of the slow rotational dynamics close to the spinodals. At very small sweep rates, the upward and downward measured birefringence curve will overlap, so that the birefringence hysteresis will disappear. Note, however, that the extrapolated shear-rate where the maximum hysteresis occurs still extrapolates to a finite value, which is indicative for the location of the critical shear-rate. For lower concentrations, further away from the spinodals, where rotational dynamics is relatively fast for all shear-rates, the magnitude of the hysteresis rapidly decreases to a value that is probably too small to be measured. For concentrations above the isotropic-to-nematic concentration, regime IV, the amplitude of the hysteresis remains large. However, its maximum value extrapolates to a zero shear-rate, as can be seen in Figure 3.5 d. This is due to the fact that one starts with a paranematic state, while after the sweep, the system remains in the nematic state, similar to what happens in regime III.

The Peclet number at which the hysteresis maximum is observed is plotted as a function of the sweep rate in Figure 3.6 for various concentrations. The values of this Peclet number, extrapolated to zero shear-rate, are plotted in Figure 3.3 (the dashed line). As can be seen, this line lies in between the two spinodals, and is therefore an indication of how the location of the spinodal changes with shear-rate. Note that the critical shear-rate coincides with the shear-rate obtained from the above described experimental method.

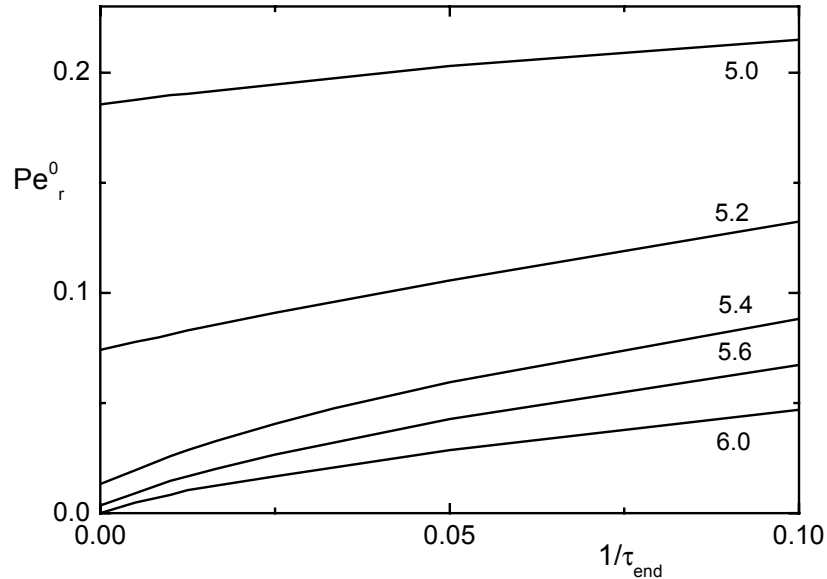


Figure 3.6: The bare Peclet number at which the maximum hysteresis is found as a function of the sweep rate, with τ_{end} the dimensionless time during which the final shear-rate is reached. The numbers in the figure refer to the various concentrations in terms of $\frac{L}{D}\phi$.

On increasing the shear-rate during a sweep, one might expect a sudden increase in the birefringence once the paranematic-to-nematic spinodal point is crossed, and a subsequent sudden decrease on lowering the shear-rate when crossing the nematic-to-paranematic spinodal again. It turns out that the dynamics close to the spinodal points are so slow, that an unambiguous identification of the shear-rate where the expected sudden increase or decrease occurs can not be determined accurately enough to really distinguish these from the shear-rate where the maximum in the hysteresis curve occurs.

What is neglected in the above analysis is the existence of distinct nematic domains, which might be important for lower shear-rates. The order parameter tensor \mathbf{S} is assumed to be the same everywhere in the system. It is unclear what the influence of the formation of inhomogenities is on the measured birefringence.

3.3 EXPERIMENTAL METHODS AND RESULTS

3.3.1 THE COLLOIDAL SYSTEM

The system used in this study consists of bacteriophage fd. These bio-polymers have a contour length of $L = 880$ nm and a diameter $D = 6.6$ nm, as obtained with electron microscopy. The persistence length of these molecules is $P = 2000$ nm, which is about twice the contour length [37]. Fd-virus is therefore somewhat flexible. The solvent is a 10 mM Tris(hydroxymethyl)-aminomethane buffer (pH = 8.15) with 25 mM NaCl added. The pH was adjusted by adding a dilute solution of hydrochloric acid (HCl) to the fd-solution.

Fd-virus molecules are charged, resulting in an effective diameter that is larger than the above mentioned thickness of 6.6 nm. From Onsager's expression for the effective diameter of a charged rod [14] we obtain a diameter of 14.8 nm at an ionic strength of 30 mM. The effective aspect ratio is thus equal to $\frac{L}{D} = 60$.

Experimentally, the two binodal concentrations without shear flow are found to be equal to 13.0 mg/ml and 14.5 mg/ml, respectively. These corresponds to values of $\frac{L}{D}\phi$ of 4.5 and 4.8, respectively (using a molar mass of 1.64×10^7 gram [37]). These numbers are higher than the respective predicted values of 3.3 and 4.2 by Onsager [14]. This discrepancy is due to the slight flexibility of fd-virus [38, 39].

3.3.2 EXPERIMENTAL SET-UP

The home-built birefringence set-up is based on the design by Fuller and Mikkelsen [40] (see Chapter 1 for more details). The rotating half-wave plate is mounted on a dentist drill, which can achieve a rotational speed of about 4 kHz. The shear cell is a home-built optical couette cell with a gapwidth of 2.47 mm, which is placed in a thermostating, optical matching bath. The largest shear-rate that is applied is 7 s^{-1} . The acceleration and deceleration times during a shear-rate sweep varied from 0.5 s to 1.0 s (see Figure 3.4). The direction of the laser beam relative to the shear geometry is depicted in Figure 3.1.

3.3.3

SHEAR ALIGNMENT OF FD-VIRUS

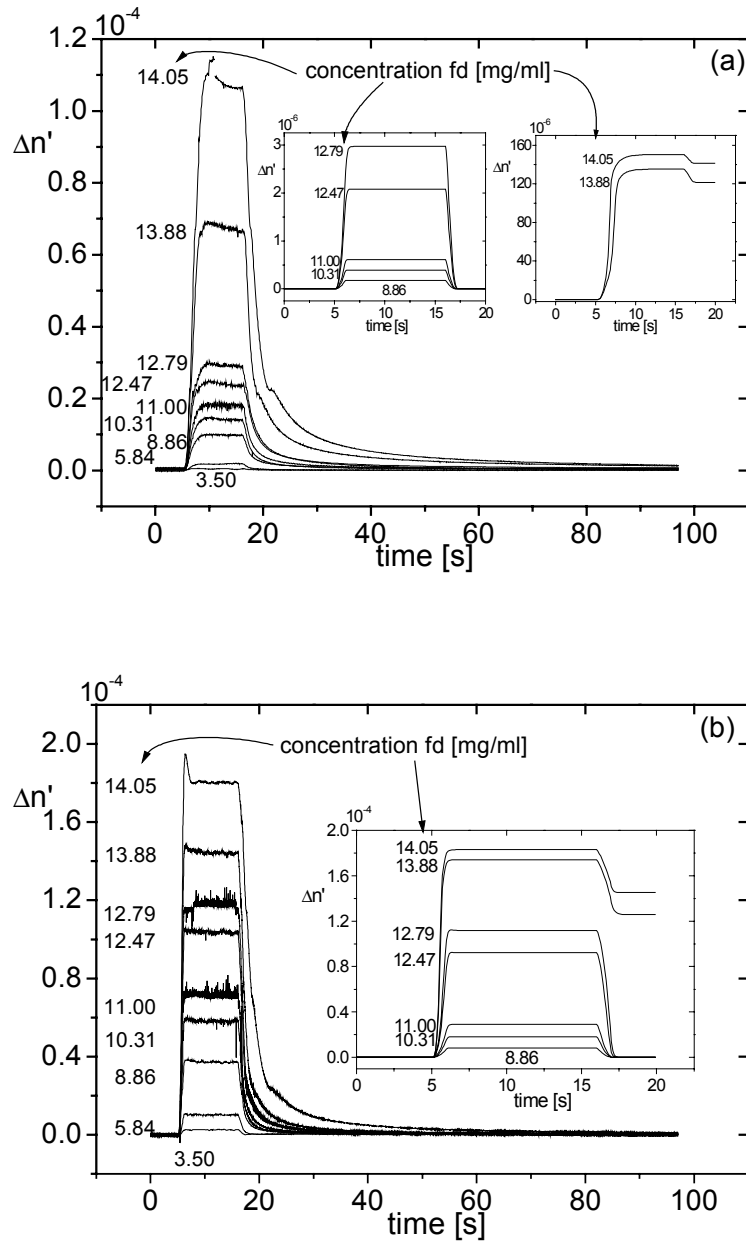


Figure 3.7: Birefringence as a function of time, where the shear-rate is linearly increased between 5 and 6 seconds, and decreased to 0 again between 16 and 17 seconds after the start of the measurement. In the time interval 6 to 16 seconds, the shear-rate is kept constant. Figure (a) is for a final shear-rate of 1 s^{-1} and (b) for 7 s^{-1} . The numbers in the figures refer to concentrations in mg/ml. The inserts in both plots are numerical results as obtained from the equation of motion eq.(3.16). The proportionality constant in eq.(3.26) is determined from the stationary experimental birefringence level for the highest concentration.

Before discussing the shear induced shift of spinodals as obtained by the above described hysteresis measurements, flow alignment experiments will be presented in the following subsection. As will be seen, there is qualitative agreement between experiment and theory, which validates the use of eq.(3.16) for the interpretation of the experimental results to obtain the shear induced shift of spinodals. Due to the Ginzburg-Landau type of expansion that was employed to derive the equation of motion eq.(3.16), and the neglect of defects, there is only qualitative agreement.

Flow alignment experiments are performed on suspensions of fd-virus for shear-rates varying from 1 and 7 s⁻¹, and concentrations varying from 3.5 mg/ml (the overlap concentration is 0.076 mg/ml), up to 14.05 mg/ml, which is close to the binodal nematic concentration. Figure 3.7 shows typical birefringence curves, where the shear-rate is linearly increased from 0 to it's final value within the time interval 5 to 6 seconds, and linearly decreased again to 0 in the time interval 16 to 17 seconds.

As expected, birefringence increases with increasing shear-rate and increasing concentration. In Figure 3.7, numerical results obtained from eq.(3.16) are plotted in the inserts. The proportionality constant in eq.(3.26) is chosen so as to match the birefringence level for the highest concentration. The proportionality constant that appears on the right hand-side of eq.(3.26) is found to be equal to 0.33×10^{-4} , when the concentration c is expressed in mg/ml. Mapping of the concentration in mg/ml onto $\frac{L}{D}\varphi$ can be done by relating the spinodal concentrations found from eq.(3.16) and the experimentally found binodal concentrations with Onsager's exact results. Since the coexistence region for fd-virus suspensions is much narrower than predicted by Onsager, there is no unambiguous choice for the proportionality constant between values of $\frac{L}{D}\varphi$ and concentrations in units of mg/ml. We chose a value of 0.38 ml/mg for the proportionality constant so as to have an optimum match between the experimental shear alignment experiments and the theoretical prediction based on eq.(3.16). For the calculation of the bare rotational Peclet number and the dimensionless time we used a bare rotational diffusion coefficient of 11 s⁻¹. This value of the rotational diffusion coefficient is found by comparing the critical shear-rates as obtained from eq.(3.16) (see Figure 3.12). The difference with the value of 20.9 s⁻¹ that was found in ref. [37] is probably due to the approximate nature of our theory and differences in contributions from electrolyte friction [41]. As can be seen, the experimental birefringence curves are in qualitative agreement with theory, except that for the highest concentrations theory predicts no decay of the

birefringence to 0. For these higher concentrations the system remains in the stable nematic state after cessation of the shear flow. The experimentally observed relaxation of birefringence is probably due to the formation of domains with different directors. The formation of such inhomogeneities has been neglected in our theory. No more than qualitative agreement can be expected, due to the approximate nature of the Ginzburg-Landau type of expansion that was used.

Note the overshoot in birefringence in Figure 3.7 a and b that occurs only for concentrations which are close to the nematic binodal concentration. This effect is more pronounced for larger shear-rates. It is unclear what the precise microscopic origin of the overshoot is. As can be seen from in Figure 3.7, this overshoot is not predicted by theory.

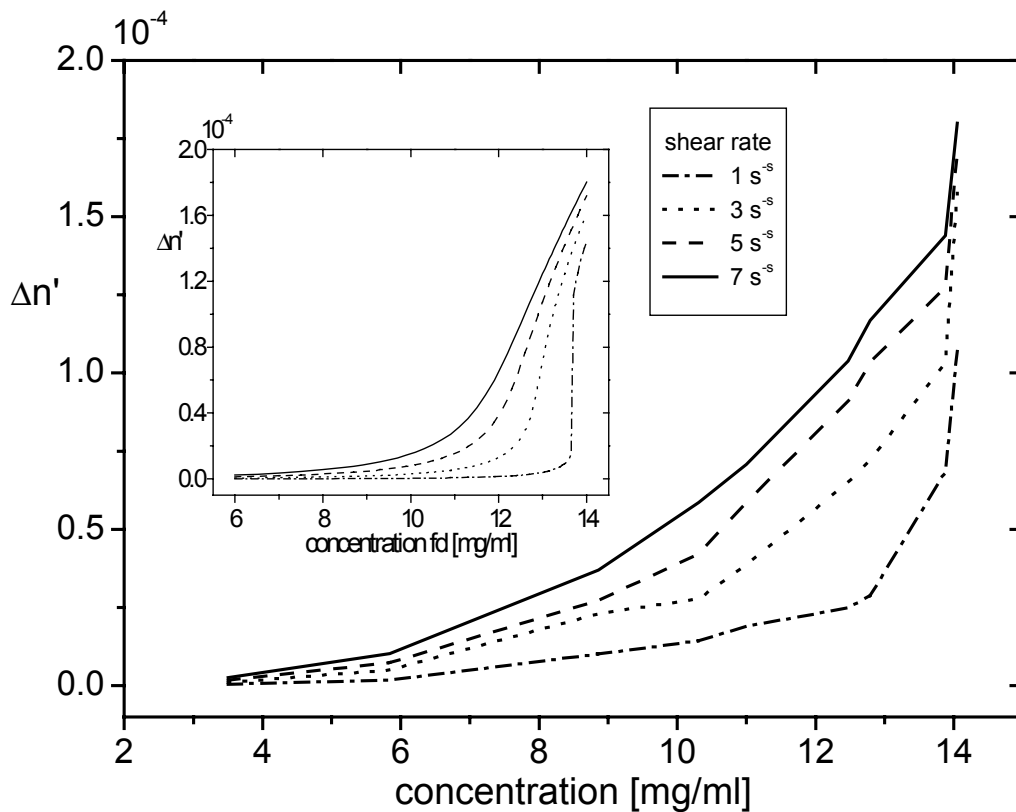


Figure 3.8: Birefringence as a function of concentration for four shear-rates, which are indicated in the figure. The insert shows the theoretical prediction according to eq.(3.16).

The concentration dependence of the stationary value of the birefringence for four different shear-rates is shown in Figure 3.8. A strong non-linear increase of the birefringence in the neighbourhood of the binodal concentration (14.5 mg/ml) is

found. For these larger concentrations, thermodynamic forces assist the shear forces to align the rods. Note the almost linear increase of birefringence with concentration for the lowest shear-rate of 1 s^{-1} , up to about 13.00 mg/ml , beyond which thermodynamic forces render a rapid increase.

The insert in Figure 3.8 is the theoretical prediction from eq.(3.16) for the same shear-rates as in the experiments. Theory underestimates the birefringence at somewhat lower concentrations. The critical shear-rate for the fd-virus suspension is 1.6 s^{-1} (see the subsequent subsection). Only the smallest shear-rate in Figure 3.8 is below this critical shear-rate. For larger shear-rates the birefringence is therefore expected to change continuously as a function of concentration. For the smallest shear-rate, the theoretically found concentration dependence exhibits a discontinuity where the paranematic state becomes unstable, and the systems jumps to the nematic state. The resolution in concentration for the data points in Figure 3.8 is too crude to really see this discontinuity.

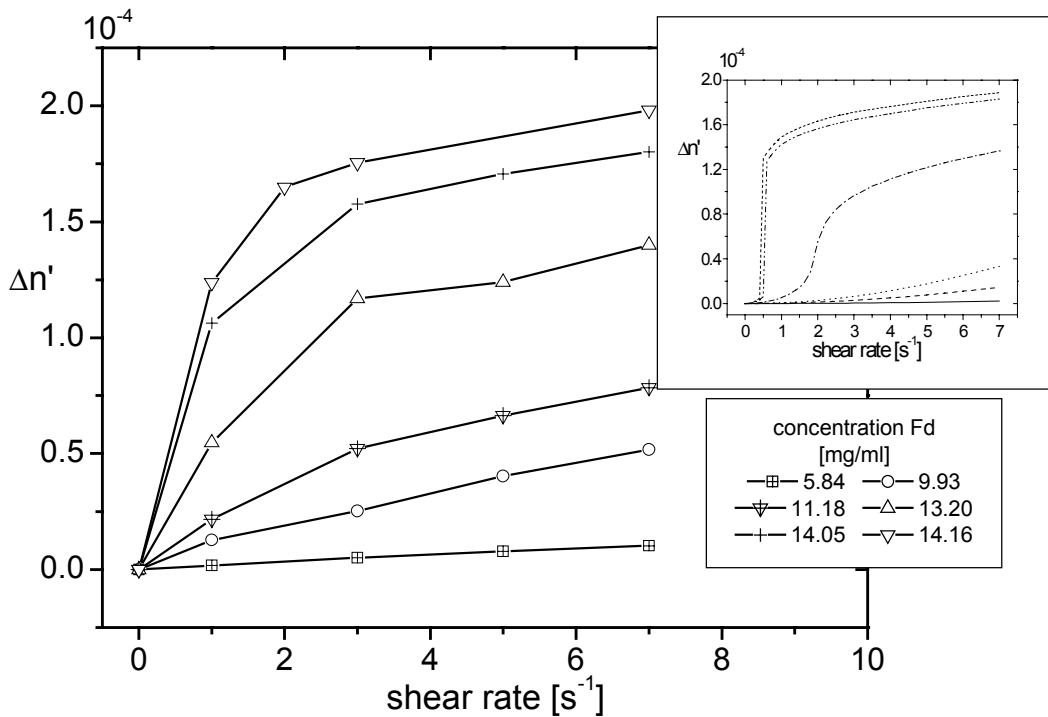


Figure 3.9: Birefringence as a function of shear-rate for various concentrations, as indicated in the figure. The insert shows theoretical results as obtained from eq.(3.16).

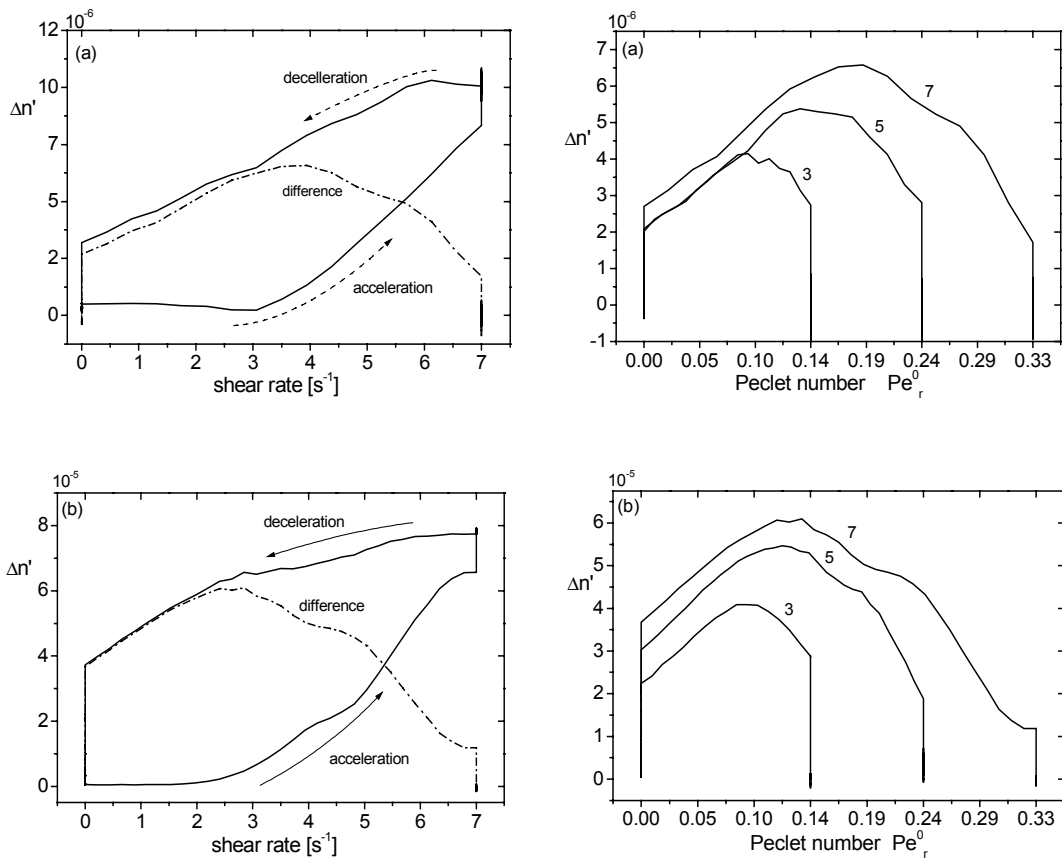
The shear-rate dependence of stationary birefringence is shown in Figure 3.9 for various concentrations. The insert shows theoretical results obtained from eq.(3.16).

For the two highest concentrations, theory predicts a jump discontinuity at low shear-rates, where the system jumps from the paranematic branch to the nematic branch.

In all the above described experiments, we found qualitative agreement between experiment and theory. This validates the use of the theory described in section 3.2.3 for the interpretation of the experimental procedure described in section 3.2.6 in order to obtain the shear-rate induced shift of spinodals.

3.3.4 HYSTERESIS EXPERIMENTS

The experimentally applied time dependence of the shear-rate during a sweep is sketched in Figure 3.4. The corresponding time dependence of the measured birefringence during a sweep (solid lines) and the difference between the two (dotted line) is plotted in Figure 3.10 for three different concentrations; 5.84, 11.18 and 13.88 mg/ml.



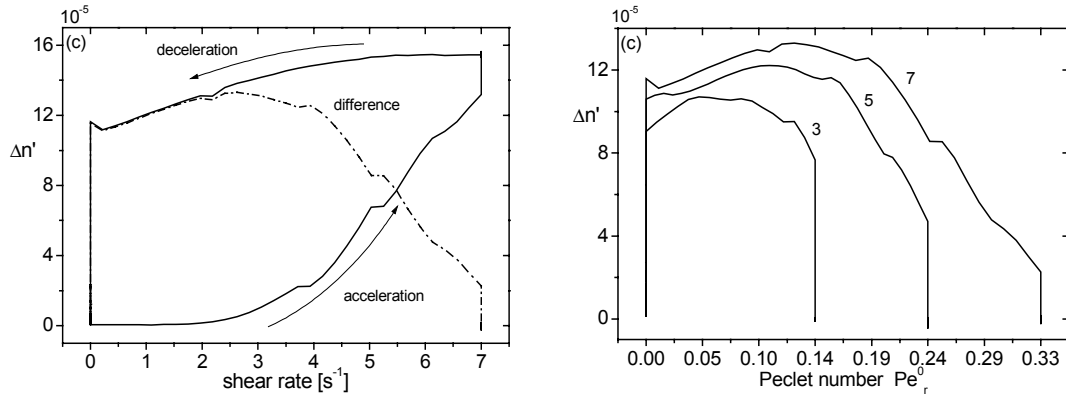


Figure 3.10: Left column of figures: birefringence as a function of the actual shear-rate during a sweep (solid lines) and the hysteresis (dotted line), for four concentrations: (a) 5.84, (b) 11.18 and (c) 13.88 mg/ml. The rate of change of the shear-rate is 7 s^{-2} (corresponding to the theoretically defined sweep rate $\frac{1}{\tau_{end}} = 0.335$, for a bare rotational diffusion coefficient of 20.9 s^{-1}), while the highest shear-rate is 7 s^{-1} (corresponding to a bare rotational Peclet number of 0.33). The actual time dependence of the measured birefringence during a sweep cycle resembles the plots in Figure 3.4. Right column of figures: hysteresis curves for three different sweep rates. The numbers in the figure refer to sweep rates $\frac{d\dot{\gamma}}{dt}$ in units of s^{-2} .

For the lowest concentration (Figure 3.10 a), the amplitude of the hysteresis curve is found to be much smaller than for the higher concentrations. This is in accordance with the theoretical prediction in Figure 3.5, pertaining to the concentration regime I as defined in subsection 3.2.6. The experimentally observed sweep rate dependence of the shear-rate where the maximum in the hysteresis curves occurs, however, is experimentally found to be more sensitive on the sweep rate as compared to theory. The form of the hysteresis curves in Figure 3.10 b resembles the theoretical curves in Figure 3.5 b, corresponding to the concentration regime II. The predicted gradual disappearance of a clear maximum in the regimes III and IV (see Figure 3.5 c and d) is also observed in the experimental Figure 3.10 c.

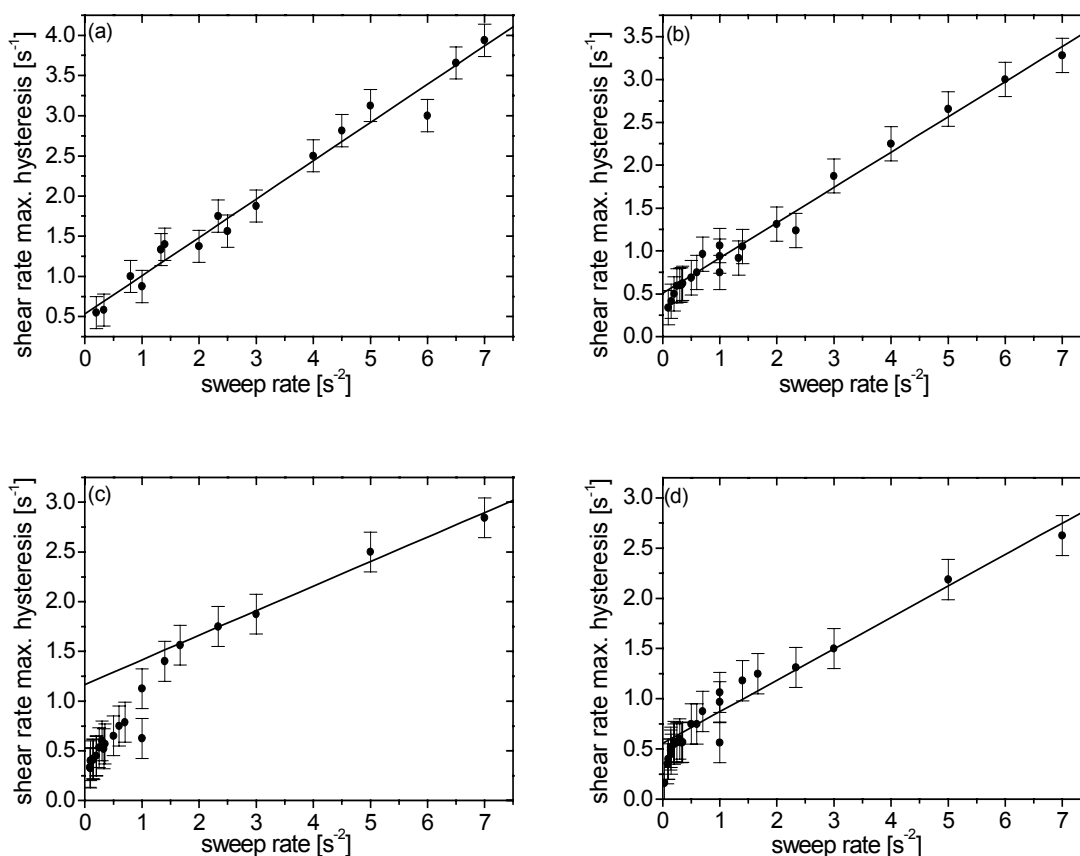


Figure 3.11: The sweep rate dependence of the shear-rate where the maximum hysteresis is found, for the concentrations: (a) 5.84, (b) 10.59, (c) 11.18 and (d) 13.88 mg/ml. The solid lines are linear fits, where data points for very small sweep rates are omitted.

The sweep rate dependence of the shear-rate where the maximum hysteresis occurs is plotted in Figure 3.11 for four different concentrations. There are two differences with the theoretical predictions in Figure 3.6. First of all, except for the lowest concentration, the curves sharply bend towards a zero shear-rate on lowering the sweep rate. The predicted essentially linear dependence is only found for somewhat larger sweep rates. In the extrapolation procedure to zero sweep rate we omitted data points for the very small sweep rates, where the sharp downward bend occurs. Secondly, the shear-rate that is found from a linear extrapolation to zero sweep rate remains finite below the critical shear-rate. This “background” is independent of concentration and seems to be equal to a similar offset at very high concentrations. These discrepancies are not yet understood. The shear-rates found from such linear extrapolations to zero sweep rates are plotted in Figure 3.12.

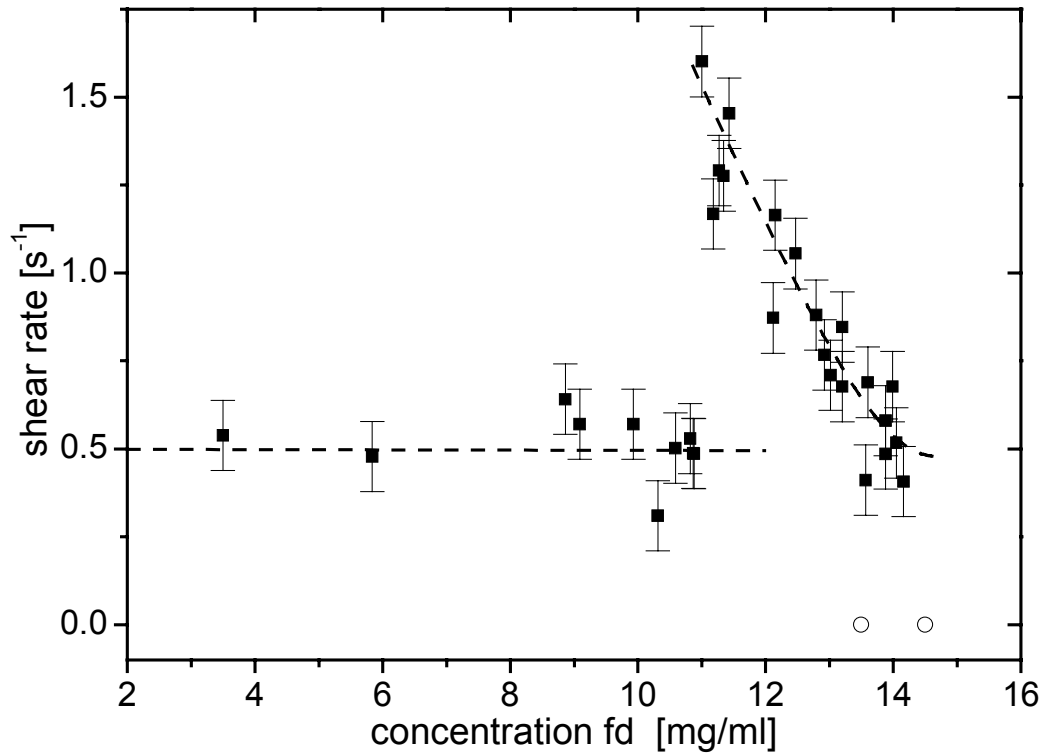


Figure 3.12: The experimentally obtained non-equilibrium phase diagram. This plot corresponds (in part) to the dotted line in Figure 3. The points \circ mark the binodal concentrations without shear flow. A dotted line is plotted to guide the eye.

The data in Figure 3.12 should be compared to the dotted line in the non-equilibrium phase diagram in Figure 3.3. The critical shear-rate that follows from Figure 3.12 is 1.6 s^{-1} . Comparing to the theoretically predicted critical Peclet number in Figure 3.3 gives a bare rotational diffusion coefficient of 11 s^{-1} . This value has been used in the previous subsection to compare experimental shear alignment curves with theoretical predictions.

3.4 SUMMARY AND CONCLUSIONS

Time resolved birefringence measurements have been used to probe the shear dependent location of isotropic-nematic spinodals in a suspension of fd-virus. The shear-rate where the maximum hysteresis occurs during a shear sweep, where the shear-rate is first increased and subsequently decreased, lies in between the paranematic-to-nematic and the nematic-to-paranematic spinodals in the shear-rate versus concentration phase diagram. The critical shear-rate beyond which no distinction can be made between the nematic and paranematic states is found to be equal to 1.6 s^{-1} . The corresponding critical concentration of fd-virus is 10.9 mg/ml , which should be compared to the binodal concentrations in the absence of shear flow of 13.0 mg/ml and 14.5 mg/ml . There is thus an appreciable shear induced shift of the spinodals, since the spinodal concentrations without shear flow are in between the binodal concentrations.

The birefringence hysteresis curves are calculated from an equation of motion for the orientational order parameter tensor, which is derived here from the N-particle Smoluchowski equation for rigid, lyotropic rods. This equation of motion is believed to be only qualitatively correct as a result of a Ginzburg-Landau type of expansion that is employed in its derivation, and due to the use of an approximate closure relation for a fourth order ensemble average. A very similar equation of motion has been considered by Doi and Edwards [19]. There are two experimental observations which are not accounted for by the above mentioned equation of motion. First of all, on extrapolation of the shear-rate where the maximum hysteresis occurs to zero sweep rates, curves turn sharply to a zero shear-rate for small sweep rates. Second, there is a “background” shear-rate outside the spinodal region, that is, the shear-rate where the maximum hysteresis occurs at zero sweep rates is found to be non-zero. These discrepancies are not yet understood. In addition, shear alignment suspensions lose their birefringence on cessation of shear flow, where the equation of motion predicts a stable nematic state. This is probably due to the formation of inhomogeneities.

3.5 REFERENCES :

1. Zocher, H., *Anorg. Allg. Chem.*, 1925. **147**: p. 91.
2. Bernal, J.D. and I. Fankuchen, *J. Gen. Physiol.*, 1941. **25**: p. 111.
3. Pelletier, O., *et al.*, *Europhys. Lett.*, 1999. **48**: p. 53.
4. Kreibig, U. and C. Wetter, *Z. Naturforsch.*, 1980. **35**: p. 750.
5. Fraden, S., *et al.*, *Phys. Rev. Lett.*, 1989. **63**: p. 2068.
6. van Bruggen, M.P.B., J.K.G. Dhont, and H.N.W. Lekkerkerker, *Macromolecules*, 1999. **32**: p. 2256.
7. Dong, X.M., *et al.*, *Langmuir*, 1996. **12**: p. 2076.
8. Folda, T., *et al.*, *Nature*, 1988. **333**: p. 55.
9. Doi, M. and S.F. Edwards, *J. Chem. Soc. Faraday Trans. 2*, 1978. **74**: p. 560.
10. Doi, M. and S.F. Edwards, *J. Chem. Soc. Faraday Trans. 2*, 1978. **74**: p. 918.
11. Edwards, S.F. and K.E. Evans, *J. Chem. Soc. Faraday Trans. 2*, 1982. **78**: p. 113.
12. Sato, T. and A. Teramoto, *Macromolecules*, 1991. **24**: p. 193.
13. Teraoka, I. and R. Hayakawa, *Journal of Chemical Physics*, 1988. **89**: p. 6989.
14. Onsager, *The effects of shape on the interaction of colloidal particles*. *Annals New York Academy of Sciences*, 1949. **51**: p. 627-659.
15. Odijk, T., *Macromolecules*, 1986. **19**: p. 2073.
16. Stroobants, A., H.N.W. Lekkerkerker, and D. Frenkel, *Evidence for one-, two-, and three-dimensional order in a system of hard parallel spherocylinders*. *Physical Review A*, 1987. **36**(6): p. 2929.
17. van der Schoot, P., *Light scattering by concentrated solutions of rodlike macromolecules.*, . 1992, Technical University Delft: Delft.
18. Vroege, G.J. and H.N.W. Lekkerkerker, *Phase transitions in lyotropic colloidal and polymer liquid crystals*. *Rep. Prog. Phys.*, 1992. **55**: p. 1241.
19. Doi, M. and S.F. Edwards, *The theory of Polymer Dynamics*. The international series of monographs on physics, ed. J. Birman, *et al.* 1986, Oxford: Clarendon Press.
20. Maeda, T., *Matrix Representation of the Dynamical Structure Factor of a Solution of Rodlike Polymers in Isotropic Phase*. *Macromolecules*, 1989. **22**: p. 1881-1890.
21. Shimada, T., M. Doi, and K. Okano, *Concentration fluctuation of stiff polymers. III. Spinodal decomposition*. *The Journal of Chemical Physics*, 1988. **88**(11): p. 7181-7186.

22. Winters, J.W., T. Odijk, and P. van der Schoot, preprint, .
23. Olmsted, P.D. and P.M. Goldhart, *Isotropic-nematic transition in shear flow: State selection, coexistence, phase transition, and critical behavior*. Physical Review A, 1992. **46**(8): p. 4966-4992.
24. Olmsted, P.D. and C.-Y.D. Lu, *Phase Separation of Rigid-Rod Suspensions in Shear Flow*. Physical Review E, 1999. **60**(4): p. 4397-4415.
25. Olmsted, P.D. and C.-Y.D. Lu, *Phase Coexistence of Complex Fluids in Shear Flow*. Faraday Discussions, 1999. **112**: p. 183-194.
26. Dhont, J.K.G., *Shear induced displacement of the spinodal of brownian systems*. Physical Review Letters, 1996. **76**: p. 4469-4272.
27. Hess, W., *Molecular theory for moderately concentrated polymer solutions in shear flow*. Rheologica acta, 1984. **23**: p. 477-488.
28. Doi, M., T. Shimada, and K. Okano, Journal of chemical physics, 1988. **88**: p. 4070.
29. Dhont, J.K.G., *An Introduction to Dynamics of Colloids*. studies in interface science, ed. D. Mobius and R. Miller. Vol. II. 1996: Elsvier. 642.
30. Maier, W. and A. Saupe, Z. Naturforsch., 1958. **13A**: p. 564.
31. Maier, W. and A. Saupe, Z. Naturforsch., 1959. **14A**: p. 882.
32. Maier, W. and A. Saupe, Z. Naturforsch., 1960. **15A**: p. 287.
33. Hinch, E.J. and L.G. Leal, Journal of Fluid Mechanics, 1976. **76**: p. 187.
34. Kayser, R.F.J. and H.J. Racheché, *Bifucation in Onsager's model of the isotropic-nematic transition*. Physical Review A, 1978. **17**(2): p. 2067-2072.
35. Bhave, A.V., *et al.*, *A constitutive equation for liquid-crystalline polymer solutions*. Journal of Rheology, 1993. **73**(3): p. 413-441.
36. Fuller, G.G., *Optical Rheometry of complex fluids*. first ed, ed. K.E. Gubbins. 1995, Cornell University: Oxford University press. 268.
37. Fraden, S., *Phase transition in colloidal suspensions of virus particles*. Observatio, Prediction, and Simulation of Phase Transitions in Complex Fluids, ed. M. Baus, L.F. Rull, and J.P. Ryckaert. Vol. 460. 1995, Dordrecht: Kluwer Academic Publishers.
38. Chen, Z.Y., Macromolecules, 1993. **26**: p. 3419.
39. Tang, J. and S. Fraden, Liquid Crystals, 1995. **19**: p. 459.
40. Fuller, G.G. and K.J. Mikkelsen, *Optical rheometry using a rotary polarization modulator*. Journal of Rheology, 1989. **33**(5): p. 761-769.
41. The hysteresis curves discussed in section 3.2.6 are obtained with a rotational diffusion coefficient equal to 20 s^{-1} . The essential features of the hysteresis curves do not change when a value of 11 s^{-1} is used instead.

Chapter 4

SHEAR-BANDED STRUCTURES IN SUSPENSIONS OF RIGID RODS

We observed the formation of stable banded structures under stationary shear flow conditions in suspensions of boehmite rods. The question addressed in this chapter is whether this banded structure is due to a Taylor instability or a shear-banding instability.

Beyond some shear rate, the position of the bands begin to oscillate in time. On further increasing the shear rate, the oscillatory behaviour becomes irregular in time. The behaviour of the banded structure is investigated for various concentrations as a function of shear rate. The Taylor number where banding is observed, is a factor two to three below the critical Taylor number. Since the well-known critical value of the Taylor number, where the Taylor instability occurs in molecular systems, may be different for colloidal systems, this does not exclude the possibility that we nevertheless observed a Taylor instability. The internal microstructure of the bands is probed by birefringence experiments, where the transmitted light through two crossed polarizers, with an optical couette cell in between, is measured. The internal structure of the shear-bands is not in accordance with what is expected for shear-banding nor for a Taylor-banded state. It could be that the instability is a Taylor instability, but that the final, stationary banded state is more complicated compared to molecular systems, due to shear-thinning effects and the existence of concentration gradients.

4.1 INTRODUCTION

Although not yet observed experimentally, one expects on the basis of theoretical considerations that in suspensions of rigid rods the so-called shear-banding instability will occur [1-3]. Shear-banding is the result of a delicate interplay between shear forces and thermodynamic forces. Theory predicts shear-banding in the neighbourhood of the paranematic-nematic two-phase region.

Shear-banding was first observed in polymer extrusion experiments on polyethylene melts [4]. Here a sudden increase of material throughput is observed on increasing the extrusion rate. This phenomenon is now referred to as “the spur effect”. As far as we know, McLeish and Ball [5, 6] were the first to explain this effect in terms of a flow instability. The apparent viscosity in the polyethylene extrusion experiment suddenly seems to decrease, this will give rise to a discontinuous increase of the material throughput. The usual flow pattern will become unstable, and the flow pattern changes abruptly to a “banded” state. Shear-banding is observed for a number of systems, like wormlike-micelles [7, 8], other kinds of surfactant systems [9-11], polycrystalline colloids of spherical particles [12-14], and in polydisperse granular matter [15]. Under controlled shear rate conditions, two different kind of shear-banded states are observed in a couette geometry, which are schematically depicted in Figure 4.1.

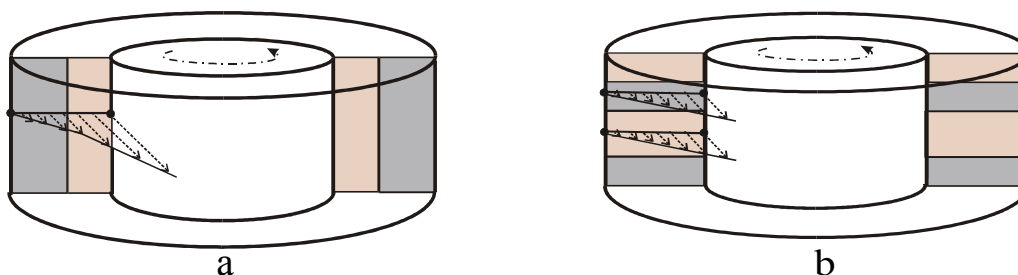


Figure 4.1: Possible shear-banded flow patterns in a Couette geometry. a) Bands in the gradient direction and b) bands in the vorticity direction. The dark area represent region with higher concentration, whereas the lighter ones represent the lower concentration.

Banded structures are observed when two bands of different shear rates “coexist” (see Figure 4.1 a). Within each band the shear rate is a constant, and the bands are interconnected by an “interface” where the spatial derivative of the shear rate is very large. The shear rate changes only along the gradient direction. The other banded structure that is observed is a structure where the microstructure of the system varies periodically along the vorticity direction (see Figure 4.1 b). The shear rate is probably

constant throughout the system, but the stresses in the gradient direction for the two states is different.

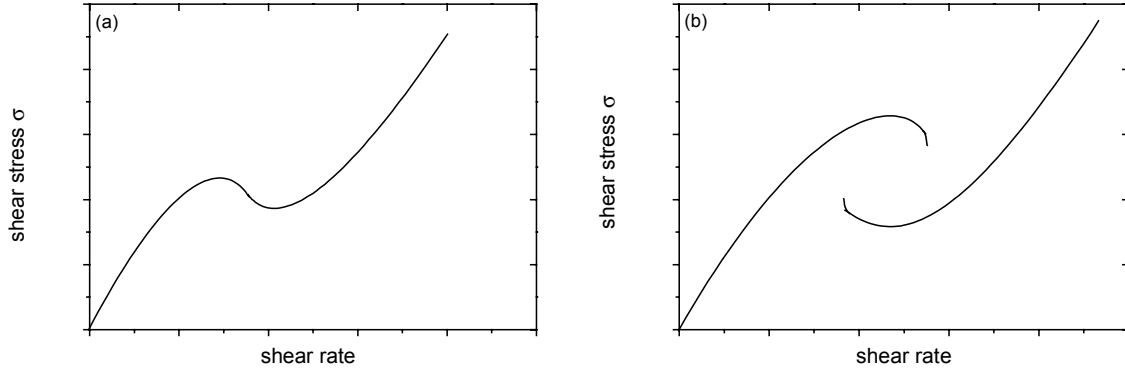


Figure 4.2: a) The van der Waals loop-like behaviour of the stress as a function of the shear rate, leading to shear-banding along the gradient direction as depicted in Figure 4.1 a, and b) the multivalued stress, leading to shear-banding along the vorticity direction as depicted in Figure 4.1 b.

Intuitively the instability of the usual linear flow profile can be understood as follows. Consider a homogeneous suspension of rod like colloids with a concentration just below the critical concentration (see Figure 3.3). On gradually increasing the shear rate, the viscosity η will decrease because of the shear induced alignment of the rods. The friction coefficient for sliding layers of suspension is lowered on the alignment of the rods. In the neighbourhood of the critical shear rate, a small increase of the shear rate leads to a relatively strong enhancement of the alignment. This is due to the very slow rotational dynamics in the neighbourhood of the spinodals, which is not sufficiently fast any more to counterbalance the aligning shear forces. This severe shear thinning behaviour can lead to a van der Waals loop-like behaviour of the stress $\sigma = \dot{\gamma} \eta(\dot{\gamma})$, as depicted in Figure 4.2 a. It is easily shown that the Navier-Stokes predicts an unstable linear flow profile when the derivative $d\sigma/d\dot{\gamma}$ is sufficiently negative [2]. The stable stationary state under controlled shear rate conditions is now the shear-banded state as sketched in Figure 4.1 a. Stability of this banded state requires the stresses along the gradient direction to be equal in the two bands, that is, the two shear rates must give rise to the same stress. For higher concentrations, within the two-phase region, the two stable states each have their own stress versus shear rate dependence. These are the two branches plotted in Figure 4.2 b. Under controlled shear rate conditions bands can now “coexists” with identical shear rate but each with a microstructure that pertains either to the nematic branch or the paranematic branch.

A second kind of instability that occurs in a couette geometry, which is also found in molecular systems, is the Taylor instability [16, 17]. This is an instability that occurs at relatively high shear rates, and is due to large centrifugal forces on suspension volume elements. This classic instability gives rise to a flow pattern as depicted in Figure 4.3. Bands are formed along the vorticity direction, like in the shear-banding scenario depicted in Figure 4.1 b, but the bands now have a more complicated internal structure.

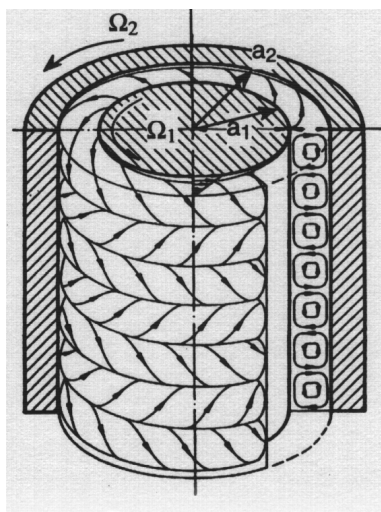


Figure 4.3: The stable flow pattern in a Taylor-banded structure [18].

In this paper we investigate possible flow instabilities in a colloidal system of rigid, rod-like particles. The colloidal system and the experimental set up are introduced in section 4.2, section 4.3 contains the experimental observations and we conclude with a discussion.

4.2 THE COLLOIDAL SYSTEM AND EXPERIMENTAL SET-UP

The system used to perform the experiments consists of boehmite rods. The synthesis of these aluminium hydroxide particles is described by Buining [19]. The rods have an average length of 108 nm with a polydispersity of 30% and a thickness of 9 nm with a polydispersity of 23 %, as determined from electron microscopy. The solvent is water. To stabilise the rods against van der Waals attractions, 0.5 weight % of ACH (Aluminium Chloride Hydrate) is added. ACH strongly adsorbs onto the rods and provides a stabilising polymer-like layer [20]. To reduce and control the double layer interactions, 0.01 M NaCl was added [20]. To our surprise we could not detect the isotropic-to-nematic phase transition in the quiescent system.

An outline of the experimental set up is given in Figure 4.4. A 2D CCD-camera detects the white light that is transmitted through an optical couette cell, immersed in a thermostating optical bath containing toluene. This bath is located in between two crossed polarizers. The angles of the polarizers with respect to the vorticity direction will be varied in an experiment.

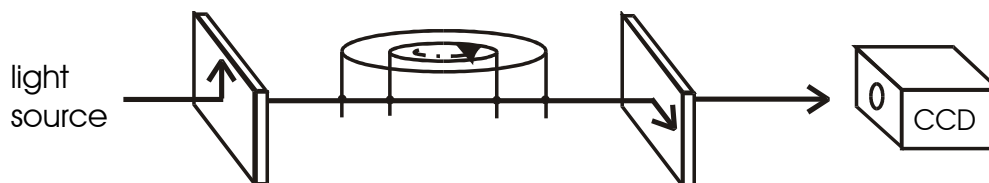


Figure 4.4: The experimental set up. White light is direction along the gradient direction of an optical couette cell, which is located between two crossed polarizers. The transmitted light is detected by means of a 2D CCD-camera.

All CCD-pictures are corrected for background intensity. The couette cell is described in Chapter 1: the inner cylinder is rotated here with respect to the stationary outer cylinder, the gapwidth is 2.47 mm and the radius of the inner cylinder is 21.5 mm.

4.3 EXPERIMENTAL RESULTS

A typical CCD-picture is shown in Figure 4.5. The polarization direction of the incident light is along the vorticity direction.

These results are typical for the volume fraction range of 1 to 3 %. The transmitted light pattern was found to be independent of the shear history of the system: fast and slow shear rate accelerations gave rise to identical CCD-patterns. For zero shear rate the CCD-picture is uniformly black, indicating that the microstructure at rest is isotropic. For a relatively low shear rate, the shear forces uniformly align the rods into a paranematic state, giving rise to a uniformly white CCD-pattern (see Figure 4.5 a).

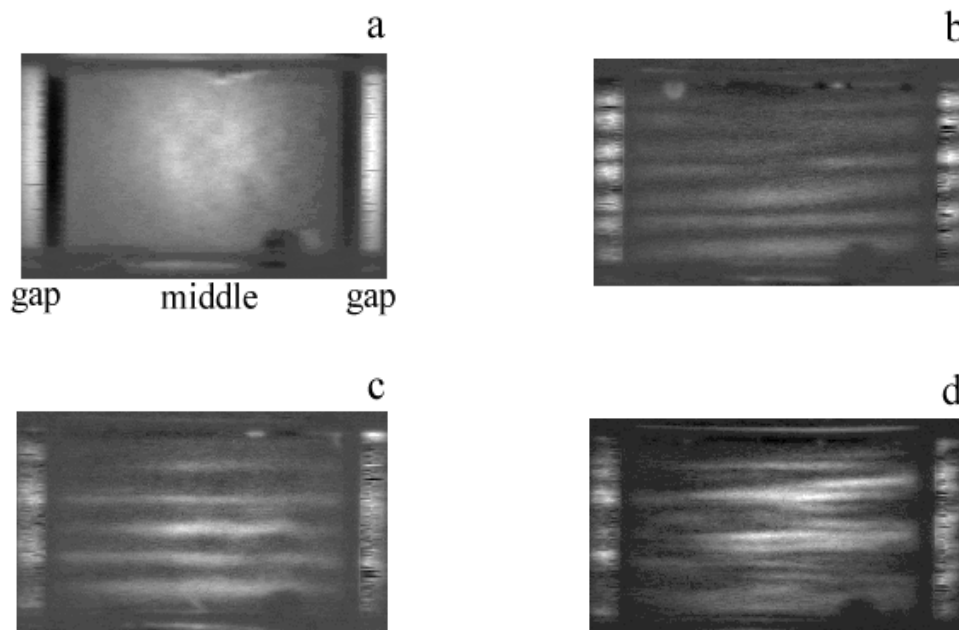


Figure 4.5: CCD-pictures for a volume fraction of 1.8 % at various shear rates: a) 79, b) 108, c) 173 and d) 284 s^{-1} . The polarization direction of the first polarizer (the polarizer on the left in Figure 4.4) is along the vorticity direction.

The inhomogeneity seen in Figure 4.5 a is due to optical effects of the shear cell and the thermostating bath, as well as the finite diameter of the incident beam of white light. The gap as seen in the flow direction (at the edges on the left and right sides of Figure 4.5 a) is relatively bright due to the large optical path length. Above a certain shear rate, a banded structure is observed, as can be seen in Figure 4.5 b. Increasing the shear rate further, the banded structure begins to oscillate, rendering a CCD-figure that is a bit blurred, especially at the edges, where the optical path length is relatively large (Figure 4.5 c). Increasing the shear rate even further, the band oscillations change to an irregular time dependence of the position of the bands, rendering the blurry CCD-pattern shown in Figure 4.5 d.

The banded structures described above are observed at all concentrations we investigated (between a volume fraction of 1 and 3 %). A “non-equilibrium phase diagram” is shown in Figure 4.6. Four different regions can be distinguished: A homogeneous paranematic state (corresponding to Figure 4.5 a), a stable banded structure (Figure 4.5 b), an oscillating banded structure (Figure 4.5 c) and an “unstable” banded structure, where the position of the bands fluctuate in an irregular fashion. As can be seen, the “state-transition points” tend to shift to higher shear rates at higher concentrations.

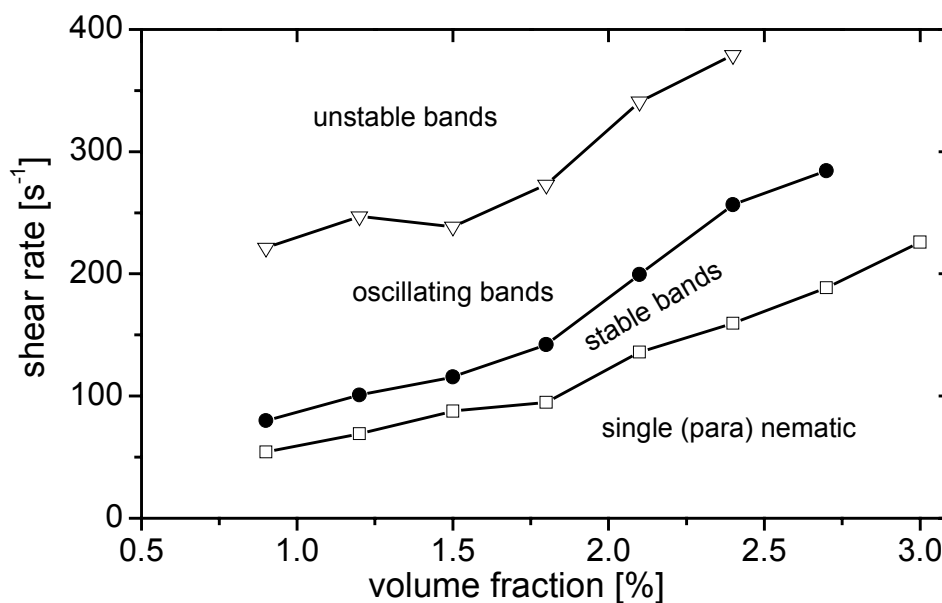


Figure 4.6: The non-equilibrium phase diagram. The lines indicate the transition from one state to the other. The various states are described in the main text.

To further investigate the flow pattern in case a stable banded structure is observed, where no oscillations nor irregular movement of the bands occur, CCD-patterns are recorded for different orientations of the two polarizers. In this way the microstructure within the bands can be resolved to some extent. The CCD-pictures that were taken for different polarizer orientations are shown in Figure 4.7. Figure 4.7 a, where the first polarizer is along the vorticity direction, shows a band structure where thick and thin white bands seem to alternate. The thicker bands can be seen to be somewhat tilted with respect to the horizontal thinner bands. It seems as if the thicker bands form a spiral-like structure. Rotating the polarizers 25 degrees, relative to the flow direction clockwise (see Figure 4.7 b), gives a banded structure that is very coarse in comparison to the previous case in Figure 4.7 a. A further clockwise rotation to 45 degrees yields a CCD-pattern where pairs of bands are seen (see Figure 4.7 c). Three broad bands are observed with an internal structure that leads to a relatively dark region in the middle of the bands. For an angle of 65 degrees of the first polarizer with respect to the vorticity direction, three uniform white bands separated by a broad black region are observed (see Figure 4.7 d). Note that the white regions in the gaps (at the edges of the CCD-pattern) seem to be “out of phase” with the observed white bands.

In Figure 4.8 it is shown what happens to the CCD-pattern on reversing the rotational velocity of the inner cylinder. Although difficult to see from Figure 4.8, the narrow

white bands remain horizontal on reversing the rotation direction of the inner cylinder. The broad white bands, however, reverse their tilt.

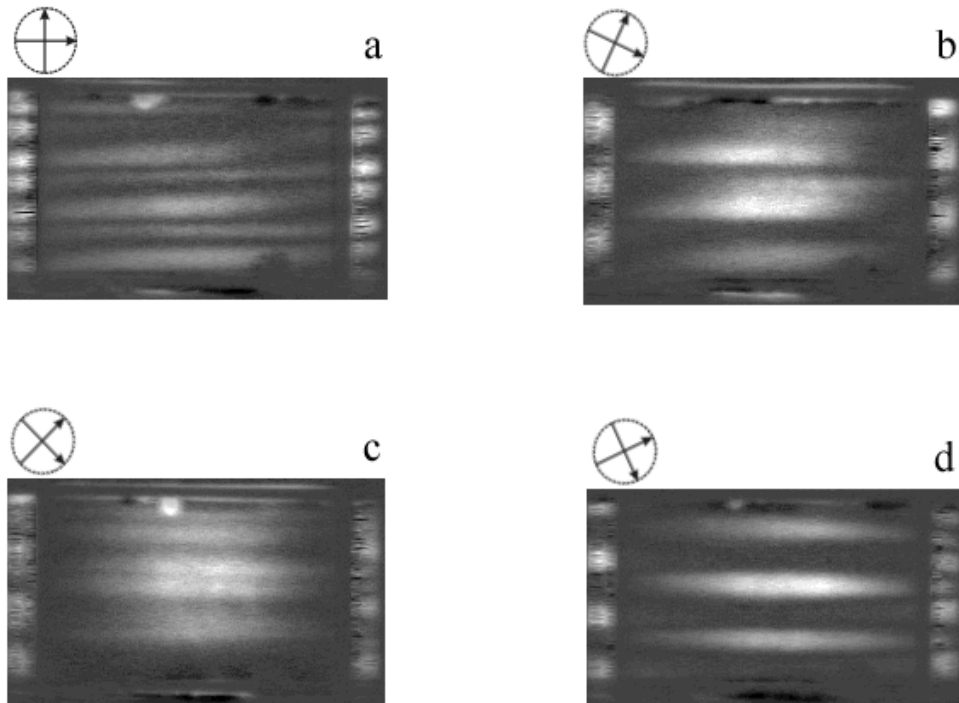


Figure 4.7: CCD-patterns of a stable banded structure for various orientations of the polarizers, as indicated in the figures. The angles of the first polarizer (the polarizer on the left in fig.4) relative to the flow direction are a) 0, b) 25, c) 45 and d) 65 degrees.

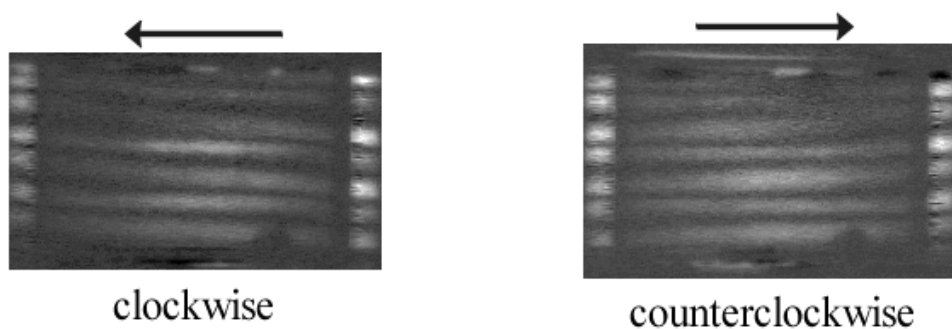


Figure 4.8: CCD-patterns for two different rotation directions of the inner cylinder. The arrows indicate the velocity of the face of the inner cylinder closest to the CCD camera. The volume fraction is 1.8 % and the shear rate is 110 s^{-1} , corresponding to the situation in Figure 4.7 a.

The average width of these bands could in principle be affected by the height of the sample within the gap of the couette cell. As can be seen from Figure 4.9, however, the width of the bands is almost independent of the sample height, except for very small sample heights. It thus seems that the suspension boundaries at the top and bottom of the couette cell hardly affect the shear-banded structure.

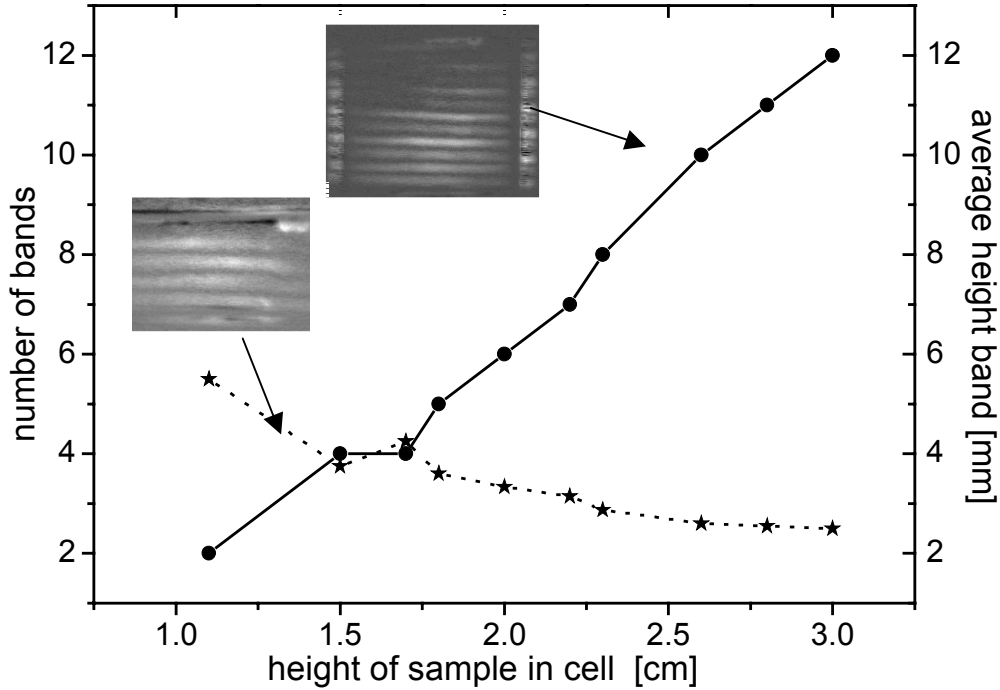


Figure 4.9: The number of observed bands (dotted line) and their average width (solid line) as a function of the sample height within the gap of the couette cell.

4.4 DISCUSSION AND CONCLUSION

In case of a couette cell where the inner cylinder rotates, the criterion for a Taylor instability to occur is that the so-called Taylor number Ta is larger than about 3400 (see eq.(4.1)). The Taylor number is related to the mass-density ρ of the suspension, the angular velocity Ω_i of the inner cylinder (in radians per unit time), the gapwidth g , the radius R_i of the inner cylinder and the suspension shear viscosity $\eta(\dot{\gamma})$.

$$Ta = \frac{\rho^2 \Omega_i g^3 R_i}{\eta(\dot{\gamma})^2} < 3400 \quad (4.1)$$

This criterion for the occurrence of the Taylor instability is valid for Newtonian fluids, where the viscosity is shear rate independent, and the density is uniform. For the low volume fractions of interest here, the mass-density of the suspension is almost equal to that of water. Shear viscosity data for our boehmite system are plotted in Figure 4.10 as a function of the shear rate for various volume fractions of rods. The suspension is found to be shear-thinning slightly only at volume fractions above approximately 2 %. One might therefore conclude that the above criterion for the occurrence of the Taylor instability is accurate for our boehmite suspensions. However, since the local shear rates within the banded structures can be much larger than the overall applied shear rate, this statement should be interpreted with some care. It might be that the local shear rates within the banded structure are so large that shear-thinning does influence the above criterion. In addition, concentrations of boehmite rods may not be uniform in a shear banded state, leading to a spatial variation of the viscosity.

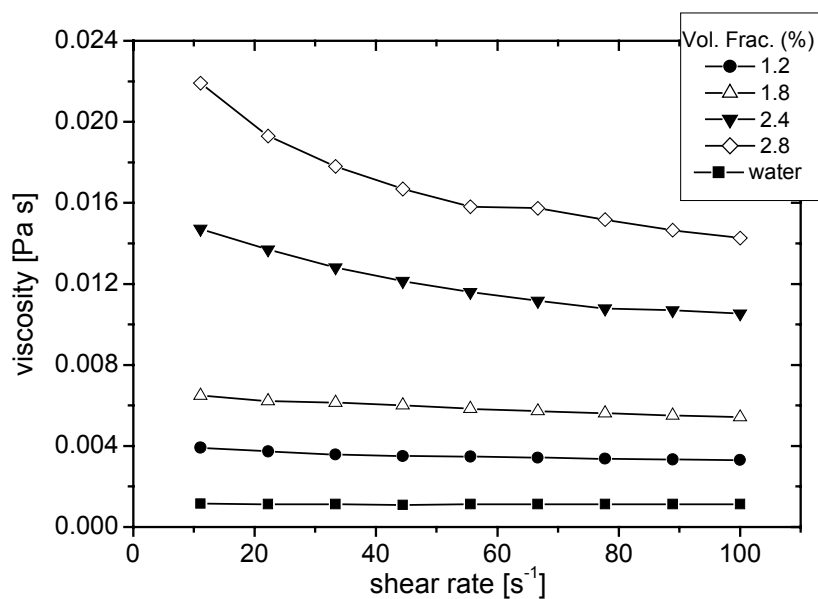


Figure 4.10: Shear viscosity as a function of the shear rate for various volume fractions of boehmite rods, as indicated in the figure.

The Taylor number as calculated from the above viscosity data for the lowest shear rate where a banded structure is found is always less than half its critical value (see the table below). In view of the reservations concerning the validity of the above mentioned criterion for a Taylor instability to occur, it remains uncertain whether we have observed a Taylor instability or a shear-banding instability.

Volume fraction	Taylor number
1.2	1749
1.8	1273
2.4	1085

Table 4.1: The Taylor number for three different concentrations for the smallest shear rate where banding is observed.

The internal structure of the bands as probed by rotation of the polarizers in section 4.3 is quite different for a banded state due to a Taylor instability or a shear-banding instability. What is not expected for both instabilities is the tilt of some of the bands. What is expected to be seen in case of shear-banding is that on rotation of the polarizers the white bands turn black and vice versa, since within the bands the microstructure should be uniform. From Figure 4.7 it is clear that the bands have a non-uniform internal microstructure. What is not in accordance with a Taylor instability is an alternating structure of broad white bands and relatively thin white bands as found in Figure 4.7 a. It could be that the instability that occurs in our boehmite system is nevertheless a Taylor instability, but that the final, stationary state is different from that of molecular systems, due to shear-thinning effects and the existence of concentration gradients. The precise structure of the banded state requires additional experimentation.

4.5 REFERENCES :

1. Olmsted, P.D., Europhysics Letters, 1999. **48**: p. 339-345.
2. Dhont, J.K.G., Phys. Rev. E, **60**, 4534 (1999).
3. Olmsted, P.D. and C.-Y.D. Lu, Phys. Rev. E, **60**, 4397 (1999).
4. Bagley, E.B., I.M. Cabot, and D.C. West, J. Appl. Phys., **29**, 109 (1958).
5. McLeish, T.C.B. and R.C. Ball, J. Polym. Sci., **24**, 1735 (1986).
6. Doi, M. and S.F. Edwards, *The theory of Polymer Dynamics*. The international series of monographs on physics, ed. J. Birman, *et al.* 1986, Oxford: Clarendon Press.
7. Berret, J.-F., D.C. Roux, and G. Porte, J. Phys. II (France), **3**, 1261 (1994).
8. Schimtt, V., *et al.*, Langmuir, **10**, 955 (1994).
9. Bonn, D., *et al.*, Phys. Rev. E., **58**, 2115 (1998).
10. Diat, O., D.C. Roux, and G. Porte, J. Phys. II (France), **4**, 1261 (1994).
11. Sierro, P. and D.C. Roux, Phys. Rev. Lett., **78**, 1496 (1997).
12. Imhof, A., A. van Blaaderen, and J.K.G. Dhont, Langmuir, **10**, 3477 (1994).
13. Palberg, T. and M. Wurth, J. Phys. I (France), **6**, 237 (1996).
14. von Hunerbein, S., M. Wurth, and T. Palberg, Prog. Coll. Polym. Sci., **100**, 241 (1996).
15. Bardenhagen, P.T., J.U. Brackhill, and D.L. Sulsky. *Shear deformation in Granular material*. in *Proc. 11th Int. Symp. on Det.* 1998. Snowmass, Colorado, USA.
16. Taylor, G.I., Philos. Trans. R. Soc. London A, **223**, 289 (1923).
17. Di Prima, R.C. and H.L. Swinney, *Instabilities and Transition in Flow Between Concentric Rotating Cylinders*. Topics in Applied Physics, ed. H.L. Swinney and J.P. Gollup. Vol. 45: Springer-Verlag.
18. Castaing, B., *Hydrodynamics and Nonlinear Instabilities*. first ed, ed. C. Godreche and P. Manneville. 1998, Cambridge: Cambridge University Press.
19. Buining, P.A., *et al.*, J. Am. Ceram. Soc., 1991. **74**(6): p. 1303.
20. van Bruggen, M., *Liquid Crystals formation and diffusion in dispersions of colloidal rods*, in *Debye Institute, Van't Hoff Laboratory*. 1998, University of Utrecht: Utrecht. p. 207.

SUMMARY

The aim of this thesis is to investigate the structure formation and deformation in colloidal systems due to an externally applied shear flow. The focus is on two different kind of colloidal systems: suspensions of attractive spherical colloidal particles in the neighbourhood of a gas-liquid critical point and suspensions of rod-like colloidal particles.

In Chapter 2 deals with the shear induced deformation of long ranged, critical microstructure of a colloid-polymer mixture close to it's gas-liquid critical point. The colloidal system consists of stearyl silica spheres and Polydimethylsiloxane (PDMS) dissolved in cyclohexane. The polymer PDMS induces so-called depletion attractions between the colloidal spheres, giving rise to a gas-liquid critical point. Close to the critical point, the spatial extent of effective interactions between the colloidal particles is very large and the dynamics of concentration fluctuations is very slow. These two properties of near-critical systems causes their microstructure to be sensitive to an externally applied shear flow. Shear flow does not affect correlations in the plane perpendicular to the flow direction, whereas in other directions there is a severe breakdown of structure. The microstructure under shear sflow is thus extremely anisotropic. This anisotropy in microstructure leads to a turbidity that is dependent on the polarisation direction of the light, a phenomenon that is commonly referred to as dichroism. Shear induced dichroism is measured as a function of shear rate and the distance from the critical point. Our experiments are in agreement a theoretical mean-field scaling relation that is derived from the Smoluchowski equation. This scaling relation predicts that a plot of the shear induced dichroism divided by the square-root of the shear rate versus the shear-rate multiplied by the fourth power of the correlation length is independent of the distance to the critical point. All experimental curves indeed collapse onto the same master curve, which agrees with the theoretically predict curve, up to a correlation length of about 700 nm. For correlation lengths larger than 750 nm, an unexpected decrease of the dichroism

on approach of the critical point is observed. Theory in this beyond mean-field region requires the solution of non-linear equations of motion for the pair-correlation function. So far, these non-linear equations of motion have not been solved

In Chapter 3, the shear-rate dependent location of paranematic-nematic spinodals for suspensions of fd-virus particles is investigated. Fd-virus is a rod-like plant virus with a length of 880 nm, a thickness of 6 nm and has a persistence length of 2000 nm. Contrary to the above described critical system, the shear-rate dependence of the pair-correlation is relatively unimportant for these rods-like colloids as compared to the shear-rate dependence of single particle probability density functions. The tendency of the shear flow to align the rods is the most important feature that causes the shear rate induced shift of phase transition lines. The experimental technique used here is time resolved birefringence. Hysteresis experiments are performed, where the shear-rate is first increased in time and subsequently decreased. The shear-rate where the maximum hysteresis in birefringence is found is a measure for the location of the paranematic-nematic spinodals. The hysteresis experiments are interpreted on the basis of an approximate solution of the Smoluchowski equation for stiff rods. There are some features that we find experimentally, which are not yet understood. The measured spinodal concentrations shift to lower values on increasing the shear-rate, as expected. The critical shear rate, beyond which no phase transition occurs anymore, is in reasonable agreement with the prediction of the approximate solution of the Smoluchowski equation.

In Chapter 4 of this thesis, we report preliminary results on a flow instability that is observed in suspensions of stiff, rod-like colloids. The colloidal system consists of boehmite rods, partly stabilized against van der Waals attractions by absorbing a polymer on the surface of the rods. Under shear flow, two kind of flow instabilities can in principle occur: the classic Taylor instability and the shear-banding instability. In both case one observes a banded structure along the vorticity direction in a couette cell. The internal microstructure of the bands, however, is different for both instabilities. We attempted to study the microstructure within the bands by measuring the transmitted intensity, with the shear cell located in between two crossed polarizers. It was found that the internal band structure does not comply with either the classic Taylor structures nor with the structure that is expected for the shear-banding instability. What probably happens is that the initial instability is of the Taylor type, but that the final stationary state is different from what is predicted for Newtonian fluids with a constant density, due to shear-thinning effects and possible variations of boehmite concentrations. Local shear-rates are probably very large, so

that shear-thinning may play a role in determining the final stationary state. In addition, in these suspensions the concentration of boehmite rods may be inhomogeneous: such density inhomogeneities are absent in incompressible simple fluids. Further research is required to fully unravel the internal microstructure of the bands.

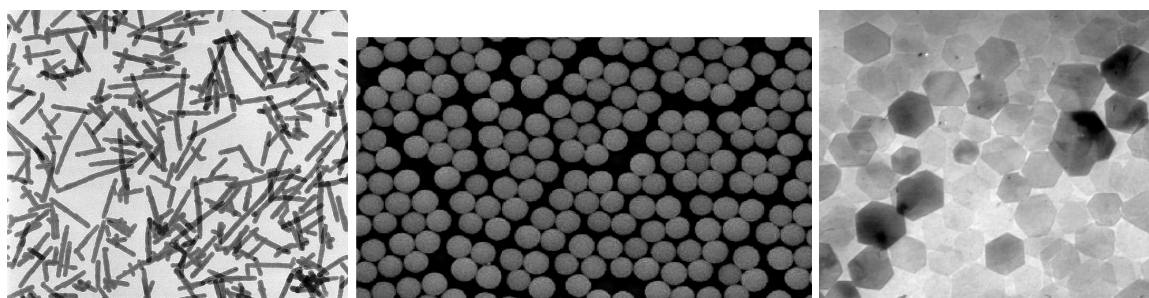
DE ESSENTIE NA 4 JAAR

In de loop der jaren heeft de schrijver ondervonden dat het uitleggen van wat zijn onderzoek inhield, geen vanzelfsprekendheid was. Wanneer de resultaten concreet bruikbaar zijn in het dagelijkse leven, dan begrijpt men het sneller. Helaas, het onderzoek beschreven in deze thesis heeft nog geen enkele directe toepassing. De hele opzet van het werk bestaat uit experimenten en mathematische modellen die een verklaring proberen te vinden voor bepaalde fysische fenomenen. Dit is een zoektocht naar zuiver wetenschappelijke kennis, die ons misschien veel later van pas kan zijn. Deze tekst is een korte samenvatting van 4 jaar bloed, zweet en tranen. Niet alle aspecten van het onderzoek zullen worden behandeld omdat men dan verdwaalt in alle gegevens.

TUSSEN ATOMEN/MOLECULEN EN ZANDKORREL

Een heel belangrijk thema in deze thesis zijn colloïden. Wat zijn dat nu? Colloïden zijn kleine deeltjes met een grootte tussen een $1000\ 000^{\text{ste}}$ en een $1\ 000^{\text{ste}}$ van een millimeter. Om de lezer een idee te geven van de grootte; ongeveer een factor 10 kleiner dan de rode bloedcellen in ons lichaam (rode bloed cel, rond schijfje van ongeveer 0.008 op 0.002 millimeter).

De colloïdale systemen, ook wel dispersies genoemd, waarmee in dit vakgebied gewerkt wordt, bestaan uit een vloeistof (het oplosmiddel) en de colloïdale deeltjes. Het geheel is dus niets anders dan een pot met een vloeistof en hele kleine niet opgeloste vaste deeltjes erin, denk aan een pot met modder. Het enige verschil met de modder is dat colloïden kleiner zijn dan de zand korrels en er wordt meestal gewerkt met veel verdundere systemen (vergelijkbaar met 100 gram zand op een emmer water (10 liter)). Nu zijn scheikundige erin geslaagd om colloïden te maken met verschillende goed gedefinieerde vormen zoals staven, bollen, platen,... (zie Figuur 1). In een colloïdale dispersie zijn de colloïden bijna allemaal even groot en dat helpt bij de bestudering van hun gedragingen.



Figuur 1: Foto's gemaakt met een krachtige microscoop. a) Aluminiumhydroxide staafjes 500 nm lang en 10 nm dik b) Latex bollen met een diameter van 1200 nm. en c) Aluminiumhydroxide plaatjes met een dikte van 10 nm en een diameter van 200 nm.

Omdat colloïden zo klein zijn zinken ze niet naar de bodem, maar ze bewegen zich door het oplosmiddel, ze vertonen diffuus gedrag. Deze random beweging door de oplossing wordt ook wel Brownse diffusie genoemd. Het is zo dat in een glas met water de moleculen op het eerste oog stil staan want er is geen stroming te zien in het glas. In werkelijkheid bewegen en botsen ze als gekken en dit komt door de warmte. Dit geldt voor alle vloeistoffen, ook voor het oplosmiddel van onze colloïdale dispersie. Bij deze bewegingen botsen vele oplosmiddel-moleculen tegen de grotere colloïden die op hun beurt in beweging komen. Je kunt het vergelijken met de thermiek in de bergen. Zweefvliegers maken gebruik van die stroom van warme lucht

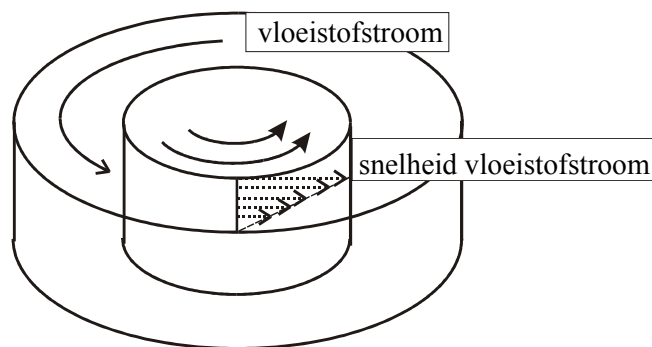
om te blijven zweven. De ‘warme’ lucht atomen/moleculen botsen tegen de onderkant van de vleugels van de zweefvlieger en die blijft daarom zweven. Het enig verschil met de colloïdale wereld is dat deze thermische luchtstroming 1 kant op gaat en bij colloïdale dispersies gaan de moleculen willekeurig alle kanten op. Het totale gedrag van de colloïden bestaat dus uit onregelmatige bewegingen, alle kanten op, eigenlijk net als de oplosmiddel moleculen. Omdat colloïden een factor 100 groter zijn dan de moleculen/atomen van het oplosmiddel, bewegen ze wel trager, hetgeen ons zeker van pas komt omdat de experimentele apparatuur moeite heeft met de kleine en snelle atomen/moleculen.

Wat de wetenschappers nu doen is het oplosmiddel weg denken. In de theorie ‘vergeet’ men dat de colloïden zich in een vloeistof bevinden. De reden dat dit kan is juist dit verschil in de grootte. Op de tijdschaal dat we de colloïden proberen te bestuderen zijn de atomen en moleculen niet meer van belang omdat ze juist zo snel bewegen t.o.v. van de colloïden. Je kan het vergelijken met het volgende. Je wil een foto nemen van een voortbewegende schildpad. Je neemt dan een langere sluitertijd omdat de schildpad zich langzaam voortbeweegt. Wanneer er dan een haas snel door het beeld gaat bewegen, dan krijg je vegen in de foto. Bewegen er nu miljoenen hazen snel alle kanten op dan is de hele foto vaag en zou je met foto-trucage de constante ‘achtergrond’ gewoon kunnen weghalen om een scherpe foto van de schildpad te krijgen. De moleculen/atomen geven ook zo’n vaag constant beeld en wij denken ze gewoon weg omdat ze toch overal zitten.

METEN IS ...

Wat er bestudeerd gaat worden, is het gedrag van colloïden in stromingen, of anders gezegd, wat gebeurt er als een dispersie wordt geroerd. Om dit te kunnen bepalen is er een speciaal apparaat gemaakt dat bepaalde optische eigenschappen van colloïdale dispersies kan onderzoeken (zie tekening Figure 1.3, p 8 en foto achterkant kft). Om het verhaal niet te ingewikkeld te maken wordt beschrijving van de experimentele opstelling achterwegen gelaten. Ook de uitleg nodig om de optische effecten in de geroerde dispersies te begrijpen, word overgeslaan omdat dit te ver zou leiden.

Eén aspect betreffende de experimentele opstelling moet wel even kort vernoemd worden, dat is namelijk de cel waar de colloïdale dispersie in werd geroerd (zie Figure 1.5, p 10). Dit roeren gebeurde op een speciale manier zodat de stroming die er ontstaat goed gedefinieerd is. De binnencilinder wordt gedraaid met als gevolg dat de vloeistof in de spleet tussen de twee cilinders (aangegeven met ‘sample’ in Figure 1.5) gaat stromen met een goed bekend stromings-en snelheidsprofiel (zie tekening Figuur 2).



Figuur 2: Bovenaanzicht stromingsprofiel in monster cel. Binnen cylinder draait rond. De snelheid waarmee de vloeistof mee beweegt neemt linear af naar de buiten cylinder, waar de vloeistof stil staat. Dit profiel is voorgesteld door de pijlen, hoe groter de pijl hoe harder de vloeistof mee vloeit. De pijlen geven niet de stroom richting aan, die is concentrisch aan de twee cylinders van de cel.

De reden dat we dit goed gedefinieerde stromingsveld willen hebben, is dat er voor dit stromingsveld goede beschrijvende formules bestaan die eenvoudig zijn in de berekeningen. Stel we zouden andere stromingspatronen aanleggen met bijvoorbeeld een mixer, dan worden de berekeningen een heel stuk moeilijker.

EN DAN ... WETENSCHAP

In deze thesis is er duidelijkheid gezocht voor drie verschillende problemen. Alle hebben ze colloïden en roeren gemeen.

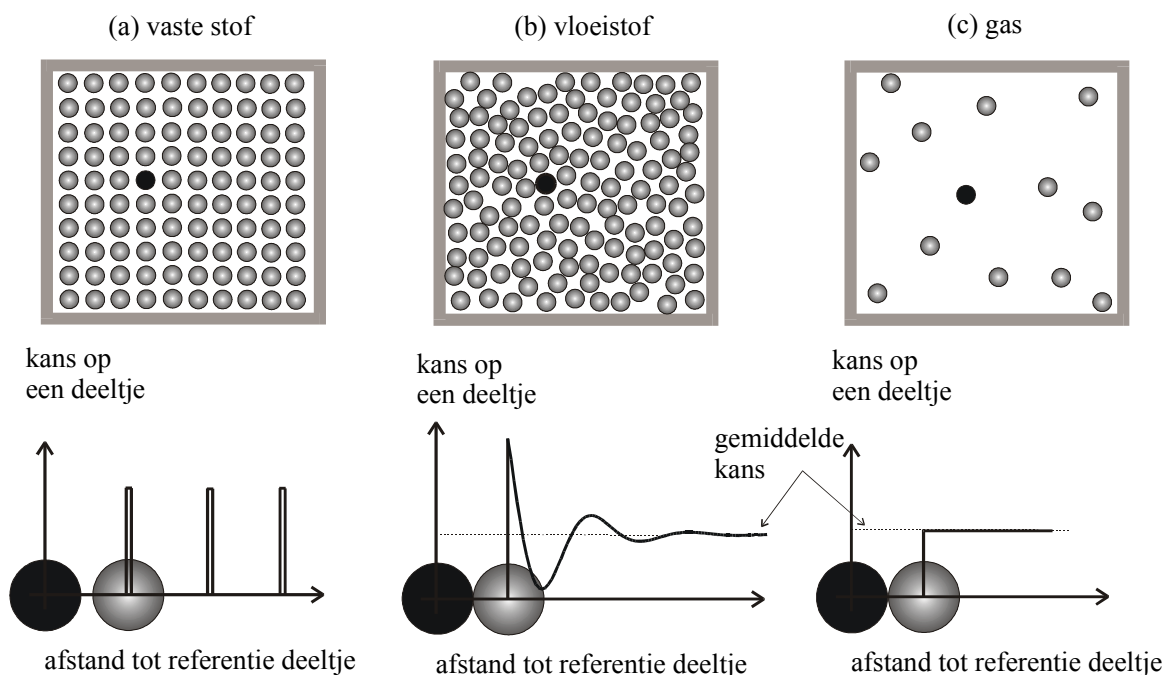
Men kan zich voorstellen dat de vorm van het kleine deeltje invloed heeft op de reactie op het opgelegde stromingsveld. Dit is te vergelijken met een bal en een speer. Als de bal weg gegooid wordt, maakt het niet uit hoe je de bal vast pakt omdat die rond is. De bal vliegt altijd even ver. Wil je een speer weg gooien, dan maakt het wel degelijk uit hoe je de speer vasthoudt. Gooi je de speer parallel met zijn voortbewegingsrichting, net als een speerwerper, dan vliegt hij een behoorlijk eindje weg. Gooi je de speer daarentegen loodrecht op zijn voortbewegingsrichting dan kom je niet ver door de extra weerstand die deze oriëntatie heeft. Deze vormafhankelijkheid en oriëntatie afhankelijkheid vind je ook in stromingen van colloïdale dispersies. Er is nu wel een extra factor die een rol speelt, namelijk het feit dat er niet één colloïd zich beweegt in de vloeistof stroming, maar miljarden en dat heeft zijn gevolgen want ze zullen elkaar beïnvloeden door bijvoorbeeld botsingen.

In de nu drie volgende paragrafen zal ingegaan worden op de onderwerpen onderzocht in deze thesis.

A) BOLLEN

Vaste stoffen hebben een regelmatige structuur. De atomen/moleculen zijn gerangschikt over grote afstanden en ze blijven netjes op hun plaats zitten, zoals bijvoorbeeld in ijs, suiker en zout kristallen en nog veel meer. Nu hebben vloeistoffen ook een soort van structuur. Deze is niet zo regelmatig als een vaste stof maar toch, er is een bepaalde regelmatigheid in te vinden, vooral op zeer korte afstanden (enkele malen de diameter van een atoom, dus heel kort). Het gaat nu niet over vaste posities van atomen/moleculen net als in vaste stoffen, maar meer over waar deeltjes zich gemiddeld het vaakste bevinden.

Nu bestaat er nog een fase, namelijk de gasfase. In deze toestand, waar er weinig deeltjes zijn per volume, bestaat er geen enkele orde meer, de deeltjes zijn ongeordend. Hieronder zijn plaatjes van hoe men vaste, vloeistoffen en gassen kan voorstellen.



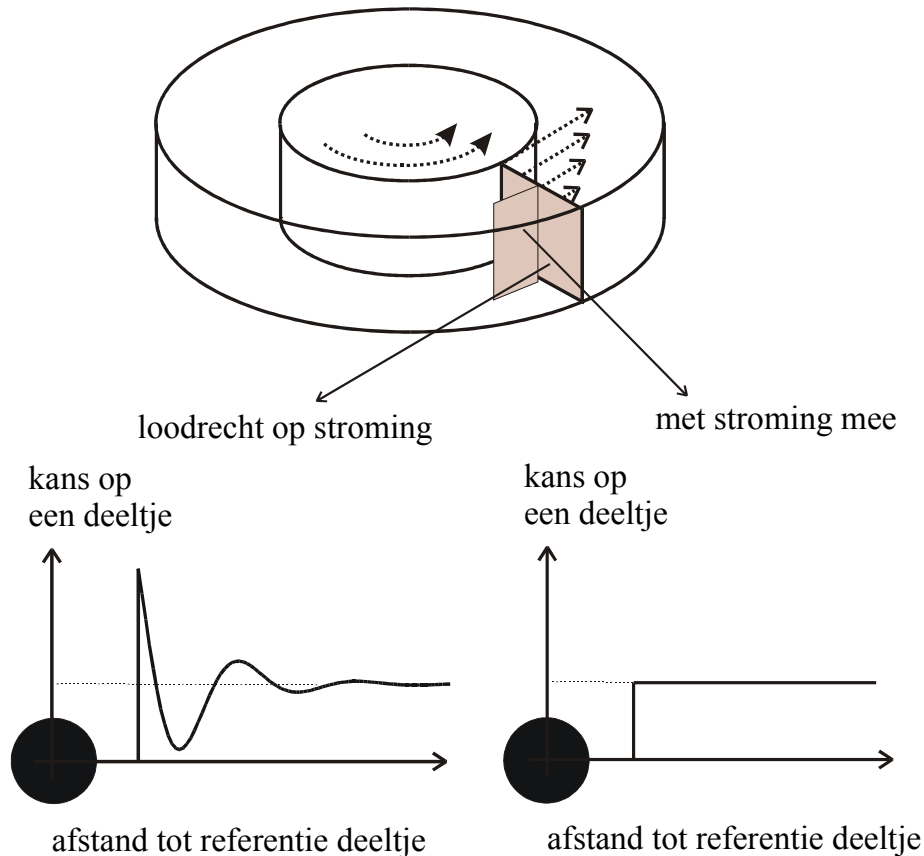
Figuur 3: Schematische voorstelling van een a) vaste stof; b) vloeistof en c) gas. Onder de tekening zijn correlatie functies getekend. Voor een vloeistof dempt de functie naar een gemiddelde kans die niet meer afhankelijk is van de positie t.o.v. een referentie deeltje. Bij een gas toestand is die afhankelijkheid onmiddellijk weg en is er overal een even grote kans. Bij de vaste stof zijn duidelijk posities waar deeltjes zitten en waar er geen zijn en deze positie afhankelijkheid zeer lang doorgaan.

Nu hebben wetenschappers bedacht om die positie ordening wiskundig voor te stellen, namelijk met behulp van een correlatie functie. Deze functie stelt de kans voor dat een deeltje op een bepaalde plaats zit ten opzichte van een referentie deeltje. In de tekening Figuur 3, kan je duidelijk het verschil zien tussen een vaste stof, waar de deeltjes regelmatige posities hebben en een vloeistof. In de vloeistof is te zien dat dicht bij het referentie deeltje er posities zijn waar de andere atomen/moleculen liever zitten. Dit is voorgesteld door de punten in de curve die boven de gemiddelde kans liggen. Er zijn ook plaatsen waar de deeltjes minder graag zitten, en daar ligt de curve onder de gemiddelde kans. Uiteindelijk oscilleert de curve naar een gemiddelde kans positie onafhankelijk ver van het deeltje. Bij de gas toestand is geen enkele structuur meer te zien, duidelijk voorgesteld door de correlatie functie, die overal een gelijke kans geeft om deeltjes aan te treffen. Wat nu geldt voor alle toestanden, vast of vloeibaar of gas, het maakt niet uit welke kant je gaat kijken, naar links, rechts, boven of onder, de correlatie functie is overal gelijk, 'symmetrisch' kan men ook zeggen.

Atomen/moleculen en colloïden hebben veel punten van overeenkomst en net als atomen vormen colloïdale oplossingen ook vaste, vloeistof en gas structuren, zoals net voorgesteld. Nu is het de bedoeling om de structuur van een colloïdale oplossing onder stroming te bepalen. Wat verandert in deze ordening wanneer er een stromingsveld op de colloïdale dispersie wordt aangebracht. Het colloïdale systeem wat we hier gebruiken bestaat uit bolletjes met een straal van 51 nm. (0.000000051 m.) opgelost in cyclohexaan.

Er was reeds een theorie bedacht die probeert te voorspellen wat er zou gebeuren. Wij gaan experimenteel proberen die theorie te bevestigen. De theorie heeft een vrij eenvoudig basis, namelijk de Newtoniaanse wetten. Anders gezegd, als men de plaats en de snelheid van deeltjes weet, kan men veel uitrekenen steunend op het 'actie geeft reactie' principe. Als twee colloïden elkaar raken dan weet je wat er na de botsing gebeurt en omdat je dat van alle deeltjes kan berekenen is het dus mogelijk om de structuur te berekenen ook als je een stromingsveld aanlegt.

Wat deze theorie voorspelt is een anisotropische structuur wanneer er een vloeistof stroom op de dispersie wordt aangebracht, anders gezegd een niet symmetrische structuur. Zonder stroming is de structuur van de colloïden in alle richtingen dezelfde, kijk naar uitleg bij tekening Figuur 3. De stroming die hier gebruikt wordt, is niet symmetrisch. Men kan het vergelijken met de wind, die heeft een richting (westen wind) en een snelheid (90 km/uur). Als de windrichting draait (oosten wind) dan krijg men niet hetzelfde effect, bomen gaan een andere kant op buigen.



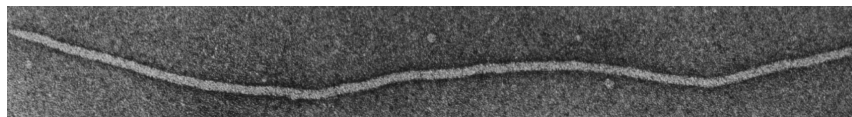
Figuur 4: Correlatie functies in twee richtingen met strooming. Loodrecht op de stromingsrichting blijft de structuur die van een vloeistof. Het rare is dat de structuur met de stroming mee veranderd in die van een gas fase. Dus men krijgt twee soorten fase.

Wat blijkt uit de experimenten is dat de vloeistofstroming ervoor zorgt dat de colloïden mixen, maar niet in alle richtingen en dat is het rare. In de richting van de vloeistof stroom (de wind) worden de colloïden gemixed en verliezen ze hun structuur en veranderd de correlatie functie naar een vlakke curve (zie Figuur 4) en word het een soort gasvormige fase. Alle structuren loodrecht op de stromingsrichting blijven behouden en de correlatie functie blijft onveranderd. De deeltjes blijven, loodrecht op de stromingsrichting, als het ware op hun relatieve plaatsen zitten en er blijft een vloeistof te zien. Als er heel hard geroerd word, verlies je deze speciale situatie en dat is iets wat de theorie niet voorspeld heeft maar dit is wel iets wat we gemeten hebben.

B) STAVEN

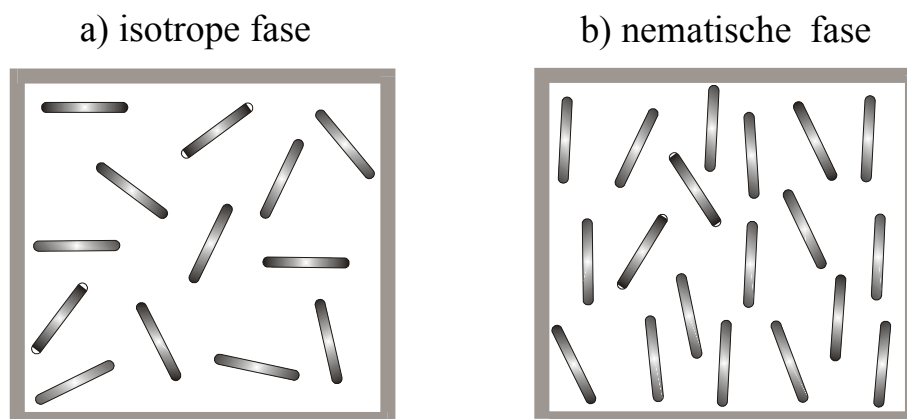
De herstructureringen, bestudeert in de vorige paragraaf, kunnen ook bij andere deeltjes vormen bekeken worden. Er zullen dan heel andere uitkomsten te zien zijn, zoals zal blijken. In deze thesis is ook gekeken naar staaf vormige deeltjes, om

preciezer te zijn. Er werd gewerkt met een virus, het fd virus. Dit virus is 880 nm lang en 15 nm breed (0.00088 mm op 0.000015 mm) en een beetje flexibel. (Het virus zorgt alleen voor wat buikinfecties bij biggetjes en is dus onschadelijk voor de mens)



Figuur 5: Foto van een fd-virus deeltje gemaakt met krachtige microscoop

Stel je hebt heel veel staafvormige deeltjes, dan zul je ze, als je ze economisch wilt stapelen, het liefst allemaal parallel moeten leggen, net als het pak spaghetti. Doe je dat niet dan heb je veel meer ruimte nodig. Deze fd-virussen en alle staafvormige colloïdale deeltjes stapelen zich zelf spontaan. Als je nu veel van die deeltjes bij elkaar stopt in een kleine ruimte, dan zullen ze op een gegeven moment allemaal spontaan parallel gaan liggen. Dit noemen we van isotroop (alle wanordelijk) naar nematische structuur (alle parallel) gaan (zie tekening Figuur 6).



Figuur 6: Isotroop (a) en nematische (b) fase. In de isotrope fase hebben alle deeltjes een random oriëntatie, in de nematische fase liggen ze allemaal min of meer parallel aan elkaar.

Nu brengen we een stromingsveld op een monster aan met deze fd-staafjes. Het resultaat zal zijn dat de deeltjes alle langzaam parallel aan het stromingsveld zullen gaan staan, net als een vlag in de wind. Hoe harder de stroming hoe beter ze parallel liggen. Door de stroming gaan ze dus eigenlijk een nematische of opgelijnde structuur vormen en dit verschijnsel hebben we in Chapter 3 uitgebreid bestudeerd. Ook hier is een theorie opgesteld met als startpunt de Newtoniaanse wetten, net als bij de bollen. Wat men nu moet weten van elk deeltje is de positie, de snelheid en de oriëntaties.

Ook nu weer zijn theorie en experiment vergeleken en zijn er overeenkomsten gevonden. De experimenten begonnen aan monsters met een zo hoge concentratie dat

de staafjes spontaan oplijnen en telkens werden ze verdund, dus minder fd-virussen per volume monster. Het resultaat was dat er telkens een sterkere stroming door de monster cel moest worden opgelegd om de opgelijnde structuur te vinden, tot op een gegeven moment dat die opgelijnde nematische structuur helemaal niet meer werd gezien.

De theorie die betreffende dit onderwerp al gepubliceerd is samen met diegene hier door ons opgesteld, wordt nu voor het eerst getoetst aan experimenten. Er werden resultaten gevonden die overeenkomsten toonde tussen theorie en experiment, zoals het steeds harder moeten roeren en het plots niet meer zien van die opgelijnde structuur. Er werden ook punten van verschil gevonden die tot nu toe nog niet begrepen worden. Deze discrepanties van de experimenten met de theorie geven ons gelukkig nog een beetje werk om uiteindelijk de puntjes op de i te kunnen zetten.

C) STAVEN TE HARD GEROERD

Tijdens het uitlijnen en testen van de experimentele apparatuur in de test fase en latere experimenten, zijn er rare fenomenen gezien. Op het eerste zicht leken dit op een soort gestreepte structuur (foto's in Chapter 4, Figure 4.5, p. 80). Theoretische modellen voorspellen dit soort structuren, maar voor zover bekend zijn ze nog nooit gezien in staafvormige colloïden. Het systeem waarin dit fenomeen gezien werd en wat dus gebruikt is voor de experimentele opstelling te testen, bestond uit kleine aluminium staafjes, zeg maar super kleine naalden (foto Figuur 1 a). Deze zijn rond de 100 nm lang en ongeveer 10 nm dik. Niet tegenstaande dit ook staafjes zijn, zijn ze een 8 maal korter dan de fd-virussen en dit kan een oorzaak zijn dat we de banden structuur niet gezien hebben in de fd systemen.

In dit hoofdstuk is geprobeerd een beter experimenteel inzicht te krijgen in deze banden structuur bij de aluminium staafjes. De reden dat dit zou kunnen ontstaan is dat bij het punt van oplijnen van de staafjes, er een delicate balans is tussen het roeren en het niet willen oplijnen. Het systeem gaat zich scheiden in twee gebieden: een gebied waar er veel deeltjes zitten die allemaal opgelijnd zijn, deze regio beweegt snel. De andere regio met een lagere concentratie aan staafjes die niet opgelijnd zijn, stroomt veel langzamer. Dit opsplitsen in regio's wordt 'shear banding' genoemd en resulteert in zo'n gestreepte structuur. Helaas is er, na uitvoerig onderzoek, een andere oorzaak van de bandenstructuur gevonden. Het eindbeeld op foto lijkt wel veel op shear banden, maar het heeft er niets mee te maken. De oorzaak van de banden structuur ligt in het feit dat als er hard word geroerd er een ander stromingspatroon ontstaat in de monster cel (zie tekening Figure 4.3, p 78) en niet meer het patroon voorgesteld in tekening Figuur 2.

NAWOORD

Dit stukje tekst wordt waarschijnlijk het meest gelezen, dus kan ik er maar beter voor zorgen dat het wat voorstelt.

Een van de motivaties om aan deze promotie te beginnen was dat ik mijn eigen incompetentie wel eens wou tegen komen, de drang om mijn ‘intellectuele grenzen’ op te zoeken. Dit had natuurlijk wat te maken met mijn woordblindheid en de constante opmerkingen hierover tijdens mijn schooltijd. Achteraf gezien is dat een behoorlijk arrogante gedachte en eigenlijk ben ik mijn grenzen wel tientallen keren tegen gekomen. Wetenschap is juist het tegenkomen van deze grenzen en telkens proberen deze te verschuiven. Bij dit gevecht tegen je eigen onwetendheid heb je hulp nodig. De lijst met namen die hier de revue gaat passeren zal vast niet volledig zijn, maar het zijn de mensen waar ik aan moest denken toen ik deze tekst schreef.

De opsomming wil ik beginnen bij Henk, mijn eerste promotor. Ik wil je bedanken voor de kans en de ruimte die je me hebt gegeven om dit onderzoek gestalte te geven. Ik vervolg onmiddellijk met mijn tweede promotor, Jan. Ik heb onze samenwerking alleen maar ervaren als ‘heel erg prettig’. Zowel op wetenschappelijk als persoonlijk vlak konden we het goed vinden. Ik denk dat ik heel veel geluk met jou heb gehad. Je stond altijd klaar, luisterde naar mijn zin of onzin en bleef rustig de dingen uitleggen ook als ik het niet begreep. Ook bij het schrijven, niet mijn meest sterke kant, bleef je geduldig verbeteringen aanbrengen. Bedankt Jan.

Voor het technische aspect van mijn promotie, wil ik eerst Bonny bedanken. Jij was de link tussen de instrumentmakerij en/of glasblazerij. Je leerde mij mijn wetenschappelijke ideeën om te zetten naar technisch uitvoerbare experimenten. Ook je drang naar perfectie bij het in mekaar zetten en testen van de dichroïsme/dubbelbrekings opstelling was een grote leerschool voor me en dit heeft mede gezorgd voor de resultaten hier gebundeld. Ook op persoonlijk vlak konden we het goed vinden, misschien wel omdat we allebei dezelfde hobby hadden, namelijk het jeugdwerk. Bonny bedankt.

Zoals de meeste onder jullie al begrepen hebben, was één opgave in mijn promotie onderzoek een apparaat bouwen/testen dat ingezet kon worden bij de wetenschappelijke vragen. De instrumentmakerij heeft deze handarbeid dan ook uitgevoerd. Ik wil Gerard, Kees, Hans, Harry en de drie IT-boys Patrick, Martijn en Carel hartelijk danken voor hun enthousiasme en technisch vernuft. Ik denk, nee ik weet zeker dat de universiteit en vele medewerkers niet weten hoe belangrijk jullie ondersteuning is. Goed wetenschappelijk onderzoek vraagt goed technisch kunnen, het een kan niet zonder het ander. Ook de glasblazerij met Piet, Peter en Igno wil ik bedanken voor hun prestatie. Een belangrijk onderdeel van het apparaat, de glazen cel waar het monster inzit, moest optisch perfect zijn en jullie gouden vingers hebben iets gemaakt wat mijn verwachtingen heeft overtroffen en mede heeft geleid tot een succesvol resultaat.

Beste kamergenoten, labgenoten en ex-labgenoten, ik ga geen namen noemen want ik vergeet vast enkele, ik wil jullie allemaal bedanken voor de toffe collegiale sfeer op het lab. De squashtornooien, het voetballen en de sinterklaas-en kerstfeestjes hebben bijgedragen tot die goede sfeer en dit had zeker zijn weerslag op de resultaten behaald. In english for non dutch speaking lab members; I want to thank my colleagues for their companionship which resulted in the fact that the Van't Hoff lab is a nice place to work. All the different social events stimulated a constructive atmosphere which on itself contributed to the results bundled.

There are two persons I want to mention explicitly, first Valerie Anderson. Thank you for editing the texts I gave you from the thesis, this was a great help. During my PhD, I also worked together with one Kroation dude, Zvonimir Dogic, a real physisist who worked in Boston. I learned a lot from you and it was fun working with you, I'm looking forward to become your colleage in Germany.

De audiovisuele dienst is op het vlak van communiceren van onderzoeksresultaten een goede steun en toeverlaat. Jan den Boesterd, Ingrid van Rooijen en Aloys Lurvink ook jullie bedankt bij het maken van bijvoorbeeld posters. Ik wil ook de stichting FOM bedanken voor hun steun. Een telefoontje en/of brief naar het FOM-buro, zijnde mevr. M.W. Slob-van der Wal of mevr. J.J. Middelwaarde, leverde snel het gewenste resultaat op. Vele organisaties zouden een voorbeeld aan jullie kunnen nemen wat beleid en effectiviteit betreft.

Ik zou graag mijn verhaal vervolgen met de 'Nederlandse' vrienden. We zijn alle tegelijk begonnen in Utrecht aan de opleiding Scheikunde (1992). Machiel, Karen, Bart, Dirk en Els, ik wil jullie bedanken voor jullie steun in woorden en daden. Dit wordt voor mij het afscheid van Utrecht en het begin van een periode waarin we

elkaar minder vaak kunnen zien en ja dat doet een beetje pijn. Met wat nostalgie en heel veel dankbaarheid zal ik blijven denken aan jullie vriendschap van de afgelopen 8 jaar. He Ollanders, Julich is niet zo ver, dus we houden zeker contact. Een extra motivatie om me niet te vergeten: In Duitsland is het bier beter dan in Utrecht, maar nog niet zo goed als in België!

De Belgische club mag ik ook niet vergeten; Cor, Nathalie, Myriam, Janine, Els en Jeroen en de rest van de 'Op Vrije Voeten' maffia ook jullie bedank ik voor jullie interesse en steun. Ons organiseren van kinder/tienerweekends, het vergaderen en de andere dingen die bij een voorzitterschap van zo'n landelijke erkende jeugdendienst horen, waren een aangename afwisseling met de formules en experimenten. De combinatie van hard science and soft management, was voor mij erg motiverend, inspirerend en afwisselend.

Deze lofzang wil ik eindigen met het bedanken van mijn familie; mijn ouders, Ab en Lida, en mij broer, Remco. Zij zijn in mijn leven een constante steun geweest. Zonder hun support zou ik nooit op dit punt in mijn leven hebben kunnen geraken. Ik weet niet zo goed hoe ik dit allemaal anders kan zeggen, maar ik draag dit proefschrift dan ook aan jullie op. Het klinkt kinderachtig en/of sentimenteel maar woordblindheid is in mijn gehele studie, van lagere school tot nu, een constante donderwolk geweest en jullie hebben voor mij altijd onvoorwaardelijk klaar gestaan om te helpen en te adviseren wanneer onbegrip en incompetentie van leerkrachten weer dreigde mij te blokkeren. PA, MA, BROERTJE, deze is voor jullie.

LIST OF PUBLICATION

A.M. Wierenga, T.A.J. Lenstra and A.P. Philipsen, Aqueous dispersions of colloid gibbsite platelets: synthesis, characterisation and intrinsic viscosity measurements." *Colloids and Surfaces A: Physicochemical and Engineering Aspects*, Vol. 134, p 359-371 (1998)

T.A.J. Lenstra and J.K.G. Dhont, Flow Dichroism in Critical Colloidal Fluids, Submitted to *Physical Review E*

T.A.J. Lenstra, Z. Dogic and J.K.G. Dhont, Shear-induced Displacement of Isotropic-Nematic Spinodals, Submitted to *The Journal of Chemical Physics*,

CURRICULUM VITAE

De schrijver van deze dissertatie is geboren op 20 mei 1973 te Utrecht. Na het behalen van zijn diploma middelbaar onderwijs aan het Atheneum van Kapellen (België) met de specialisatie wiskunde-wetenschappen, begon hij in 1992 aan zijn studie scheikunde aan de Universiteit Utrecht. In februari 1997 rondde hij zijn opleiding af met het behalen van zijn doctoraalexamen met het hoofdvak Fysische- en Colloïdchemie, aangevuld met de keuzevakken Theoretische chemie en Kristallografie.

Op 1 maart 1997 trad hij in dienst van de stichting FOM (Fundamenteel Onderzoek der Materie) als onderzoeker in opleiding bij de werkgemeenschap Statistische Fysica. Hij werd te werk gesteld op het Van't Hoff laboratorium voor Fysische en Colloïdchemie verbonden aan de Universiteit van Utrecht en zijn werkzaamheden hebben geleid tot de dissertatie die heden voor u ligt. Na de openbare verdediging en het beëindigen van zijn aanstelling, treedt Tjerk Lenstra in maart 2001 in dienst bij het Forschungszentrum Jülich, aan het Institut für Festkörperforschung in Duitsland.



T.A.J. Lenstra